

UNIVERSITY OF CALGARY

From Greensands to Green Technology: Examination of Carbon Dioxide Storage
Potential in Glauconitic Sandstones

by

Qin Zhang

A THESIS

SUBMITTED TO THE FACULTY OF GRADUATE STUDIES

IN PARTIAL FULFILLMENT OF THE REQUIREMENTS FOR THE

DEGREE OF DOCTOR OF PHILOSOPHY

GRADUATE PROGRAM IN GEOLOGY AND GEOPHYSICS

CALGARY, ALBERTA

MAY, 2022

©Qin Zhang 2022

Abstract

Glauconite is a divalent cation-bearing mineral abundant in sedimentary rocks and hydrocarbon reservoirs worldwide, and it may be important for ongoing efforts to geologically store anthropogenic CO₂. Since glauconite naturally contains both Fe(II) and Fe(III) in its mineral structure, it can also be leveraged to constrain paleoenvironmental redox conditions. Nevertheless, because of its complex mineralogy and redox sensitivity, thermodynamic and kinetic properties of glauconite have been difficult to constrain. This thesis has been devoted to fill this significant knowledge gap. Chapter 2 contains a detailed evaluation of the mechanisms through which carbonate minerals naturally replace glauconite during diagenesis of glauconitic sandstones from the Mannville Group in Alberta, Canada. Using a combination of petrological and geochemical analyses, we show that glauconite carbonation is a reduction-facilitated, coupled glauconite recrystallization and siderite precipitation reaction, which is accompanied by a significant reduction of Fe. These results suggest that geochemical conditions, most importantly, temperature, partial pressure of CO₂, and fluid redox state were thermodynamically favorable for glauconite carbonation during burial diagenesis of Mannville Group glauconitic sandstones. Chapter 3 quantifies the far-from-equilibrium rates of glauconite dissolution using a novel experimental apparatus specifically designed to explore mineral dissolution kinetics under strictly anaerobic conditions. Steady-state glauconite dissolution rates were measured at varying pH from 1.7 to 11.2 and temperature from 24 to 80 °C. The experimental results show stoichiometric or close-to-stoichiometric glauconite dissolution for Fe, Mg and Si. In comparison to previous studies, we emphasize that the mechanism of glauconite dissolution is determined by redox condition and temperature, and the dissolution rates are pH-dependent in acidic conditions and pH-independent in natural to basic pH. Chapter 4 uses calculations based on 11,652 well logs to show that glauconitic sandstones offer significant and previously overlooked potential for sedimentary reservoir-based mineral carbonation. Our results demonstrate that hundreds of gigatons of CO₂ could be sequestered by carbonating the immense quantity of glauconite underlying Alberta, Canada alone. Together, these findings suggest that glauconite had been underestimated both in terms of availability and reactivity, and these new findings provide important insights to re-evaluate CO₂ storage in sedimentary basins.

Preface

Chapter 2. Published as Zhang, Q., and Tutolo, B.M., "Geochemical Evaluation of Glauconite Carbonation during Sedimentary Diagenesis." *Geochimica et Cosmochimica Acta* 306 (2021): 226-244.

Chapter 3. Submitted to *Geochimica et Cosmochimica* as Zhang, Q., Nightingale, M., Awolayo, A.N., and Tutolo, B.M., "Kinetics of glauconite dissolution under anaerobic conditions as a function of pH and temperature."

Chapter 4. Published as Zhang, Q., and Tutolo, B.M., "Evaluation of the potential of glauconite in the Western Canadian Sedimentary Basin for large-scale carbon dioxide mineralization." *International Journal of Greenhouse Gas Control* 117 (2022): 103663.

Acknowledgements

It would have been a difficult time for anyone without a good support system over the past 2.5 years, and my journey through the Ph.D. process has been made possible, enhanced, and refined by many people from a variety of positions. I am deeply grateful towards all of them, and I express my gratitude in no particular order.

I have felt incredibly fortunate to be a member of the Geoscience department at the University of Calgary, and I am proud to be a product of this place. I am deeply appreciative of the faculty and staff who guided me through coursework and research, inspired me with different perspectives, and introduced me to new methods and technologies from a wide range of backgrounds. It is not at all an exaggeration to say that I learnt something new everyday during my 4 years at U of C. I thank my committee members Bernhard Mayer, Chris Clarkson, Stephen Hubbard, Rudi Meyer, and Sasha Wilson for their continuous engagement. Their expertise, insights and visions have helped improve this thesis profoundly and will continue to benefit me throughout my research career.

I thank Per Pedersen for pointing me to the right direction since the first month of my Ph.D. Chapters 2 and 4 of this thesis would not have been possible without Per's help locating the suitable Mannville Group rock samples and accessing the core log database. I thank Christopher Debuhr for his excellent skills on the SEM, many of my best images were taken with his help. I thank the Applied Geochemistry group for their engagement with grad students, and especially for offering us the opportunities to collaborate with Michael Nightingale. Since the beginning of my experimental work, I started constantly bothering Mike with questions and ideas about fluid samples and everything else around the lab; Chapter 3 would not have been possible without Mike's help. I am also deeply grateful for the valuable experiences I have had with all the students I have taught, mentored, and worked with; I have enjoyed myself profoundly and learnt a great deal from working with all of them.

The RTG group has been my anchor throughout this Ph.D. process. I thank Simone Pujatti for always being ready to offer some dark jokes when I complained to him, and for knowing everything about rocks and taking the time to explain them to me. I thank Yury Klyukin for being my on-call mineralogy tutor, and for his endless patience to help me analyze difficult samples on the RAMAN. I am grateful to Alec Hutchings for teaching me a variety of field and lab techniques and giving me the opportunity to experience the most abundant mosquitoes anyone could ever encounter. Adedapo Awolayo had worked past midnight for several days helping me finish Chapter 3 on time; his work showed me a different perspective and I cannot stress enough how grateful I feel for his diligence, patience, and support. Juan Carlos de Obeso and I collaborate on several experimental projects, without a word, he had taken over all the lab work over the past month so that I could focus on writing my thesis. I am extremely appreciative for this and all other ways that Juan Carlos has supported me. It has been a great honor working with all members of the RTG group.

I thank the strong women in my life. My mother, Jian Cao, my cousin, Yuqiao Cao, and best friend, Pengpeng Wang. Each of them had faced their own difficulties over the past few years, they have always been generous with their support, nonetheless. My mother will probably not believe that I can finish this Ph.D. until she sees the degree; she thinks it is so difficult that she has to constantly offer me a backup plan, “don’t worry, mom has savings”. This, while not being the most encouraging, offered a huge sense of security, and I am grateful for every effort she has made in her own way to make life easier for me. Yuqiao and Pengpeng are both family and friends. I am thankful for the lovely messages and funny, thoughtful gifts they kept sending my way.

My furry friends, Guoguo Cao and Luna Meownington, I know they both would rather eat my thesis than read it, I am still thankful for their faithful companionship.

I thank Kieran Dunne for not only being the best partner and friend, but also a diligent computer technician, writing coach, career consultant, and cheerleader. I thank him for believing in me before I believed in myself.

Finally, I thank my adviser, Benjamin Tutolo. I often advise younger students to choose an advisor who loves what they do, because I feel incredibly fortunate that I did. Ben's combination of enthusiasm, expertise, wisdom, and vision has broadened my horizon and inspired me to explore fundamental science beyond its immediate application. Ben is kind and generous, and willing to let the lab group be part of his personal life; being able to celebrate holidays and accomplishments with Ben's family means more than what he can imagine to international students like me. I thank Ben for all his support along the way, and moving forward, it is my hope to emulate his abilities as a scientist and educator.

Funding Support: this thesis research was undertaken thanks in part to funding from the Canada First Research Excellence Fund, and National Science and Engineering Research Council of Canada (NSERC) Discovery Grant RGPIN-2018-03800.

Dedication

To Mom and Kieran

Table of Contents

Abstract.....	ii
Preface	iii
Acknowledgements	iv
Dedication.....	vii
Table of Contents.....	viii
List of Tables	xi
List of Figures	xii
1 Chapter 1 Introduction.....	1
1.1 Global Climate Crisis and Our Unique Opportunities.....	1
1.2 Glauconite in Sedimentology and Stratigraphy	3
1.3 Challenges to Utilize Glauconite as a Resource for CO ₂ Sequestration	6
2 Chapter 2 Geochemical evaluation of glauconite carbonation during sedimentary diagenesis.....	9
2.1 Introduction	10
2.1.1 Previous Research on Glauconite	11
2.1.2 The Potential for Carbon Mineralization in Glauconitic Sediments.....	13
2.2 Methods.....	15
2.2.1 Material.....	15
2.2.2 Mineral Identification and Chemical Analyses.....	16
2.2.3 Redox Characterization by XANES.....	17
2.2.4 Geochemical Modeling	19
2.2.5 Thermodynamic Data for Geochemical Calculations	22
2.3 Results.....	24

2.3.1	Petrography	24
2.3.2	Chemical Analyses.....	26
2.3.3	Iron Redox during Glauconite Carbonation	32
2.3.4	Geochemical Modeling	33
2.4	Discussion.....	39
2.4.1	Summary and Interpretation of Petrographic and Geochemical Observations.....	39
2.4.2	Implications for CO ₂ Mineralization in Glauconite-rich Sediments	44
2.5	Conclusions	45
3	Chapter 3 Kinetics of glauconite dissolution under anaerobic conditions as a function of pH and temperature 47	
3.1	Introduction	48
3.1.1	Glauconite and the global Fe and C cycles.....	48
3.1.2	Measurements and estimates of glauconite dissolution rates	49
3.2	Methods.....	51
3.2.1	Mineral Preparation	51
3.2.2	Experimental Setup.....	53
3.2.3	Solution Analyses	57
3.2.4	Rate Calculation, Uncertainties, and the Propagation of Errors	58
3.2.5	Derivation of Rate Equation.....	60
3.2.6	Geochemical Modelling	61
3.3	Results.....	64
3.3.1	Chemical Analyses.....	64
3.3.2	Rate Equation.....	66
3.3.3	Geochemical Modelling	67
3.4	Discussion.....	74

3.4.1	Elemental Releases from Glauconite	74
3.4.2	Temperature and pH Dependence of Glauconite Dissolution	77
3.4.3	Glauconite kinetics and implication for CO ₂ sequestration in glauconite-rich sediments.....	81
3.5	Conclusions	83
4	Chapter 4 Evaluation of the Potential of Glauconite in the Western Canadian Sedimentary Basin for Large-Scale Carbon Dioxide Mineralization.....	84
4.1	Introduction	85
4.1.1	Material and Methods	89
4.2	Results	91
4.3	Discussion.....	92
4.3.1	Challenges and opportunities for glauconite carbonation	95
4.4	Conclusions	98
5	Chapter 5 Conclusions.....	99
5.1	Summary	99
5.2	Implication for Geological CO ₂ Storage.....	101
	Bibliography	103
	Appendices	118
	Appendix A Supplementary Material for Chapter 2.....	118
	Appendix B Supplementary Material for Chapter 3.....	118
	Appendix C Supplementary Material for Chapter 4.....	121
	Appendix D Copyright Letter of Permission	123

List of Tables

Table 2-1 Water chemistry data (Cody and Hutcheon, 1994) and calculated gas fugacity (Sect.2.2.4) used to simulate the reaction between 0.1 kg glauconite and Mannville reservoir fluids at 35 °C.....	21
Table 2-2 Calculation values for the thermodynamic properties of minerals (25°C, 1 atm)	26
Table 2-3 Equilibrium constants for calculating the solubility of minerals as a function of temperature at steam saturation conditions (reactions shown as Eq.2-2 and Eq.2-3).	26
Table 2-4 Maximum, minimum, mean and standard deviation of EPMA analyses (Oxide wt.%) of glauconite pellets from Mannville Group, n=23, Fe was analyzed as Fe ²⁺	31
Table 2-5 Maximums, minimums, means and standard deviations of EPMA chemical analyses (in oxides wt.%) of dolomite (dol) crystals with heterogeneous rims, n=10 (core), and n=3 (rim); and siderite (sd) crystals, n=8 (euhedral), and n=3 (anhedral).	32
Table 2-6 Elemental compositions of bulk rocks (oxides wt.%), major elements measured by XRF, S measured by IR combustion, LOI = loss on ignition.....	34
Table 3-1 Compositions (g/kg) of inlet solutions used for the glauconite dissolution experiments (modified after Saldi <i>et al.</i> (2007)).	56
Table 3-2 Calculated thermodynamic properties of the two types of glauconites used in the flow-through experiments.....	63
Table 3-3 Equilibrium constants for calculating the solubility of glauconites as a function of temperature at steam saturation conditions. (Reactions shown as Eq. 3-5 and Eq. 3-6).....	63
Table 3-4 Water chemistry data and calculated gas fugacity used to simulate the reaction between 0.1 kg glauconite and reservoir pore fluids at various temperatures. The initial activities of Fe ⁺⁺ and Al ⁺⁺⁺ were set by equilibrium with siderite and kaolinite, respectively.....	64
Table 3-5 Experimental conditions, steady-state chemical fluxes, reacting mineral masses, Mg, Fe, and Si-derived apparent dissolution rates, and analytical errors of glauconite flow-through experiments.....	69
Table 3-6 Experimental conditions, steady-state chemical fluxes, reacting glauconite masses, BET surface area measurements, K-derived apparent dissolution rates, and analytical errors of glauconite flow-through experiments.	73
Table 3-7 Kinetic rate parameters derived from fitting Arrhenius equation to the measured glauconite dissolution rates.....	74
Table 3-8 Ratios of elements calculated from EDS measurements on glauconite Type II.....	77

Table 4-1 Parameters used to calculate the total amount of glauconite (*MGl_t*) in the Mannville glauconitic sandstone member in Alberta. The minimum (a) and maximum (b) masses of glauconite. The medium (c) value was used in the following calculations.92

List of Figures

Figure 2-1 Mineral distributions of the Mannville glauconitic sandstone (2054.33 m).....	27
Figure 2-2 SEM images and energy dispersive spectrometry maps of element distribution in the Mannville glauconitic sandstone (2055.02 m).....	28
Figure 2-3 Energy dispersive spectrometry map of element distribution and SEM images of the Mannville glauconitic sandstone (2053.61 m).....	29
Figure 2-4 SEM images and energy dispersive spectrometry maps of element distribution in the Mannville glauconitic sandstone (2054.33 m).....	30
Figure 2-5 Al and Fe contents in the EPMA analyses on glauconite grains (data provided in supplementary material).	31
Figure 2-6 X-ray fluorescence maps of the Mannville glauconitic sandstones.	35
Figure 2-7 Processed XANES spot analyses illustrating the range of Fe oxidation states in the examined samples. ...	36
Figure 2-8 Cluster analyses of XANES maps and accompanying plots of the pre-edge characteristics of the derived spectra.	37
Figure 2-9 Activity diagram illustrating the stability fields of iron minerals in Mannville Group.	38
Figure 2-10 Calculated results of thermodynamic modeling.....	38
Figure 3-1 Scanning electron microscopy (SEM) images of pre-experimental glauconite grains Type I (a) and Type II (b), and post-experimental glauconite Type I (c) and Type II (d).....	53
Figure 3-2 Experimental apparatus that maintained strictly anoxic environments and constant temperatures.	57
Figure 3-3 Elemental releases from glauconite dissolution experiments.....	66
Figure 3-4 Reaction paths calculated by numerically reacting glauconite (Type II) with pore fluids (Table 3-4).	68
Figure 3-5 Comparison of Si versus Fe (a) and Si versus Mg (b) release rates.....	75
Figure 3-6 Variation of the logarithm of measured steady-state glauconite dissolution rates (derived by Si) as a function of pH.....	80

Figure 3-7 Pre-experimental glauconite (a), post-experimental glauconite (b&d) and a Fe-Si secondary precipitate (c).
.....81

Figure 4-1 Distribution of wells (blue dots) that intersect with the Mannville glauconitic sandstones (> 800 m depth)
in Alberta.90

Figure 4-2 Glauconitic sandstone thicknesses calculated from the TVDs recorded in the core logs.92

1 Chapter 1 Introduction

1.1 Global Climate Crisis and Our Unique Opportunities

The current rate of anthropogenic release of CO₂ into the atmosphere is expected to drive the climate system over tipping points beyond which limiting global warming to 1.5 °C above pre-industrial level scenarios is impossible (IPCC, 2022). Numerous consequences, such as weather extremes, intensive forest fires, stronger hurricanes and floods, and diminishing fresh water supplies, are already being felt around the globe (e.g., Lovejoy and Nobre, 2019; Moss, 2010; Warszawski et al., 2021). Irreversible impacts are expected as natural and human systems are pushed beyond their ability to adapt, yet the window to avert the most destructive effects of climate change is rapidly closing (IPCC, 2022). To combat the devastating effects of anthropogenic climate change, global societies must take urgent actions. Continued use of fossil fuels as an energy source, even at an intentionally diminishing capacity, will require capturing CO₂, from both point source emitters and directly from the atmosphere, and the long-term prevention of its ever entering or returning to the atmosphere. A key technology for doing this is CO₂ storage and mineralization in geologic reservoirs (Bickle, 2009; DePaolo and Cole, 2013; IPCC, 2022; Lackner, 2002; Seifritz, 1990; Warszawski et al., 2021; Zhang and DePaolo, 2017). Geological carbon sequestration (GCS) has been explored worldwide by many branches of science and technology in response to the challenge of stabilizing global atmospheric CO₂ concentrations. In GCS, CO₂ can be physically trapped in porous rocks below an impermeable caprock (structural trapping), part of which may become trapped in small pores (residual trapping) or dissolved in formation water (solubility trapping) and/or react with rocks to form stable carbonate minerals (mineral trapping) (Snæbjörnsdóttir et al., 2020). As the most stable form of these mechanisms, mineral trapping is widely considered the most desirable outcome of GCS. The process of trapping CO₂ by reacting it with cation-bearing silicate minerals to form stable carbonate minerals (herein referred as mineral carbonation, also known as carbon mineralization) was first proposed over 30 years ago (Seifritz, 1990) and was followed by later research that demonstrated its security and permanence (e.g., Bickle et al., 2013; Depaolo and

Cole, 2013; Lackner, 2002; Oelkers et al., 2008; Snæbjörnsdóttir et al., 2020; Zhang and DePaolo, 2017). Mineral carbonation requires the initial dissolution of gaseous or supercritical CO₂ into water, where it either forms carbonic acid and provokes silicate mineral dissolution or reacts directly with the cation-rich formation fluids. Alternatively, when water is added to supercritical CO₂, a thin water film forms on the mineral surfaces (wet supercritical CO₂), creating a highly reactive front that leads to substantial (54% to 116%) increase in mineral dissolution rates (Lacinska et al., 2017; Min and Jun, 2018; Thompson et al., 2013). Then, divalent cations released by silicate mineral dissolution react with dissolved or wet supercritical CO₂ to form stable carbonate minerals. Rock formations with high supplies of reactive minerals (minerals that readily supply divalent cations such as Fe, Ca and Mg) are therefore crucial for CO₂ mineralization (Baines and Worden, 2004; DePaolo and Cole, 2013; Zhang and DePaolo, 2017). For this reason, (ultra)mafic rock formations, such as basalts and peridotites, are often seen as favorable locations for mineral carbonation reactions, while sedimentary reservoirs such as limestones and sandstones are assumed to be too poor in these reactive minerals to present significant carbonation opportunities (e.g., Snæbjörnsdóttir et al., 2020).

Although CO₂ mineralization capacities in sedimentary basins are commonly overlooked, both depleted and active fossil fuel reservoirs offer secure storage space for CO₂ in the subsurface because GCS can reuse the caprocks that were able to trap the buoyant oil and gas in these reservoirs over geologic time to physically trap CO₂. GCS in depleted oil and gas reservoirs is considered to be the most economical method, most importantly, because these reservoirs have been extensively surveyed during the exploitation stage, and pre-existing infrastructure such as wells and pipelines can be re-purposed for CO₂ transport and injection with minor modifications (e.g., Bickle, 2009; Fuss et al., 2018; Li et al., 2006; Voormeij and Simandl, 2002). Moreover, pore-pressure and poroelastic stress changes associated with prior oil and gas production make induced seismicity less likely, which means large-scale GCS in depleted oil and gas reservoirs is not only less expensive than, e.g., sub-seafloor strategies, but is also unlikely to cause seismic hazards in continental settings (Dvory and Zoback, 2021; Stork et al., 2018). In active reservoirs, CO₂ injection may result in enhanced oil or gas recovery (EOR) and simultaneous CO₂ sequestration, which could also lead to an economic benefit by offsetting the cost of capture

(Bachu, 2008; Pooladi-Darvish et al., 2008; Voormeij and Simandl, 2002). Although such operations may lead to net positive CO₂ emissions, the screening criteria for operation safety and the reservoir engineering for effective injection, are valuable and readily adaptable to the development of CO₂ storage technologies (Bachu, 2016; Han et al., 2010; Kavscek, 2002).

Global estimates of CO₂ storage capacity in depleted oil and gas fields range from 458 to 923 GtCO₂ (Fuss et al., 2018; Yoshikazu et al., 1993). Nevertheless, these estimates only account for volumetric capacity for structural trapping because, as mentioned before, mineral trapping is considered negligible in sedimentary basins. In this thesis, we use the Mannville Group glauconitic sandstones in Alberta, Canada as an example to show that sedimentary basins, particularly glauconite-rich sandstones, not only provide pore space for the physical trapping of CO₂, but also abundant opportunities for stabilizing CO₂ via mineral carbonation, which ensures the long-term security of storage by reducing the reliance on the caprocks over time. The Mannville Group glauconitic sandstone unit in Alberta has been studied as a CO₂ storage site and is amongst the most well-documented glauconitic sandstones in the world (e.g., Abercrombie et al., 1994; Chiang, 1984; Christopher, 1984; Cody et al., 1999; Cody and Hutcheon, 1994a; Hayes et al., 1994b; Hradsky and Griffin, 1984; Williams, 1963). This wealth of information provides us with valuable and unmatched insights into the parameters governing the capacity for sedimentary reservoir-based CO₂ mineralization worldwide. The analyses we present here suggest that similar, hydrocarbon-producing, glauconite-rich formations worldwide, such as the Shannon Sandstone Beds in Wyoming, US (Hansley and Whitney, 1991), Chadra sands in Gialo field, Libya (Al-Shaieb and Shelton, 1978), the Great Burgan oil field in Kuwait (El-Sharkawi and Al-Awadi, 1982) and the Sacha oil field of Ecuadorian Oriente (Canfield et al., 1982) likely also offer previously underestimated CO₂ mineralization capacities.

1.2 Glauconite in Sedimentology and Stratigraphy

Iron (Fe)-bearing minerals are important redox indicators in sedimentary environments because Fe is the only common, structure-determining metal that occurs in both reduced (Fe(II)) and oxidized (Fe(III)) valence states (Ireland et al., 1983). Glauconite naturally contains both Fe(II) and

Fe(III), it thus can be leveraged to constrain paleoenvironmental redox conditions (Berner, 1981; Ireland et al., 1983; Odin, 1988; Odin and Matter, 1981). Formation and alteration of glauconite also provide insights into the long-term sequestration of iron during diagenesis (Baldermann et al., 2015). Glauconite is commonly used to interpret paleoenvironmental conditions due to its global distribution throughout the geologic record (e.g. Odin, 1988; Kronen and Glenn, 2000; Hesselbo and Huggett, 2001; Harding *et al.*, 2014b). Some of these interpretations rely on identifying the alteration stage of glauconite (also known as evolution/development stage): development from nascent to highly evolved glauconite is achieved by a recrystallization process through progressive equilibrium with bottom seawater, which indicates extended residence time at the seafloor prior to burial (López-Quirós et al., 2019; Odin and Matter, 1981). Glauconite is also a sensitive proxy of low sedimentation rates, organic matter-rich, and semiconfined micro-environments in the marine realm. It therefore constitutes a powerful tool for sedimentological and stratigraphic interpretations, especially when it associates with well-defined trends of sea-level changes (Eder et al., 2007; López-Quirós et al., 2019).

Although glauconite has been studied extensively, a lack of consistency in terminology has been persistent in published research (e.g., Odin and Matter, 1981; Odin, 1988; Harding et al., 2014). Many terms have been used to identify the green sedimentary mineral, including “glauconite,” “greensands,” “glaucony,” or “glauconitic minerals”. The mineralogical definitions of glauconite vary as well: some define glauconite as a series of micas (Dyar et al., 2008), while others refer to glauconite as an iron-rich variety of the clay mineral illite or smectite (Burst, 1958; López-Quirós et al., 2019). The term “glauconite” has also been employed as a common field term for small, rounded, green pellets and grains (Odin, 1988). As a result, the mineral “glauconite” is not recognized by the International Mineralogical Association (IMA). It is possible that no fundamental difference exists amongst these definitions, but rather that they refer to different stages of glauconitization (see below). Regardless, previous studies agree that glauconite is abundant in marine greensands formations worldwide (e.g., Baldermann et al., 2015; Bornhold and Giresse, 1985; Jach and Starzec, 2003; Odin, 1988; Odin and Matter, 1981b; Wigley and Compton, 2007); some lacustrine and alluvial occurrences have also been reported (e.g., McRae, 1972). Glauconite occurs mostly on continental shelves, and it is generally widespread on

present-day shelves from 50 °S to 65 °N, at water depths between 50 and 500 m, particularly on the upper slope and outer shelf between 200 and 300 m (Odin and Matter, 1981). Glauconite pellets mostly form *in situ*, or are transported over a short distance, because their structures are too weak to sustain extensive transportation (Triplehorn, 1967; Wermund, 1961). To investigate glauconite diagenetic processes, it is also important to differentiate the effects of chemical weathering and the different stages of glauconitization. For example, Pestitschek et al. (2012) found that fresh glauconite samples are generally dark green, whereas weathered samples are generally olive green to yellowish brownish green coupled with a loss of K and Fe during weathering. On the other hand, Loveland (1981) observed color differences in their samples, but concluded such differences were caused by different stages of glauconitization. More recently, UV–Vis–NIR color spectroscopy was applied on glauconite to determine its Fe²⁺/Fe³⁺ ratio in the mineral structure (López-Quirós et al., 2019). Glauconite morphology and internal structure have been studied extensively; dozens of recognized morphological types and internal structures are described in previous research (e.g., Triplehorn, 1966). The many different morphologies of the materials which cause the greenish aspect of “greensand” or “greenearth” can schematically be grouped into the granular and the film facies of glauconite (Odin and Matter, 1981).

Glauconitization (i.e., formation of or conversion into glauconite) results in a continuum of minerals from potassium (K)-poor, disordered glauconitic smectite to K-rich, ordered glauconitic mica. Stages of alteration are defined by increasing K₂O content, where 2 wt.%–4 wt.% K₂O is nascent stage, 4 wt.%–6 wt.% K₂O is slightly evolved, 6 wt.%–8 wt.% K₂O is evolved, and greater than 8 wt.% K₂O is highly evolved glauconitic mineral (Harding et al., 2014; Hesselbo and Huggett, 2001; Huggett et al., 2000; Kronen and Glenn, 2000; Odin and Matter, 1981). The mechanism that dictates K releases from or fixation into the structures of glauconite is referred to as layer charge alterations. This phenomena is especially well-studied for Fe-rich phyllosilicates in which redox processes change layer charge (reduction of structural Fe³⁺ to Fe²⁺) and promotes immobilization of interlayer cations such as K⁺ and Li⁺ (Chen et al., 1987; Florence et al., 2017; Huang, 2005; Komadel et al., 2006; Simonsson et al., 2009). For example, through a series of Fe-reducing processes applied on phyllosilicates, the authors observed an increase in structural Fe(II) content leading to increases in layer charge and a K⁺ fixation; as the Fe was re-oxidized, the K that

was previously fixed was released (Florence et al., 2017). Similar Fe-reduction induced charge imbalances which were stabilized by K^+ uptake into the interlayer sheets during diagenesis of glauconite was observed by López-Quirós et al. (2020). Because the redox state of structural Fe determines the release or fixation of K and hence glauconite's contribution to alkalinity production and nutrient release, geochemical research on glauconite without redox considerations may not be applicable to glauconite in its natural conditions. As a result, many of the sedimentological and stratigraphic implications derived from such studies on glauconite remain open to debate, in part, due to the lack of geochemical constraints on the mechanisms of glauconite diagenesis (Harding et al., 2014).

1.3 Challenges to Utilize Glauconite as a Resource for CO_2 Sequestration

Besides its scientific significance, glauconite is an important cation provider for carbon mineralization in sedimentary basin-based geological carbon storage (GCS). Observations of some greensands formations, and numerical simulations based on these observations, suggest that glauconite is commonly diagenetically converted to carbonate minerals such as siderite, ankerite, and ferroan dolomite (Chafetz, 2007; Odin, 1988; Zhang and Tutolo, 2021). Harnessing the natural glauconite carbonation processes could thus provide an effective and secure mechanism for permanent sequestration of anthropogenic CO_2 (Zhang and Tutolo, 2021).

The chemical composition can be generalized as $K_{0.75}Fe_{1.25}^{3+}Fe_{0.25}^{2+}Mg_{0.25}Al_{0.5}Si_{3.75}O_{10}(OH)_2$ for glauconite (Blanc et al., 2015). Based on previous redox-sensitive analyses, $Fe(II)/Fe_{total}$ in glauconite ranges from ~10 - 20% (Mackenzie et al., 1988; Ali et al., 2001; Tutolo et al., 2020) to 50% (Zaitseva et al., 2008). Once liberated from the glauconite structure, the $Fe(II)$ is readily available for carbonation. Although glauconite is commonly associated with siderite (e.g., Berner, 1981; El-Sharkawi and Al-Awadi, 1982; Ivanovskaya et al., 2014), little is known about the mechanism by which $Fe(III)$ is reduced to subsequently form siderite. For example, it is unclear whether Fe is reduced while still in the glauconite structure, or after glauconite dissolves, and thus it is inconclusive to whether glauconite development is by "layer-growth mechanism" (López-Quirós et al., 2020) or "precipitation-dissolution-recrystallization mechanism" (Odin and

Matter, 1981). To guide the engineering efforts that will be critical to exploit glauconite carbonation for GCS, one of the most important steps is to understand the change of redox states of Fe in glauconite. For instance, if Fe is reduced while still in the glauconite mineral structure, then the approach must be tuned to ensure the transportation of reducing fluids into glauconite grains; if Fe is only reduced after glauconite dissolves, then the approach can be completely solution-based (e.g., reductants added to glauconite-undersaturated reservoir fluids). Part of this dissertation seeks to illuminate the controls on glauconite diagenesis by taking into account the effects of redox conditions. Chapter 2 combines geochemical modelling with petrographic observations and geochemical analyses on the Mannville Group glauconitic sandstones to demonstrate that glauconite carbonation is thermodynamically favorable in hydrocarbon reservoirs. Chapter 2 is published by *Geochimica et Cosmochimica Acta*. Sample processing, petrographic and geochemical data collection, and writing was done by Q. Zhang; XANES data collection, geochemical modelling, edits, and supervision by B.M. Tutolo.

Although recent efforts have sought to update these parameters (Heřmanská et al., 2022), the most comprehensive and widely accepted database of mineral dissolution rate parameters is that of Palandri and Kharaka (2004). This database includes dissolution rates of glauconite, which were derived from the data compilation by Sverdrup (1990), which, in turn, was derived from Cloos *et al.* (1961). Depending on glauconite dissolution mechanisms in different temperature and pH conditions, these parameters may or may not produce useful predictions of glauconite dissolution rates, because Cloos *et al.* (1961) conducted their dissolution experiments in solutions with very acidic pH (1.97-2.06 M HCl) and at high temperatures (40, 450, and 650 °C). In other studies, for example, Xu *et al.* (2004), kinetic parameters for illite dissolution were used in lieu of those derived directly for glauconite dissolution. Given the small amount (4.4 %) of glauconite in the modeled reservoir and a lack of other quantitative constraints, this assumption had negligible effect on the overall outcome of the simulations. Yet, in rocks where glauconite is more abundant, it would likely lead to significant uncertainties, which may, in turn, propagate into even more significant uncertainties in predictions of carbonate mineral formation. Because the redox state of structural Fe plays an important role in determining the fixation or release of structural K (e.g., Chen *et al.*, 1987; Huang, 2005; Sparks and Huang, 2015; Florence *et al.*, 2017), the

successful assessment of glauconite kinetics in laboratory studies requires controlled redox conditions. To better understand (paleo)environmental changes and improve industrial protocols for GCS in glauconite-rich sedimentary reservoirs, it is critical to constrain the kinetics of glauconite over the wide pH range necessary for rate derivation at relevant temperatures. In Chapter 3, a series of experiments were conducted to determine the dissolution kinetics of glauconite in reservoir temperatures and strictly anaerobic conditions. The results show that glauconite dissolves incongruently under our experimental conditions. Glauconite dissolution rates are temperature dependent, and highly pH dependent in acidic conditions. Chapter 3 has been submitted to *Geochimica et Cosmochimica*. The sample preparation, experiments, data collection and processing, and drafting were by Q. Zhang; fluid samples were analyzed via ICP-OES by M. Nightingale; geochemical modelling, editing and data visualization by A. N. Awolayo; editing and supervision by B. M. Tutolo.

Lastly, an important challenge to the large-scale installation of GCS is the uncertainties in the mineral budget. Despite the large amount of core data collected over decades of hydrocarbon production from glauconite-bearing reservoirs, no attempt has been made to estimate the amount of glauconite, and hence mineral carbonation capacity in relevant subsurface reservoirs. Therefore, constraining the amount of glauconite available in the subsurface for mineral carbonation is a crucial first step for understanding the potential impact of glauconite carbonation on global CO₂ emissions. Chapter 4 has been devoted to quantitatively constrain the availability of glauconite in the Mannville Group in Alberta, Canada, in order to estimate the potential impact of glauconite on the global carbon cycle. Chapter 4 has been accepted by *International Journal of Greenhouse Gas Control* (in press). The data collection, analyses and drafting were conducted by Q. Zhang; edits and supervisions by B.M. Tutolo.

Abstract

Glauconite is an authigenic, iron-rich clay mineral that is abundant in greensands formations worldwide. Evidence from these formations suggests that glauconite is commonly diagenetically converted to carbonate minerals such as siderite, ankerite, and ferroan dolomite. This process represents a natural CO₂ sink that may provide an effective mechanism for the engineered mineralization of anthropogenic CO₂. To evaluate glauconite carbonation reactions and improve our understanding of glauconite diagenesis, we performed a detailed evaluation of the mechanisms through which carbonate minerals naturally replace glauconite during diagenesis of glauconitic sandstones from the Lower Cretaceous Upper Mannville Group in western Alberta, Canada. Using a combination of optical microscopy and scanning electron imaging, electron microprobe and bulk geochemical analyses, and x-ray fluorescence mapping, we show glauconite carbonation in the Mannville Group is a reduction-facilitated, coupled glauconite recrystallization and siderite precipitation reaction. X-ray absorption near-edge spectroscopic mapping and spot analyses demonstrate that this reaction is accompanied by a significant shift in the oxidation state of Fe, from dominantly oxidized in glauconite to reduced in carbonate reaction products. Together, these results suggest that geochemical conditions, most importantly, temperature, partial pressure of CO₂, and fluid redox state were thermodynamically favorable for glauconite carbonation during burial diagenesis of Mannville Group sandstones. Results of thermodynamic models illustrate that, although K-feldspar is favored to precipitate during reductive glauconite dissolution and accompanying Fe-carbonate precipitation, its precipitation is likely kinetically limited, and that an Fe-impoverished glauconite is expected to recrystallize instead. Our findings show that glauconite carbonation is likely a common phenomenon in the subsurface, and thus that glauconite is potentially a significant cation source for mineralizing anthropogenic CO₂.

2.1 Introduction

Iron minerals play an essential role in sedimentary environments because iron is the only common, structure-determining metal that occurs in both reduced (Fe(II)) and oxidized (Fe(III)) valence states (Ireland et al., 1983). Glauconite naturally contains both Fe(II) and Fe(III), thus offering the best prospect for documenting the redox states in diagenetic environments (Berner, 1981; Ireland et al., 1983; Odin, 1988; Odin and Matter, 1981). Formation and alteration of glauconite also provide insights into the long-term sequestration of iron during diagenesis (Baldermann et al., 2015). Glauconite is commonly used to interpret paleoenvironmental conditions due to its global distribution throughout the geologic record, as a result, the diagenesis of glauconite has been studied extensively from a sedimentological perspective (e.g. Odin, 1988; Kronen and Glenn, 2000; Hesselbo and Huggett, 2001; Harding *et al.*, 2014b). Part of these interpretations rely on identifying the alteration stage of glauconite (also known as evolution/development stage): development from nascent to highly evolved glauconite is achieved by a recrystallization process through progressive equilibrium with bottom seawater, which indicates extended residence time at the seafloor prior to burial (Odin and Matter, 1981). However, some sedimentological implications remain open to debate, in part, due to the lack of geochemical constraints on the mechanisms of glauconite diagenesis (Harding et al., 2014). In this study, we explore post-burial carbonation processes as a glauconite alteration mechanism to address these challenges.

2.1.1 Previous Research on Glauconite

The mineral “glauconite” is not recognized by the International Mineralogical Association (IMA). An idealized glauconite composition can be described as $K_{0.75} Fe_{1.25}^{3+} Fe_{0.25}^{2+} Mg_{0.25} Al_{0.5} Si_{3.75} O_{10} (OH)_2$ (Blanc et al., 2015). Although glauconite has been studied extensively, a lack of consistency in terminology has been persistent in published research (e.g., Odin and Matter, 1981; Odin, 1988; Harding et al., 2014). Many terms have been used to identify the green sedimentary mineral, including “glauconite,” “greensands,” “glaucony,” or “glauconitic minerals”. The mineralogical definitions of glauconite vary as well: some define glauconite as a series of micas (Dyar et al., 2008), while others refer to glauconite as an iron-rich variety of the clay mineral illite (Burst, 1958). The term “glauconite” has also been employed as a common field term for small, rounded, green pellets and grains (Odin, 1988). It is possible that no fundamental difference exists amongst these definitions, but rather that they refer to different stages of glauconitization (see below). Regardless, published studies agree that glauconite is abundant in marine greensands formations worldwide (e.g., Baldermann et al., 2015; Bornhold and Giresse, 1985; Jach and Starzec, 2003; Odin, 1988; Odin and Matter, 1981b; Wigley and Compton, 2007). Some lacustrine and alluvial occurrences have also been reported (e.g., McRae, 1972). Glauconite occurs mostly on continental shelves and it is generally widespread on present-day shelves from 50 °S to 65 °N, at water depths between 50 and 500 m, particularly on the upper slope and outer shelf between 200 and 300 m (Odin and Matter, 1981). Glauconite pellets mostly form *in situ*, or are transported over a short distance, because their structures are too weak to sustain extensive transportation (Triplehorn, 1967; Wermund, 1961).

Glauconitization (formation of or conversion into glauconite) results in a continuum of minerals from K-poor, disordered glauconitic smectite to K-rich, ordered glauconitic mica. Stages of alteration are defined by increasing K₂O content, where 2 wt.%–4 wt.% K₂O is nascent stage, 4 wt.%–6 wt.% K₂O is slightly evolved, 6 wt.%–8 wt.% K₂O is evolved, and greater than 8 wt.% K₂O is

highly evolved glauconitic mineral (Harding et al., 2014; Hesselbo and Huggett, 2001; Huggett et al., 2000; Kronen and Glenn, 2000; Odin and Matter, 1981). To investigate natural glauconite carbonation processes, it is important to differentiate the effects of chemical weathering at different stages of glauconitization. For example, Pestitschek et al. (2012) found that fresh glauconite samples are generally dark green, whereas weathered samples are generally olive green to yellowish brownish green coupled with a loss of K and Fe during weathering. On the other hand, Loveland (1981) observed color differences in their samples, but concluded such differences were caused by different stages of glauconitization. Glauconite morphology and internal structure have been studied extensively; dozens of recognized morphological types and internal structures are described in published research (e.g., Triplehorn, 1966). The many different morphologies of the materials which cause the greenish aspect of “greensand” or “greenearth” can schematically be grouped into the granular and the film facies of glauconite (Odin and Matter, 1981).

Glauconite naturally contains Fe in both oxidized (Fe(III)) and reduced (Fe(II)) states. For example, a series of Mossbauer analyses on glauconite from Tunnel City Group in Minnesota, showed that the glauconite contains approximately 80% Fe(III) and 20% Fe(II) (Tutolo et al., 2020a). López-Quirós et al. (2020) suggested that glauconite alteration results in an increase in K as well as an elevated Fe(II)/Fe(III) ratio. Although Fe(III) is often reduced to Fe(II) during diagenesis, which commonly forms siderite (FeCO_3) (McConchie et al., 1979; Tutolo et al., 2020a), little is known about the mechanism by which Fe(III) is reduced. For example, it is unclear whether Fe is reduced while still in the glauconite structure, or after glauconite dissolves, and thus it is inconclusive to whether glauconite development is by “layer-growth mechanism” (López-Quirós et al., 2020) or “precipitation-dissolution-recrystallization mechanism” (Odin and Matter, 1981). Moreover, to guide the engineering efforts that will be critical to exploit glauconite carbonation for geological carbon storage (GCS), the redox states of Fe in glauconite need to be identified. For instance, if

Fe is reduced while still in the glauconite mineral structure, then the approach must be tuned to ensure the transportation of reducing fluids into glauconite grains; if Fe is only reduced after glauconite dissolves, then the approach can be completely solution-based (e.g., reductants added to glauconite-undersaturated reservoir fluids).

2.1.2 The Potential for Carbon Mineralization in Glauconitic Sediments

To combat the devastating effects of anthropogenic climate change, global societies must actively reduce CO₂ emissions to the atmosphere (IPCC, 2021). Continued use of fossil fuels as an energy source, even in an intentionally diminishing capacity, will require technologies for the capture and disposal of CO₂, such as CO₂ storage and mineralization in geologic reservoirs (Bickle, 2009; DePaolo and Cole, 2013; Lackner, 2002; Seifritz, 1990; Zhang and DePaolo, 2017). CO₂ mineralization requires the initial dissolution of gaseous or supercritical CO₂ into water, where it either forms carbonic acid and provokes silicate mineral dissolution or reacts directly with the cation-rich formation fluids. Divalent cations released by silicate mineral dissolution then react with dissolved CO₂ to form stable carbonates. Rock formations with high supplies of divalent cations are therefore crucial for CO₂ mineralization (e.g., Baines and Worden, 2004; Depaolo and Cole, 2013; Zhang and DePaolo, 2017). Potential carbon storage sites need to be closely evaluated to ensure the long-term security, and in order to predict the chemical behavior of CO₂ in storage sites, water-rock interaction processes need to be quantified. Unfortunately, many relevant reactions are sluggish and cannot be simulated effectively over laboratory time scales (e.g., Tutolo et al., 2020). Due to our limited understanding of the subsurface environment, these experiments may be unable to represent the full spectrum of the complexity associated with CO₂-water-rock interactions. Studying sites where natural carbon mineralization has occurred through geological time can provide us with fundamental understanding that permits us to evaluate the long-term chemical behaviors of CO₂ and to eventually guide the design of innovative technology.

Glaucanite is a major framework constituent in many hydrocarbon-producing reservoirs worldwide, such as the Upper Mannville Formation in southern Alberta, Canada (Hayes et al., 1994), the Shannon Sandstone Beds in Wyoming, US (Hansley and Whitney, 1990), Chadra sands in Gialo field, Libya (AlShaieb and Shelton, 1978), the Great Burgan oil field in Kuwait (El-Sharkawi and Al-Awadi, 1982) and the Sacha oil field of Ecuadorian Oriente (Canfield et al., 1982). Since GCS in depleted oil and gas reservoirs is likely the most economical method of GCS (e.g., Bickle, 2009; Li et al., 2006), the abundance of glauconite in these reservoirs has made it an important potential cation source for CO₂ mineralization. Observations of some greensands formations suggest that glauconite is commonly diagenetically converted to carbonate minerals such as siderite, ankerite, and ferroan dolomite (Wermund, 1961; Odin and Matter, 1981; Chafetz, 2007), and a recent experimental study has shown that these reactions are largely controlled by fluid oxidation state (Tutolo et al., 2020). Previous modeling studies on the glauconitic sandstone aquifer in the Alberta Sedimentary Basin suggested mineral sequestration of CO₂ occurs mainly through precipitation of dolomite, with smaller amounts of siderite (Bacon and Murphy, 2011). Harnessing the natural glauconite carbonation processes may thus provide an effective, yet partially overlooked, mechanism for permanent sequestration of anthropogenic CO₂.

In this study, we analyzed a suite of glauconitic sandstone samples from the Early Cretaceous glauconitic sandstone member of the Mannville Group in the Western Canada Sedimentary Basin (WCSB) which exhibit varying amounts of glauconite and post-depositional siderite. This unit was identified as a potential CO₂ storage site in 1996 due to its lithology and proximity to point CO₂ emission sources (Law and Bachu, 1996). Moreover, the lithology of this formation is representative of carbon storage sites in depleted oil reservoirs more generally (Law and Bachu, 1996). The Mannville Group is also an exceptional natural laboratory to study diagenetic carbon mineralization due to the high CO₂ concentration that naturally occurs in the subsurface (Cody and Hutcheon, 1994). Finally, the sedimentology and stratigraphy of the Mannville Group in Alberta has been extensively studied (Abercrombie et al., 1994; Cody and Hutcheon, 1994; Farshori, 1983; Hradsky and Griffin, 1984; Karvonen R.L. and Pemberton, 1989; R. Perry Glaister, 1959; Tilley and Longstaffe, 1984), such that it is amongst the most well-documented glauconitic sandstones in the world. This wealth of information provided us with the necessary background

to characterize the processes that contributed to diagenetic carbonation of glauconite in Mannville rocks. Using an array of techniques, we show that geochemical conditions, most importantly, temperature, partial pressure of CO₂, and fluid redox state were thermodynamically favorable for glauconite carbonation reactions to proceed over the burial history of these rocks, which, in turn, implies that carbonation reactions are an important alteration mechanism of glauconite.

2.2 Methods

2.2.1 *Material*

Mannville Group core samples are publicly accessible and readily available at the Alberta Energy Regulator Core Research Centre in Calgary. The Mannville Group is a Cretaceous stratigraphic unit located in the Western Canada Sedimentary Basin (WCSB); it mainly consists of interbedded continental sand and shale, calcareous sandstone, marine shale, glauconitic sandstone, coal seams and “salt-and-pepper” sandstone (Hayes et al., 1994b). Mannville deposition was initiated in the Early Cretaceous, as accretion of terranes in the western Cordillera compressed passive margin sediments and thrust them onto the continental margin, creating the vast volume of sediments that shed from upthrust sheets into the foredeep. The glauconitic sandstone member formed during the highly episodic transgression and subsequent regression of boreal Moosebar Sea in the southern and central parts of the basin (Christopher, 1984; Hayes et al., 1994b). The rank of coals in sections of the Western Canada Sedimentary Basin demonstrate that the sediments of the Mannville Group were previously buried to greater depths (and temperatures), but that on the order of 1 to 2 km of overburden has subsequently been eroded to bring these rocks closer to the surface (Bustin, 1991; Chiang, 1984). This has implications for the conditions attending glauconite carbonation reactions, as discussed in Sect. 2.2.4. The glauconitic sandstones in this study were sampled from a core interval at 2046-2064 m depth in the Hoadley Pool (04-18-42-03W5), a large conventional/unconventional gas and condensate reservoir within the Mannville Group (Masters, 2020). The rocks in this interval contain the

largest amount of glauconite when compared to the rest of the core. The predominant rock forming minerals include quartz, glauconite (mainly granular facies), dolomite and siderite. Abundant carbonate concretions were identified throughout this interval. Rock samples within the selected core interval were specifically chosen based on features of interest such as carbonate concretions and cements, and/or well-preserved glauconite grains.

2.2.2 Mineral Identification and Chemical Analyses

A standard petrographic microscope was used for initial observations on 9 polished thin sections. Following the optical studies, we selected 3 thin sections with distinctive texture and morphology (at depths 2053.61 m, 2054.33 m and 2055.02 m) to be examined at the University of Calgary by a FEI Quanta 250 Scanning Electron Microscopy (SEM) outfitted with an energy dispersive X-ray spectroscopy (EDX) microanalyser. Glauconite pellets were identified based on the internal texture as well as the EDX spectra. Carbonates (siderite, dolomite and ankerite) were distinguished from one another by EDX spectra coupled with EDX maps highlighting the distribution of Ca, Mg and Fe. Backscattered electron (BSE) imaging was used for mineral identification and secondary electron imaging was used for observations on crystal morphology. A total of 23 glauconite pellets and 18 carbonate crystals and cement were analyzed with a JEOL-JXA-8200 Electron Probe Microanalyzer (EPMA) at the University of Calgary. The EPMA calibration for glauconite measurements was carried out using the following standards of known concentration: augite (for Ca, Si, Mg and Cr), hornblende (for Fe, Al, Na and Ti), rhodonite (for Mn), and orthoclase (for K). The calibration for carbonates measurements was carried out against dolomite (for Ca and Mg), siderite (for Fe), and rhodonite (for Mn) standards. The ZAF correction factors were applied using CITZAF software package and the values were within the range of 0.99 to 1.01 for all the measurements. Multiple measurements were acquired on each glauconite grain and carbonate crystal to eliminate bias due to heterogeneous mineral compositions. Measurements on siderite were divided into two groups, euhedral and anhedral, in order to compare their chemical compositions. Due to the highly friable nature of the chosen samples,

they are difficult to polish effectively. Thus, locations for EPMA analyses were selected to ensure they were located in areas of high polish.

The bulk chemistry of the three rock samples was analyzed at SGS Mineral Services, Canada. The rock samples were pulverized and passed through a 75 μ m sieve. The elemental compositions of bulk rocks were determined by X-ray fluorescence (XRF), with a detection limit of 0.01%. The volatile materials such as combined and free H₂O, CO₂ and organic matter were determined gravimetrically using a multi-stage loss on ignition method. Infrared (IR) Combustion, with a detection limit of 0.01%, was carried out to measure the sulfide content.

The reported results are within 95% confidence intervals.

2.2.3 Redox Characterization by XANES

X-ray Absorption Near-Edge Spectroscopy (XANES) was performed on the Mannville glauconitic sandstone samples from 2053.61 m and 2055.02 m at the Diamond Light Source on the I18 beamline. To locate regions for analysis via XANES spot analyses or mapping, X-ray fluorescence (XRF) mapping was first performed on the analyzed samples at either 10 μ m or 2 μ m resolution, or both, at 7400 eV. For XANES analyses, a double-crystal silicon monochromator in the Si(333) reflection configuration was used to increase the beamline energy resolution compared to the standard Si(111) configuration. Energy calibration was confirmed by measuring Fe metal foil, and all data collection was performed in fluorescence mode with samples positioned at a 45° angle from the incident beam.

XANES spot analyses were acquired over the energy range 7020 eV-7400 eV: 7020-7100 eV at 10 eV steps; 7100-7118 at 0.1 eV steps; 7118-7200 eV at 1 eV steps; 7200-7300 at 10 eV steps; and 7300-7400 eV at 10 eV steps. Counting times of 3 seconds were used in the pre-edge region (7100-7118 eV); counting times of 1 second were used elsewhere. For XANES mapping, 0.05 s count times were used, with the following spacing: 7050-7100 eV at steps of 10 eV; 7100-7110 at steps of 5 eV; 7110-7118 at steps of 0.2 eV; 7118-7130 at steps of 1 eV steps; 7130-7150 at steps of 2 eV; 7150-7200 at steps of 5 eV steps; and 7200-7300 at steps of 10 eV steps. XANES mapping was performed at a spatial resolution of 2 μ m. Prior studies (Andreani et al., 2013;

Luhmann et al., 2017; Marcaillou et al., 2011; Wilke et al., 2001) have shown that the centroid of the pre-edge region can be used as a quantitative measure of the oxidation state of Fe in serpentinites, provided that Fe(II) and Fe(III)-bearing model compounds are additionally analyzed for calibration purposes. Following the guidelines put forth by these authors, we processed our spectra by first subtracting the average of the background absorbance acquired between 7000 and 7050 eV (for spot analyses) or 7100 eV (for maps), and then normalizing the intensity to the average absorbance measured above 7250 eV. Pre-edge features were extracted by subtracting a 3-term Gaussian function fit to the normalized absorbance measured above and below the features, whose positions changed depending on the bulk oxidation state of the analyzed sample. This process was done with the Matlab[®] `cftool` function, which permitted visual inspection and inclusion/exclusion of points to ensure accurate subtraction. The pre-edge features were then fit using the `peakfit.m` function (O’Haver, 2018), assuming 4 fixed-width (1.5 eV) Gauss-Lorentz components (Marcaillou et al., 2011) and compared to fits of spectra acquired on ^[VI]Fe(II)-bearing San Carlos olivine (NMNH 111312-44), ^[IV]Fe(II)-bearing staurolite (NMNH 117183), ^[VI]Fe(III)-bearing andradite (NMNH 166396), and ^[IV]Fe(III)-bearing plagioclase (NMNH 115900) provided by the Smithsonian Institution National Museum of Natural History. These materials represent the endmembers in a variogram interpretation of oxidation state (after Wilke et al. (2001)); identical analyses of the average spectra at 10% intervals between the standards (e.g., the sum of 10% San Carlos olivine spectrum and 90% of the andradite spectrum) were also performed to provide an indication of the variation in oxidation state between endmembers, which can be non-linear. XANES maps were processed using the Mantis software package (Lerotic et al., 2014). As described in Lerotic et al. (2014), the full, pre-normalized (by the Mantis software) XANES spectra were subjected to Principal Components Analysis, and then a cluster analysis was performed to group pixels with similar spectra. In all cases, five significant components were determined by Mantis during the PCA step, and thus five clusters were used to group pixels with similar spectra. These clusters are plotted Figure 2-8. The spectra corresponding to these clusters were analyzed in the same manner as the point spectra and are plotted in Figure 2-8 to demonstrate the variation in Fe oxidation state between individual clusters. Fits of the XANES spectra are given in the supplementary data, and the full XANES spectra are uploaded to the Open Science

Framework. Although previous authors (e.g., Andreani et al., 2013) have suggested the uncertainty on the variogram interpretation of Fe redox state is on the order of $\pm 5\%$, more recent interpretations based on coupled Mossbauer and XANES analyses of and/or wet chemistry analyses of amphiboles and serpentines suggest that an estimated uncertainty on the order of 15-20% absolute Fe(III)/^PFe is more appropriate (Dyar et al., 2016; Ellison et al., 2020). Considering the excitation depths of XANES analyses and the angle of presentation of the samples to the x-ray beam, it is likely that the spatial area probed by the analyses is greater than the 2 μ m step size. Indeed, although it is difficult to accurately constrain, the true spatial resolution may conservatively be estimated to be closer to 1020 μ m. Since the analyses necessarily probe the redox state of all Fe contained within the analyzed volume, sharp interfaces in Fe redox state of the analyzed sample may result in spectral mixing at the analyzed scale (similar to calculated mixtures between variogram endmembers discussed above). Nevertheless, the pre-edge features of the spectra still represent the average redox state of the analyzed volume, and thus conclusions regarding the spatial variation in redox state remain valid, just at a slightly coarser scale. Taking into account both this uncertainty on the XANES analyses and the relatively loose level of accuracy required to draw conclusions regarding Fe redox transformations during glauconite diagenesis, we decided to use qualitative comparisons of our XANES analyses, rather than reporting absolute values of Fe oxidation state, below.

2.2.4 *Geochemical Modeling*

In addition to the geochemical characterization of glauconite carbonation in Mannville sediments, this study aims to develop a conceptual geochemical model for the CO₂-water-rock interactions of the Mannville Group glauconitic sandstone. The modeling was carried out using the Geochemist's Workbench (GWB) software package (Bethke et al., 2018) with a custom thermodynamic database created using the DBCreate (Kong et al., 2013) software package (more details below). To guide reaction path modeling efforts and provide a general overview of the geochemical controls on glauconite carbonation reactions, we first made an activity diagram examining mineral stability in Mannville sediments as a function of oxygen fugacity ($fO_2(g)$) and pH. Following on a previous study of diagenesis in Mannville sediments (Cody and Hutcheon, 1994), we constructed the diagram assuming 1 μ molal Fe and S, 1 mmolal K and Mg, 100 mmolal

NaCl, and 1 molal C, with $a_{\text{SiO}_2(\text{aq})}$ set by equilibrium with respect to chalcedony, $a_{\text{Al}^{+++}}$ set by equilibrium with respect to kaolinite, and $a_{\text{Ca}^{++}}$ set by equilibrium with respect to dolomite. We produced this activity diagram at 35 °C, which is representative of temperatures in the Mannville sediments (Cody and Hutcheon, 1994). The topology of this diagram remains unchanged if deeper burial temperatures up to 85 °C are assumed, and we thus rely on this 35 °C to guide the discussion.

We also simulated the reaction between glauconite and Mannville reservoir fluids using a reaction path model. Water chemistry data from a well near the sample location (Table 2-1), which is sample 4-21-12-16W4 reported by Cody and Hutcheon (1994)) and an estimated average temperature (~35°C) were used to parameterize the model. We assumed that carbonate alkalinity is equivalent to HCO_3^- concentration at this pH. This fluid chemistry yields a calculated CO_2 fugacity ($f\text{CO}_2$) of 0.24, a value which is well within the range of $f\text{CO}_2$ reported by Cody and Hutcheon (1994). Consistent with the abundance of gas in the Mannville formation, we assumed that this fugacity was fixed throughout

the simulated reaction. Cody and Hutcheon (1994) demonstrated that SO_4^{2-} and HS^- are in disequilibrium in Mannville reservoir fluids. Rather, those authors showed that equilibrium between acetate (CH_3COO^-) and HCO_3^- , a reaction that had previously been hypothesized by Helgeson et al. (1993) to control reservoir fluid redox state, more closely approximated the oxidation state of the reservoir fluids. Indeed, $f\text{O}_2(\text{g})$ calculated from the Cody and Hutcheon (1994) data set plot in very close agreement with the empirical correlation presented by Helgeson et al. (1993). Unfortunately, Cody and Hutcheon (1994) do not present concentrations of CH_3COO^- for the sample presented in Table 2-1, and we therefore chose to use the empirical correlation presented by Helgeson et al. (1993) to calculate $\log f\text{O}_2(\text{g})$. This procedure yielded a value of ~-73, which was fixed throughout the reaction path simulation, in keeping with the external buffering of redox by organic-inorganic carbon reactions (Helgeson et al., 1993; Cody and Hutcheon, 1994). Likewise, to ensure that our simulations adhered to both the mass balance constraints on dissolved inorganic carbon provided by Cody and Hutcheon (1994) and redox constraints provided by the inorganic-organic correlation of Helgeson et al. (1993), we assumed that dissolved C did not undergo oxidation or reduction during our simulation. Consistent with

the S disequilibria reported by Cody and Hutcheon (1994) and the external buffering of redox by organic-inorganic equilibria, we assumed that dissolved S did not undergo oxidation or reduction over the course of our simulations. Because, even with modification, pyrite was still highly supersaturated in the sample reported by Cody and Hutcheon (1994), we set the initial $a_{\text{Fe}^{++}}$ to be in equilibrium with pyrite. Additionally, because Al concentrations were not reported by Cody and Hutcheon (1994) (likely because they were below detection limits), we assumed that $a_{\text{Al}^{+++}}$ was set by equilibrium with respect to kaolinite, consistent with its presence in our samples. Finally, we assumed that chalcedony, and not quartz, was the dominant silica phase precipitating at the low temperatures of our reaction, consistent with Arnórsson et al. (1983) and Cody and Hutcheon (1994). The reaction path simulation was run by first calculating the system's initial equilibrium state and then adding 0.1 kg of glauconite to 1 kg of solution, ultimately yielding a water-to-rock ratio of ~ 10 , a value which is consistent with the limited extents of reaction observed in our samples. Other dominant primary minerals in the Mannville samples (quartz and dolomite) were supersaturated during the simulations and thus assumed unreactive.

Table 2-1 Water chemistry data (Cody and Hutcheon, 1994) and calculated gas fugacity (Sect.2.2.4) used to simulate the reaction between 0.1 kg glauconite and Mannville reservoir fluids at 35 °C.

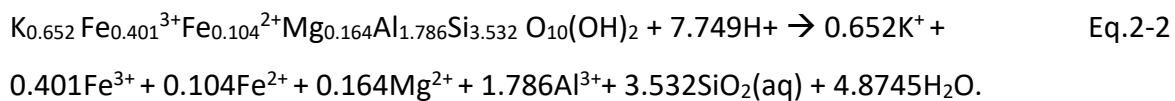
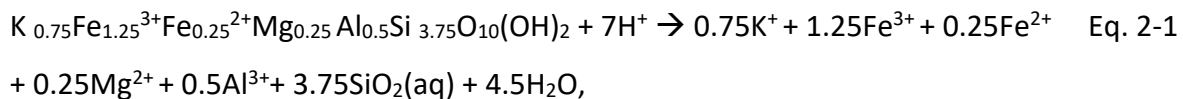
The initial activities of Fe^{++} and Al^{+++} were set by equilibrium with pyrite and kaolinite, respectively. and dolomite) were supersaturated during the simulations and thus assumed unreactive.

Location	4-21-12-16W4
pH	7.09
Li (mg/L)	4.07
Na (mg/L)	2850.0
Mg (mg/L)	19.9
K (mg/L)	71.6
Ca (mg/L)	59.4
Fe (mg/L)	0.18
SiO ₂ (mg/L)	13.35
Cl (mg/L)	1378.0
SO ₄ (mg/L)	227.6
HS ⁻ (mg/L)	106.0
Alk (meq/L)	92.1
Alkc (meq/L)	88.1
Fe (mmol/kg)	10 ⁻²⁵
Al (mmol/kg)	10 ⁻²⁰
log fO ₂ (g)	-73

2.2.5 Thermodynamic Data for Geochemical Calculations

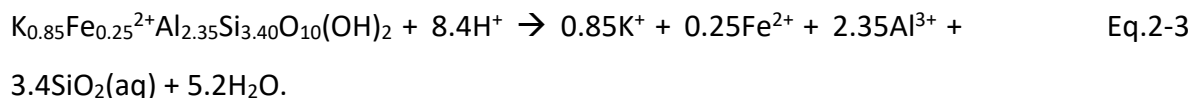
As previously discussed by Tutolo et al. (2020), there are very few sources of thermodynamic data for the clay mineral glauconite at the heart of the present study, and, as discussed above (Sect. 2.1.1), the chemical variability of glauconite dictates that the thermodynamic properties of glauconites will range quite widely, depending on their individual compositions. For example, Blanc et al. (2015) presented a set of calculated thermodynamic properties of an “ideal” glauconite, but, because the composition of this “ideal” glauconite is significantly different than that of the Mannville glauconite, we cannot adopt these parameters directly and expect accurate

results. Thus, we calculated the thermodynamic properties specific to the Mannville Group glauconite using the methods outlined by Blanc et al. (2015) using calculation techniques previously developed by Tutolo et al. (2020) (Table 2-2). The generalized mineral thermodynamic property prediction model presented by Blanc et al. (2015) utilizes the electronegativity scale model developed by Vieillard (1994a,b) to predict enthalpy, and calculates molar entropy (S°), volume (V°), and heat capacity (C_p°) using a polyhedral decomposition model comparable to that employed by Holland (1989) and Chermak and Rimstidt (1989, 1990). Due to the lack of measured data, the maximum values of both the magnetic (S° mag) and the configurational (S° conf) entropy terms are estimated using the methods outlined by Ulbrich and Waldbaum (1976). The equilibrium constants for calculating the solubility of glauconite as a function of temperature at steam saturation conditions (Table 2-3), were calculated with respect to Reactions 1 and 2. The glauconite dissolution reaction of the “ideal” glauconite (Blanc et al., 2015) and the Mannville Group glauconite dissolution reaction can be described by:



Moreover, we incorporated the thermodynamic properties of Fe(II)-illite (Blanc et al., 2015) in our models (Table 2-2 and Table 2-3), the reasons are discussed in Sect. 2.2.4.

The dissolution reaction of Fe(II)-illite is described by:



The values of the resulting equilibrium constants for Reactions 1-3 are incorporated in Table 2-3. In addition to these phyllosilicates, we also calculated equilibrium constants for the mineral ankerite ($\text{CaFe}(\text{CO}_3)_2$) using thermodynamic properties presented by Holland and Powell (2011) and incorporated them into our geochemical thermodynamic database. All aqueous geochemical

species used to calculate equilibrium constants are consistent with the thermodynamic databases used by Tutolo et al. (2014), Tutolo et al. (2015) and Tutolo et al. (2020a). A thermodynamic database for the Geochemist's Workbench (GWB) (Bethke and Yeakel, 2018) was produced using the DBCreate software package (Kong et al., 2013) at temperatures from 0 to 300 °C and steam saturation pressure. At the low temperatures relevant to our study, pressure has a negligible effect on calculated aqueous equilibria (e.g., Helgeson et al., 1993), which justifies the use of steam saturation pressure rather than the elevated pressures encountered at the current burial and ancient depths of the Mannville formation.

2.3 Results

2.3.1 Petrography

Overall, the glauconitic sandstones studied are well to moderately sorted, and well to moderately rounded, grain-supported, with point and concavoconvex inter-granular contacts (Figure 2-1a and Figure 2-3a). Various degrees of alteration and dissolution are observed in glauconite. Partially dissolved glauconite grains are commonly found encroached by microcrystalline siderite (Figure 2-3a). Siderite is a common coating material on almost all mineral grains (Figure 2-1a and Figure 2-3a,b). Dolomite occurs both as primary framework grains and as replacement material of glauconite (Figure 2-3 a). A small amount of pore-filling kaolinite was identified (Figure 2-1c). The majority of glauconite in the samples examined are granular facies, spheroidal or ovoidal pellets with randomly orientated quartz fragments inside; only a few film facies have been observed (Figure 2-1a).

Composite glauconite grains in which the clayey matrix of the rock fragments has been glauconitized while the original shape of the grain is unchanged were identified in some samples (Figure 2-1b). The rock fragments included in the composite grain are pyrite and quartz. Composite glauconite grains are often embedded in siderite cement (Figure 2-1a and Appendix A-S7). The siderite cement consists of randomly-oriented euhedral siderite rhombs as well as

massive clusters of anhedral siderite grains. Euhedral pyrite is identified in the composite grain as rock fragments, while framboidal pyrite is only found outside of the composite glauconite. Almost all of the framework minerals show some degree of replacement, following the criteria to identify mineral replacement by Wermund (1961): hazy grain margins where siderite rhombs fade into the host minerals (Figure 2-1 c and Figure 2-3a, b), intrusions and veinlets of siderite into quartz and glauconite (Figure 2-3a, b), and siderite rims along dolomite crystal boundaries (Figure 2-1c and Figure 2-3a, b). Dolomite and siderite replacement of glauconite are both common in the samples. The dolomite-glauconite interfaces (Figure 2-2a and Figure 2-3c) show no evident dissolution (no hazy margins) of glauconite grains. The euhedral dolomite crystal faces are in planar contact with the glauconite grains and appear to have grown into them. The dolomite tends to have a higher iron concentration along the contact boundaries with glauconite (Figure 2-2a,b). The siderite-glauconite interfaces most commonly involve a hazy glauconite margin (e.g., Figure 2-3b), however, planar contacts were also identified (Figure 2-2d). The clastic grains (quartz and glauconite) in the ankerite concretion (Figure 2-4a) exhibit corrosion fronts indicated by hazy grain boundaries. A layer of recrystallization shown in darker grey was also observed in the large glauconite grain in the center of the image (Figure 2-4a). The concretion is matrix-supported, and the matrix has a homogeneous texture. The elemental distribution is heterogeneous throughout the concretion (Figure 2-4b-d), but the variation appears to be random with no center-to-edge variations. It appears as though the matrix was precipitated early as a cement that protected the granules from compaction and thus preserved a “floating-grain” texture (Marshall and Pirrie, 2013).

Table 2-2 Calculation values for the thermodynamic properties of minerals (25°C, 1 atm)

Mineral	$\Delta G^{\circ f}$ kJ/mol	$\Delta H^{\circ f}$ kJ/mol	$S^{\circ lat}$ J/mol/ K	$S^{\circ conf}$ J/mol/ K	$S^{\circ mag}$ J/mol/ K	S° J/mol/ K	V° cm ³ /mol	a J/mol/K	b J/mol/K ²	c JK/mol
Glt^a (Ideal)	-4800.11	-5151.13	314.92	29.69	27.91	366.58	139.75	335.659 4	288.937 4	-68.68
Glt^b (Mannville)	-5222.10	-5881.70	283.20	36.91	7.37	327.47	137.73	288.937 4	220.981 7	-66.92
Fe(II)-illite^c	-5351.38	-5796.29	292.22				140.67			

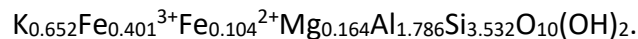
^a K_{0.75}Fe³⁺_{1.25}Fe²⁺_{0.25}Mg_{0.25}Al_{0.5}Si_{3.75}O₁₀(OH)₂ (Blanc et al., 2015); a,b,c this study
^b K_{0.652}Fe_{0.401}Fe_{0.104}Mg_{0.164}Al_{1.786}Si_{3.532}O₁₀(OH)₂ (this study)
^c K_{0.85}Fe²⁺_{0.25}Al_{2.35}Si_{3.40}O₁₀(OH)₂ (Blanc et al., 2015)

Table 2-3 Equilibrium constants for calculating the solubility of minerals as a function of temperature at steam saturation conditions (reactions shown as Eq.2-2 and Eq.2-3).

Minerals	logK (0.01°C)	logK (25°C)	logK (60 °C)	logK (100 °C)	logK (150 °C)	logK (200 °C)	logK (250 °C)	logK (300 °C)
Glt (“Ideal”)	4.5595	2.0699	-0.6483	-2.9905	-5.2112	-7.0043	-8.6490	-10.4076
Glt (Mannville)	8.3820	5.0455	1.3208	-1.9677	-5.1512	-7.7378	-10.0602	-12.4098
Fe-illite	13.2994	9.4697	5.1620	1.3275	-2.4107	-5.4544	-8.1682	-10.8624

2.3.2 Chemical Analyses

The calculated structural formula of glauconite based on the average chemical concentrations from the EPMA measurements (Table 2-4 & Table 2-5), charge balance assuming Fe(II) and Fe(III) both occur on the octahedral site, Al(III) occurs on both octahedral and tetrahedral sites, and no trioctahedral substitution between Fe(II) and Mg(II) occurs) is:



Amongst the measured glauconite pellets, Fe and Al concentrations show the most significant variations (Table 2-4 and Figure 2-5). All of the glauconite pellets contain 7-8 % K₂O. The analyzed

dolomites show very little Mn substitution. The Fe and Mg contents vary greatly amongst analyses. It is evident that the dolomite rims (e.g., Figure 2-2b) have much higher Fe content than the core (Table 2-5). The anhedral siderite, on average, has a lower Fe content and a greater Ca substitution than the euhedral siderite crystals formed around glauconite grains (Table 2-5). Both the euhedral and anhedral siderite has 4-8 % Mg and very little Mn substitution.

The bulk rock chemical analyses (Table 2-6) showed the chemical compositions are nearly identical between the samples from 2054.33 m and 2055.02 m, while the 2053.61 m sample consists of more Fe and less Mg and Ca. This variation is caused by different framework grain assemblies, which is consistent with the petrographic observations: 2053.61 m consists of mainly quartz, glauconite and little dolomite (Figure 2-3), while the other two samples contain much more dolomite (Figure 2-2) or ankerite (Figure 2-4). All three samples exhibit low Al (< 5%) and S (< 1%) contents, suggesting small amounts of Al-silicates and pyrite, respectively, which is also consistent with the petrographic observations. Due to the lack of organic matter, the LOI can most likely be attributed to structurally bound OH in glauconite and CO₃ in carbonates.

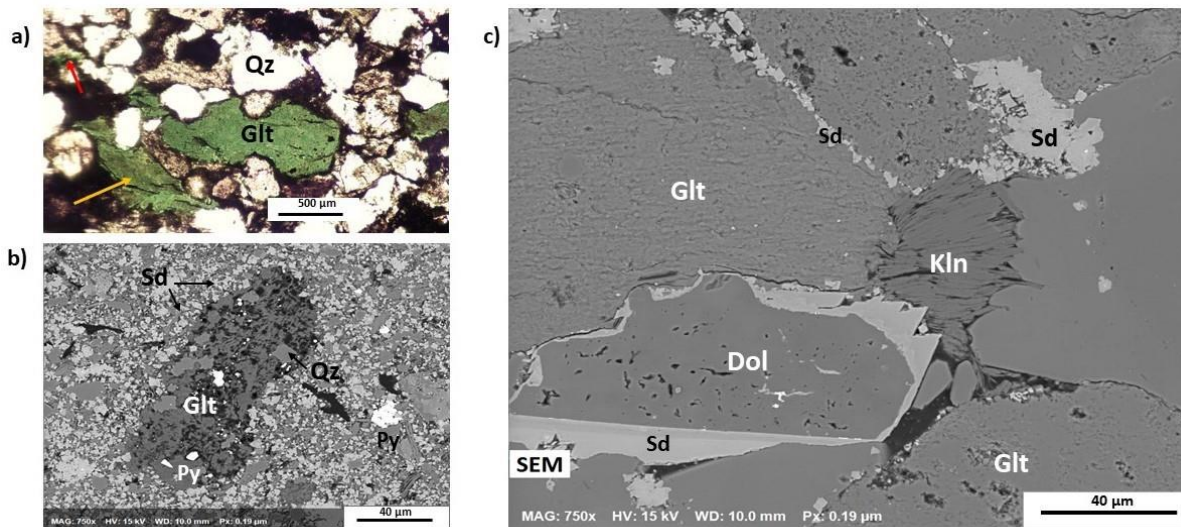


Figure 2-1 Mineral distributions of the Mannville glauconitic sandstone (2054.33 m).

- a) The glauconitic sandstone under plane polarized light; the glauconite (Glt) grain in the center exhibits an intense green color, while the one of the left (yellow arrow) exhibits an olive-green color, indicating different stages of alteration. The glauconite grains are weakly pleochroic,

minimal color change is observed at different angles. Glauconite as grain coating is also identified (red arrow).

b) Back-scattered SEM image of a composite glauconite (Glt): the clayey matrix of the rock fragments has been glauconitized while the original shape of the grain is unchanged; the original rock fragments include euhedral pyrite (Py, white) and quartz (Qz, dark grey). Microcrystalline siderite (Sd, light grey) makes up the majority of the cement of the rock. Framboidal pyrite (Py, lower right corner) is present in the siderite cement.

c) Back-scattered SEM image of siderite (Sd) and dolomite (Dol) replacement of glauconite (Glt). Siderite predominantly formed along the margins of glauconite. The dolomite (Dol) has a rim of siderite. The pore-filling kaolinite (Kln) exhibits a clear “booklet” structure.

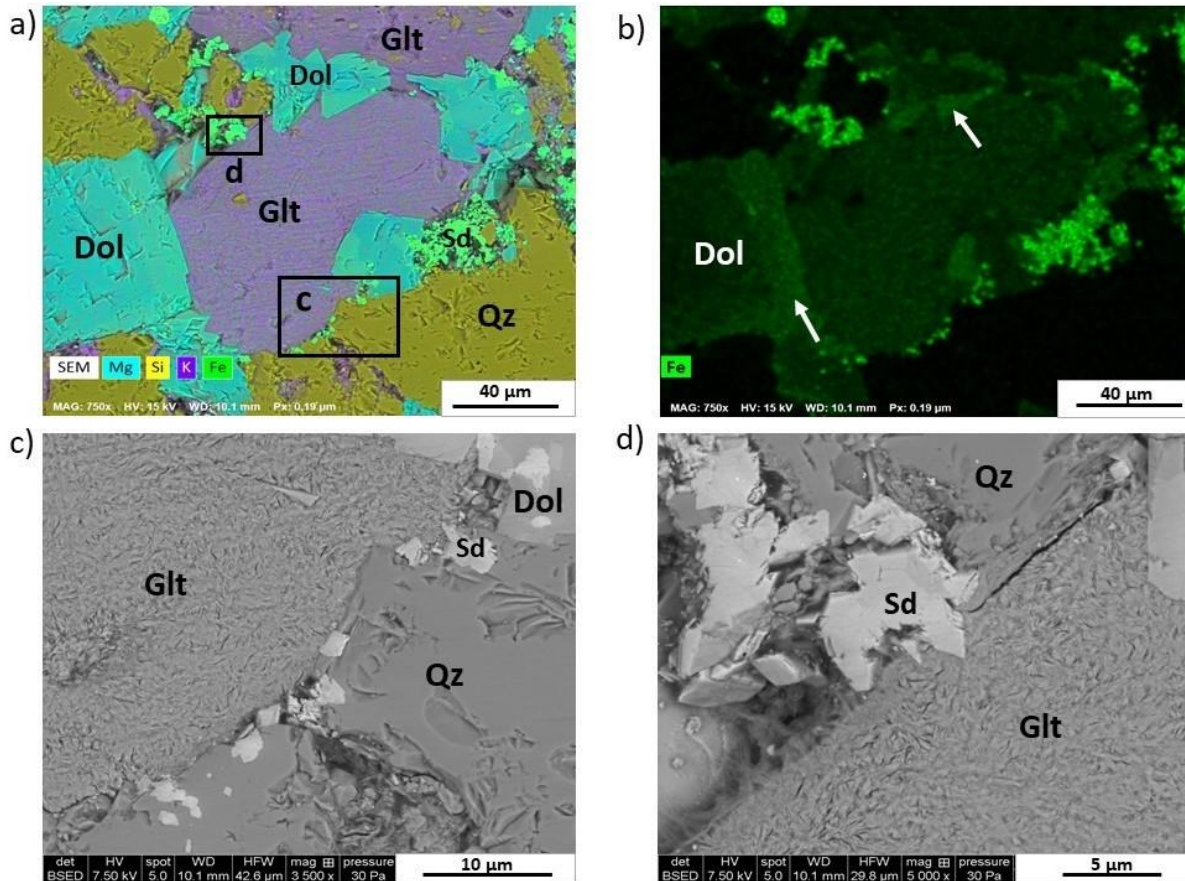


Figure 2-2 SEM images and energy dispersive spectrometry maps of element distribution in the Mannville glauconitic sandstone (2055.02 m).

a) Energy dispersive spectrometry map of element distribution in the glauconitic sandstone. Dolomite (Dol) crystals have higher Fe (greener) concentration along the contact with glauconite (Glt). The locations of SEM images c and d are marked with black boxes.

b) Energy dispersive spectrometry map highlighting Fe distribution (ingreen), in the same area as Image a. Note the Fe-rich rims of dolomite (arrows).

c) Back-scattered SEM image of quartz (Qz) and glauconite (Glt) replaced by euhedral siderite (Sd) crystals. The glauconite exhibits a lamellar nanostructure.

d) Back-scattered SEM image of glauconite (Glt) replaced by Siderite (Sd). Note the clear contact between the siderite and glauconite grain.

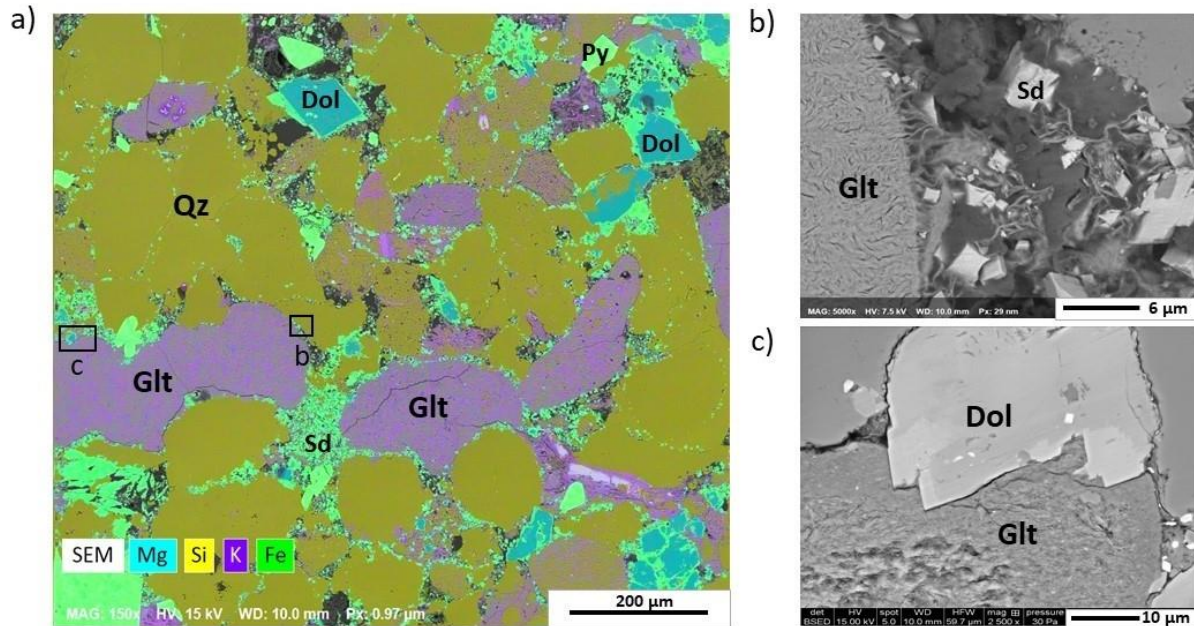


Figure 2-3 Energy dispersive spectrometry map of element distribution and SEM images of the Mannville glauconitic sandstone (2053.61 m).

- a) Indented glauconite (Glt) grains are formed due to intergranular pressure solution in the sandstone. Microcrystalline siderite (Sd, green) precipitated along most grain boundaries and ruptures of glauconite and quartz. Almost every dolomite grain (Dol) has a siderite rim. The locations of SEM images b and c are marked with black boxes.
- b) Secondary electrons image of a “hazy” margin of glauconite (Glt) grain and euhedral siderite (Sd) crystals. The glauconite exhibits a lamellar nanostructure that is commonly found in evolved glauconite.
- c) Back-scattered SEM image of glauconite (Glt) replaced by a rhombohedron of dolomite (Dol). Note the clear contact between the two grains.

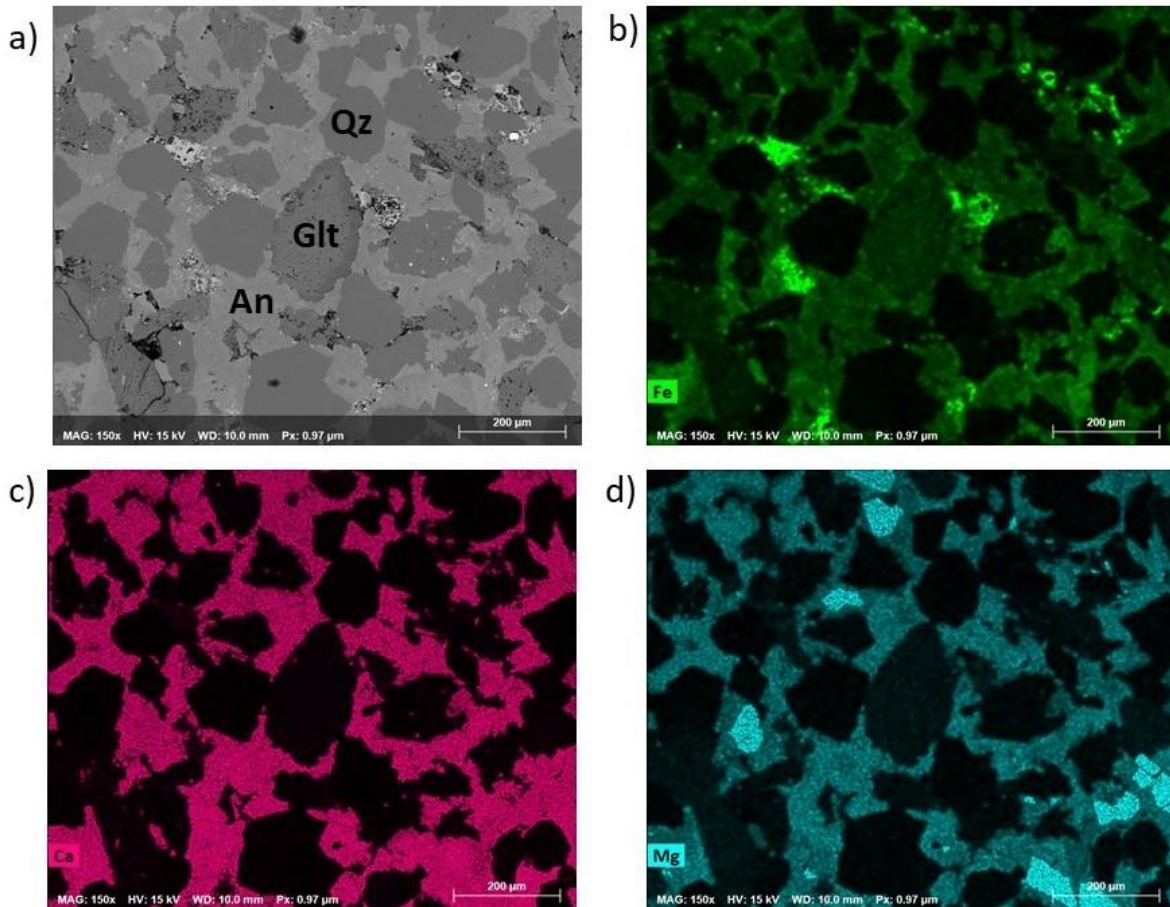


Figure 2-4 SEM images and energy dispersive spectrometry maps of element distribution in the Mannville glauconitic sandstone (2054.33 m).

a) Back-scattered SEM image of an ankerite concretion (2054.33 m). The quartz grains exhibit “hazy” outlines and appear to be “floating” in the concretion. Corrosion front is evident in both quartz and glauconite grains. A layer of recrystallization is observed in the glauconite grain in the center of the image.

b-d) Energy dispersive spectrometry maps highlighting Fe, Ca and Mg distributions.

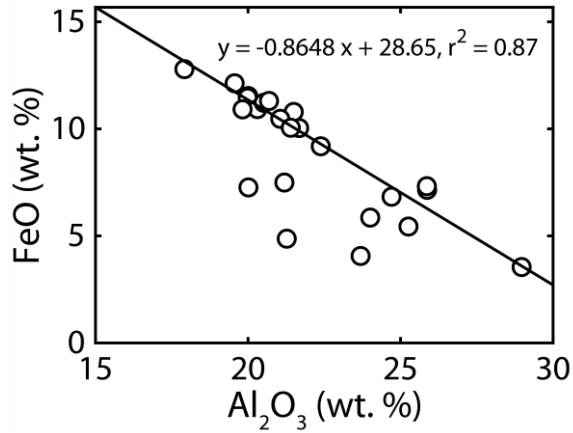


Figure 2-5 Al and Fe contents in the EPMA analyses on glauconite grains (data provided in supplementary material).

Table 2-4 Maximum, minimum, mean and standard deviation of EPMA analyses (Oxide wt.%) of glauconite pellets from Mannville Group, n=23, Fe was analyzed as Fe²⁺.

Oxides	Range	Mean ± SD
SiO ₂	49.8 - 53.5	51.8 ± 1.0
TiO ₂	0.09 - 0.3	0.1 ± 0.06
Al ₂ O ₃	19.6 - 29.0	22.2 ± 2.9
CaO	0.2 - 0.6	0.4 ± 0.09
MnO	0.0 - 0.03	0.006 ± 0.008
FeO	3.5 - 12.1	9.6 ± 2.5
K ₂ O	7.4 - 8.1	7.7 ± 0.2
Na ₂ O	0.02 - 0.2	0.1 ± 0.05
MgO	1.0 - 2.0	1.7 ± 0.2

Table 2-5 Maximums, minimums, means and standard deviations of EPMA chemical analyses (in oxides wt.%) of dolomite (dol) crystals with heterogeneous rims, n=10 (core), and n=3 (rim); and siderite (sd) crystals, n=8 (euhedral), and n=3 (anhedral).

Oxides	CaO	MnO	FeO	MgO	CO ₂
Dol(core)	30.3 - 32.4	0.0 - 0.2	0.2 - 14.1	10.1 - 22.0	45.3 - 47.1
Mean ± SD	31.2 ± 0.8	0.07 ± 0.06	4.3 ± 4.8	17.7 ± 4.7	46.6 ± 0.5
Dol(rim)	27.3 - 33.2	0.1 - 0.3	0.3 - 17.6	6.1 - 22.5	43.9 - 47.4
Mean ± SD	29.5 ± 2.6	0.2 ± 0.1	12.5 ± 8.7	12.0 ± 7.5	45.8 ± 1.4
Sd(eu)	0.6 - 6.7	0.2 - 1.1	44.1 - 56.0	0.8 - 8.3	40.0 - 46.7
Mean ± SD	2.9 ± 1.6	0.7 ± 0.2	49.8 ± 4.3	4.2 ± 2.7	42.3 ± 2.0
Sd(an)	3.4-7.0	0.5 - 0.9	45.1 - 53.5	1.4 - 7.2	40.9 - 42.6
Mean ± SD	5.1 ± 1.5	0.7 ± 0.2	47.9 ± 3.9	4.3 ± 2.3	42.0 ± 0.8

2.3.3 Iron Redox during Glauconite Carbonation

The locations of XANES spot analyses and maps on samples 2053.61 m and 2055.02 m are marked on the XRF maps (Figure 2-6). Spot 1 is on a quartz grain. Spots 2-6 are on microcrystalline siderite shown in Figure 2-3. Spots 15, 16 and 17 are in the center of a glauconite grain, while spots 13 and 14 are on the edge of the glauconite grain where siderite grows into it. Spots 18-20 represent the Fe-rich rims and veinlets in dolomite grains. The pre-edge centroid energy directly depends on the Fe redox state, where the respective centroids for Fe(II) and Fe(III) are separated by 1.4 eV (Wilke et al., 2001). Moreover, the variations in pre-edge intensity may be attributed to octahedral site distortions or to the presence of tetrahedral iron (e.g., Wilke et al., 2001; Andreani et al., 2013). Processed XANES spot analyses illustrating the range of Fe oxidation states (Figure 2-7) suggests that, within error (discussed in Sect. 2.2.3), oxidized Fe(III) is mainly concentrated

in the center of the glauconite grains (Spots 15-17), while the rest of the spots consist of mainly reduced Fe(II). XANES Maps (Figure 2-8a, b, c and e) all focused on the reaction fronts where glauconite dissolution and siderite precipitation occurred. These maps and the accompanying plots of the pre-edge characteristics of the spectra for the derived clusters suggest a transition from dominantly Fe(III) to dominantly Fe(II) near individual glauconite grain boundaries. Map d illustrates a dolomite grain with a siderite rim in contact with a glauconite grain. The Fe in the dolomite grain and the surrounding siderite is generally reduced, although some oxidized Fe was detected associated with the quartz in the background.

2.3.4 Geochemical Modeling

The constructed activity diagram (Figure 2-9) illustrates the stability fields of the Fe minerals in the Mannville Group. Regardless of pH, pyrite dominates at the most reducing conditions, including those relevant to Mannville Group pore fluids. Moreover, glauconite is only stable relative to siderite and pyrite at relatively oxidizing, elevated pH conditions, with siderite occupying similar redox conditions at more circumneutral pH. At the most oxidizing conditions, hematite dominates, although all minerals are highly soluble under acidic, oxidizing conditions. Consistent with Figure 2-9, the reaction path simulations (Figure 2-10) show that, at the redox and pH conditions of this calculation (Sect. 2.2.4), the Mannville glauconite is thermodynamically unstable. Glauconite dissolution into Mannville pore fluids thus produces siderite, K-feldspar (Figure 2-10a), or Fe(II)illite (Figure 2-10b) (discussed in Sect. 2.4.1.3), kaolinite, and chalcedony along with small and varying amounts of dolomite, ankerite, and pyrite, depending on reaction progress. Fe derived from glauconite dissolution initially precipitates as pyrite, which consumes sulfide and lowers its activity. This allows ankerite and siderite to precipitate as they reach saturation. In the second simulation, we suppressed the precipitation of K-feldspar. Throughout this reaction sequence, Fe(II)-illite (which is equivalent to a recrystallized glauconite, as

mentioned in Sect. 2.1.1) is precipitated instead of K-feldspar while the precipitation of siderite remains almost completely identical to the first simulation in which K-feldspar was allowed to precipitate. Excess Al and some Si are precipitated as kaolinite, and excess Si is precipitated as chalcedony.

Table 2-6 Elemental compositions of bulk rocks (oxides wt.%), major elements measured by XRF, S measured by IR combustion, LOI = loss on ignition.

Depth (m)	LOI	SiO ₂	Al ₂ O ₃	Fe ₂ O ₃	MgO	CaO	K ₂ O	Na ₂ O	TiO ₂	MnO	S	P ₂ O ₅
2053.61	14.8	53.2	4.61	18.6	2.52	2.92	1.33	0.23	0.22	0.27	0.837	0.25
2054.33	18.7	51.7	3.25	6.46	5.17	12.6	0.91	0.16	0.18	0.07	0.262	0.19
2055.02	19.9	49.7	3.14	6.83	5.39	13.2	0.86	0.14	0.17	0.08	0.172	0.19

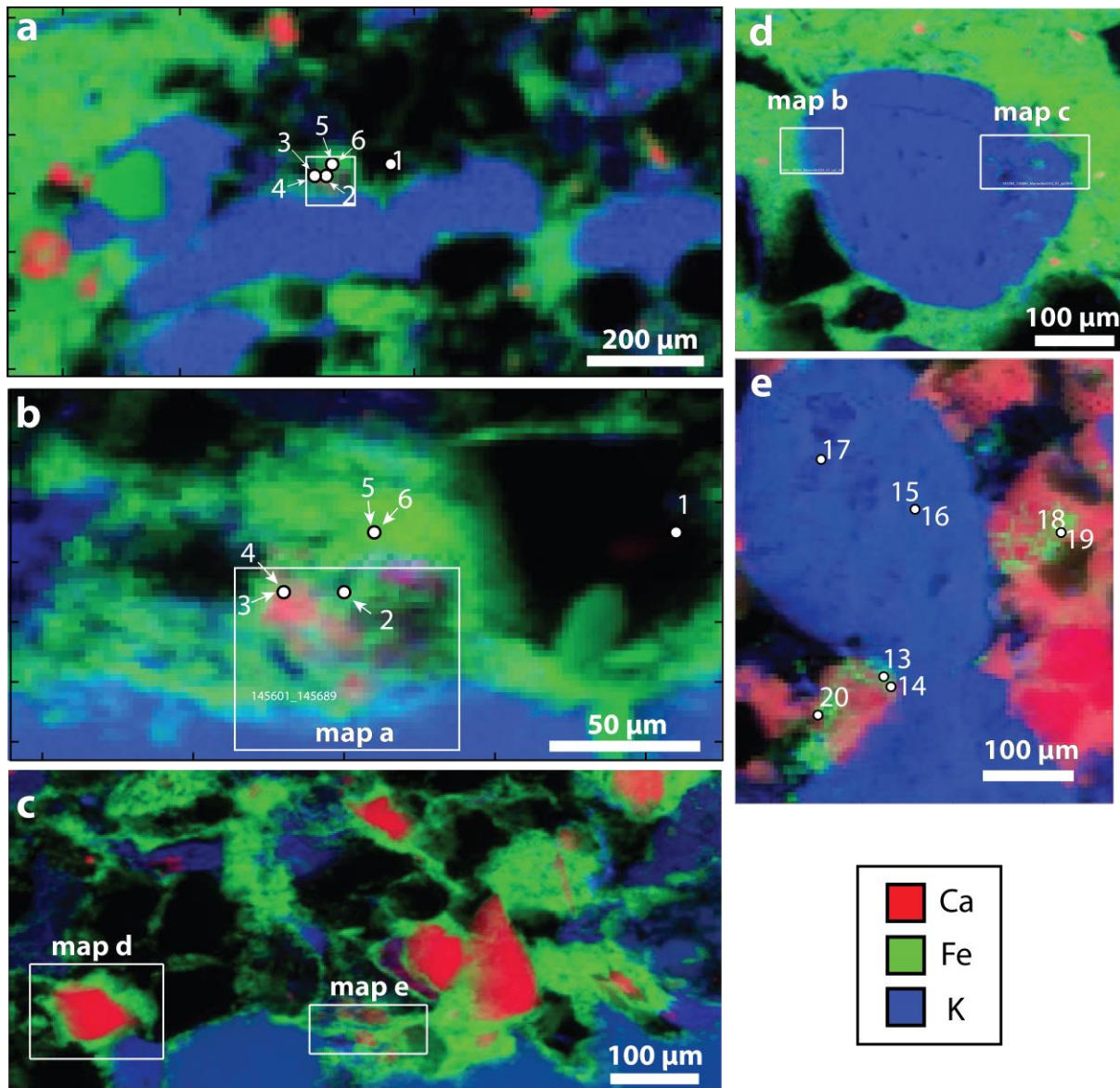


Figure 2-6 X-ray fluorescence maps of the Mannville glauconitic sandstones.

Ca is plotted in red, Fe is plotted in green, and K is plotted in blue. Ca-rich sections most likely represent a Ca component in a carbonate mineral such as dolomite; Fe-rich sections most likely represent siderite; and K-rich sections most likely represent glauconite. Black sections of the samples contain no measurable Ca, Fe, or K, and are therefore most likely quartz. The locations of individual XANES spot analyses (Figure 2-7) are labeled with numbers, and the locations of XANES maps (Figure 2-8) are outlined. The outline in a) is the outline of the XANES map plotted in b. a-e are from sample 2053.61 m, and e is from sample 2055.02 m (data provided in supplementary material).

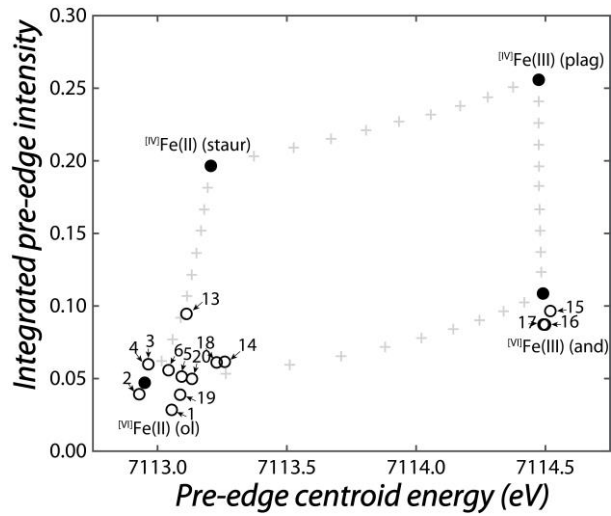


Figure 2-7 Processed XANES spot analyses illustrating the range of Fe oxidation states in the examined samples.

The corners of the variogram represent analyses of well-characterized standards (staur = staurolite; ol = olivine; and = andradite; and plag = plagioclase), while the '+' symbols represent analyses of the average spectra at 10% intervals between the standards. Numbered labels correspond to spots plotted in Figure 2-6 (data provided in supplementary material).

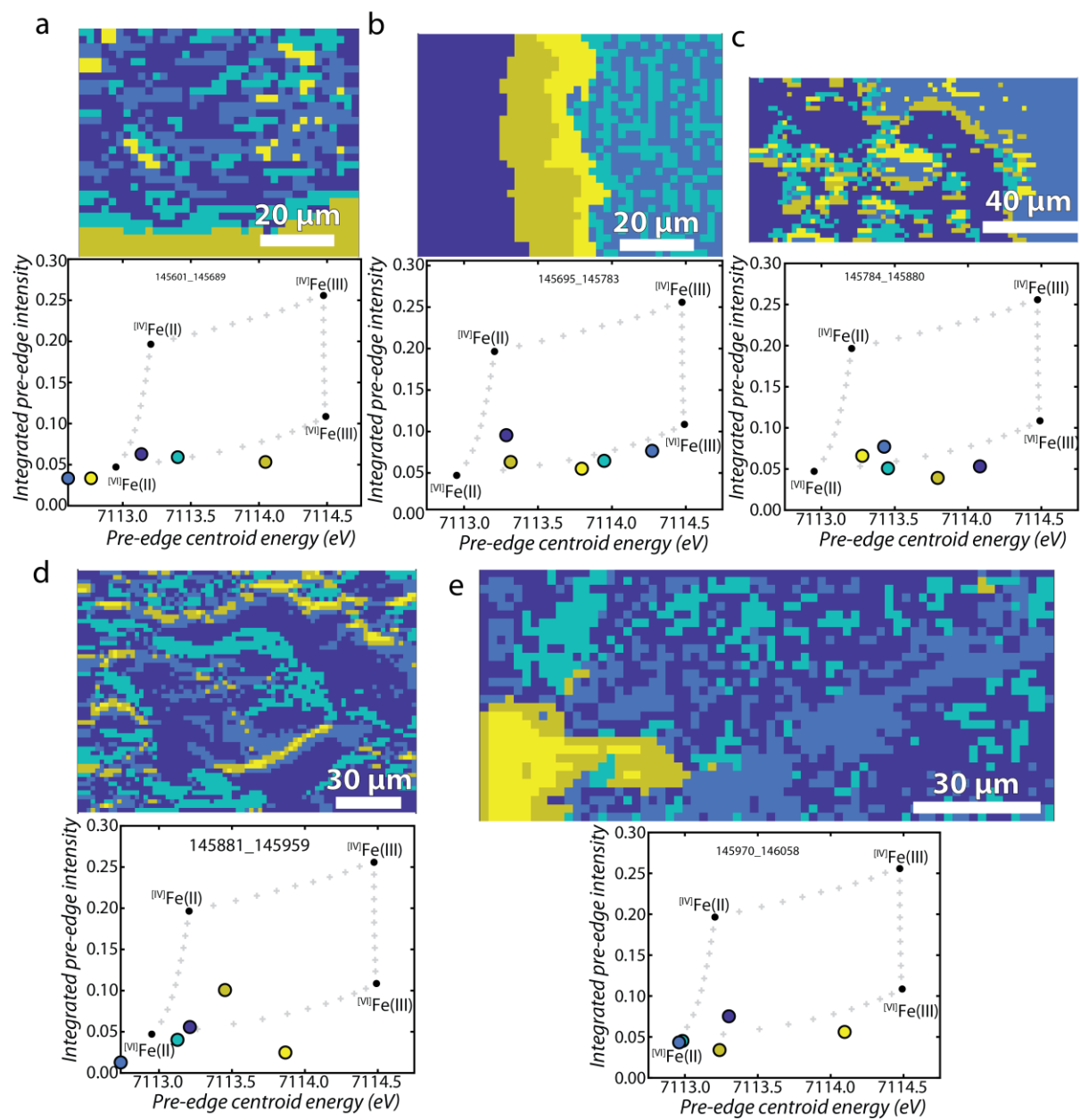


Figure 2-8 Cluster analyses of XANES maps and accompanying plots of the pre-edge characteristics of the derived spectra.

Maps a-e are outlined in Figure 2-6. The colors in each map correspond to the colors of the dots in the variogram below (data provided in supplementary material).

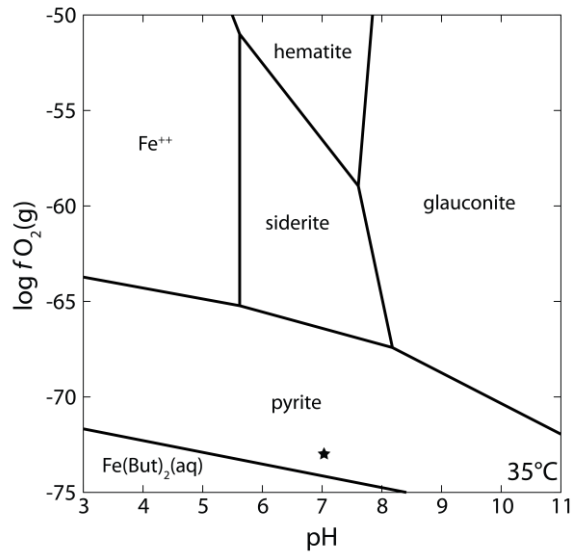


Figure 2-9 Activity diagram illustrating the stability fields of iron minerals in Mannville Group.

The diagram assumes 1 μmol Fe and S, 1 mmolal K and Mg, 100 mmolal NaCl, and 1 molal C. $a_{\text{SiO}_2(\text{aq})}$ is set by equilibrium with respect to chalcedony, $a_{\text{Al}^{+++}}$ is set by equilibrium with respect to kaolinite, and $a_{\text{Ca}^{++}}$ is set by equilibrium with respect to dolomite. The abbreviation a indicates the activity of the subscripted species or component. The star represents approximate conditions of the Mannville pore fluids (see 2.2.4).

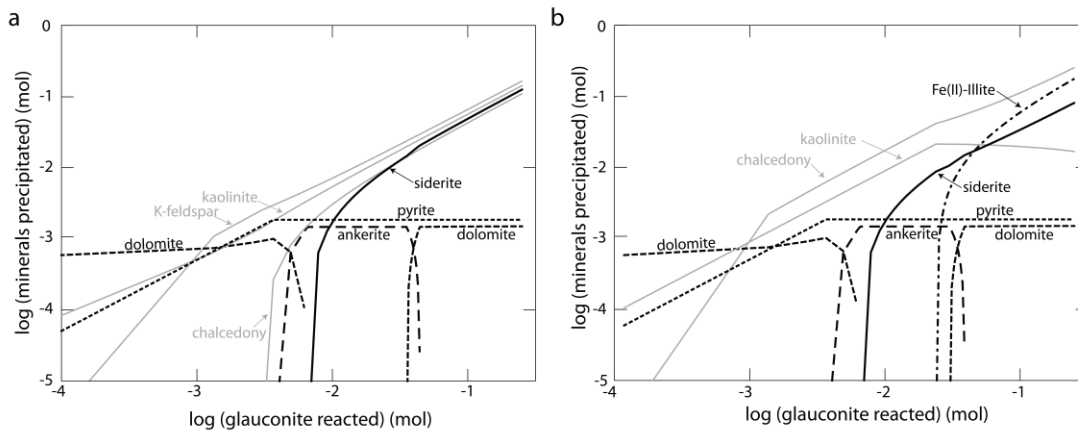


Figure 2-10 Calculated results of thermodynamic modeling.

a) A reaction path calculated by numerically reacting the Mannville glauconite with Mannville pore fluids.

b) Same as a, but assuming that the precipitation of K-feldspar is kinetically limited.

2.4 Discussion

2.4.1 *Summary and Interpretation of Petrographic and Geochemical Observations*

2.4.1.1 *Glauconite, Ankerite, and Pyrite*

The EPMA analyses on glauconite pellets show consistency in compositions of the essential cations except Fe and Al (Table 2-4). It is likely that the high Al content is related to the evolved state of the glauconite (Ruffell et al., 1999; Pestitschek et al., 2012), and the co-variation in Al and Fe (Figure 2-5) could be related to a combination of different parent materials, heterogeneous degrees of dissolution (loss of Fe), and/or slight variation in fluid chemistry at the time of formation. Together, our petrographic study and chemical analyses, particularly the consistent 7-8 wt.% of K₂O and high overall Al content (>20%) in EPMA analyses (Table 2-4), suggest that the examined glauconite grains are in the “evolved” stage. Evolved stage glauconite is generally interpreted to reflect extended residence time at the seafloor prior to burial (Odin and Matter, 1981), and successive structure-obliterating recrystallizations (Odin, 1988). However, our observations show that post-depositional carbonation plays an important role in the alteration of glauconite (Sect. 2.3.4).

The ankerite concretions observed in our samples likely formed during the early stages of diagenesis. Indeed, the homogeneous texture (absence of center-to-edge variations as a result of separate growth stages) (Figure 2-4a) indicates pervasive growth, where individual cement crystals nucleated and grew simultaneously throughout the concretion volume and resulted in a relatively uniform internal texture and little to no radius increase with time (Curtis and Coleman, 1986; Raiswell, 1987; Mozley, 1996; Raiswell and Fisher, 2000). This type of concretion most likely formed prior to significant mechanical compaction of the sediments (e.g., Bojanowski and Clarkson, 2012). The clastic quartz and glauconite grains are far apart and appear to be “floating” in the concretion, this also suggests that the concretion formed before major sediment compaction (Marshall and Pirrie, 2013). Nonetheless, it is difficult to unambiguously determine

whether glauconite dissolution or ferruginous pore waters provided the Fe^{++} required for concretion formation, because the glauconite grains might have been completely dissolved prior to concretion formation. Thus, although concretion formation during the early stages of diagenesis could represent a net sink of inorganic C over geologic timescales, we focus our subsequent discussion and interpretation of our modeling results on the formation of siderite at the expense of glauconite.

Both framboidal and euhedral pyrites were identified in our samples (Figure 2-1 and Appendix A-S7), which, together, suggest that chemical diagenesis in the Mannville sediments was dominated by reducing pore fluids that varied in Fe and S contents over time. The observed framboidal pyrites likely formed during initial, rapid growth accompanying SO_4^{2-} reduction after pore waters were occluded from the overlying sea water, while the observed euhedral pyrite likely formed slowly, after much of the initial SO_4^{2-} load had been diminished (Raiswell, 1982). Euhedral pyrite is found exclusively in the composite glauconite grain, suggesting its formation prior to glauconitization (and thus prior to dissolution and carbonation of glauconite); the framboidal pyrite in the siderite cement is authigenic, indicating elevated Fe and S concentrations. Ultimately, the limited total sulfide in the bulk rock analyses (Table 2-6) suggests that pyrite is not a dominant Fe-bearing mineral in the Mannville sediments.

2.4.1.2 Glauconite Diagenesis and the Formation of Siderite

Based on their contact faces with glauconite and their crystal structure (Figure 2-3b), we interpret the observed siderite crystals as a product of glauconite dissolution. Siderite microcrystals in the Mannville glauconitic sandstones nucleated predominantly along framework grain boundaries which exhibit dissolution textures, as well as along ruptures in individual grains (Figure 2-3). The inter- and intra-granular space allows carbonate-rich fluid to interact with the glauconite and thus

promotes carbonation. The microcrystalline siderite grains show evident rhombohedral habit and no sign of physical abrasion (Figure 2-3b) which suggests they were formed *in situ* as a result of glauconite dissolution.

The fact that these glauconite-adjacent carbonates are Ca-poor siderite (Table 2-5), rather than the ankerite that characterizes the early-formed concretions, suggests limited availability of Ca during the later glauconite carbonation reaction. This is consistent with the lack of Ca-bearing silicates in the rocks and the apparent overall stability of dolomite (the only other potential mineralogical Ca source) during diagenesis of the Mannville rocks. In turn, the observation that glauconite-adjacent siderites almost exclusively contain silicate-derived cations in the form of Fe⁺⁺ suggests that glauconite carbonation is a net CO₂ sink during diagenesis of greensands sediments.

The conversion of glauconite, where Fe is dominantly oxidized, to siderite, where it is exclusively reduced (Figure 2-7) requires Fe mobilization through a reduction reaction. The XANES maps (Figure 2-8), which indicate gradients in Fe redox state over the scale of micrometers, strongly suggest that the Fe reduction occurs in close proximity to the glauconite surface, or even potentially while Fe is still in the glauconite structure. Moreover, the gradients in Fe concentrations (Figure 2-2, Figure 2-3 and Figure 2-6) and the overall variability of Fe concentrations in the EPMA analyses (Table 2-4) suggest that the Fe is indeed mobile during glauconite diagenesis. On its face, these lines of evidence suggest that glauconite carbonation is a reduction facilitated, coupled dissolution-reprecipitation reaction (cf. Putnis, 2009). However, the behavior of the significant elements in the Mannville glauconite other than Fe (i.e., K, Mg, Al, and Si) suggest the interfacial mechanism of this reaction involves not only glauconite dissolution and siderite precipitation, but also the re-precipitation of Al-enriched glauconite. Indeed, stoichiometric dissolution of glauconite *should* liberate considerable amounts of Mg, Al, Si, and K in addition to Fe (Eq. 2-1 and Eq.2-2). Interestingly, however, the examined samples show

limited, if any, evidence of K or Mg mobility. For example, EPMA analyses all yield highly consistent concentrations of both elements in all glauconite analyses (Table 2-4), and EDS maps show homogeneous distribution of these elements across grains (Figure 2-2 and Figure 2-3). A portion of the Al and Si were evidently sequestered as kaolinite (Figure 2-1c), but we observed comparatively little kaolinite in our samples when compared to the abundance of Fe-bearing carbonates. Plotting Al_2O_3 and FeO from the individual glauconite EPMA analyses yields interesting evidence in support of the reprecipitation of Al-enriched glauconite upon reduction-facilitated dissolution of the primary Mannville glauconite (Figure 2-5). The concentrations of these oxides are strongly ($r^2=0.87$) anti-correlated, suggesting that Fe^{+++} exiting the glauconite structure is accompanied by a commensurate enrichment in Al^{+++} . As discussed in Sect. 2.1.1, the chemistry of glauconite can vary greatly depending on the mineral's "maturity". Currently, the widely accepted glauconite alteration mechanism is by recrystallization in a confinement, where partial chemical isolation from seawater or pore fluids within various substrates is maintained (Odin and Matter, 1981). However, it is difficult to explain how the confinement forms in the subsurface and why recrystallization in such confinement always results in K enrichment as glauconite evolves. López-Quirós et al. (2020) suggested the reduction of Fe(III) to Fe(II) in the structure of glauconite leads to a gradually higher charge deficiency, which may be stabilized by increased K uptake into the mineral, such that Fe reduction is a driving force for the enrichment of K. This mechanism also accounts for the lack of significant losses of other elements as glauconite matures. In addition, our study showed that when carbonation of Fe in a reducing, CO_2 -rich fluid consumes the mobile Fe(II), glauconite becomes thermodynamically unstable, and the K enrichment reaction observed by López-Quirós et al. (2020) may be reinforced. Therefore, post-burial carbonation reactions are likely a major, yet often overlooked, alteration mechanism of glauconite (cf. Odin and Matter, 1981).

The glauconite grains are partially replaced by euhedral dolomite crystals (Figure 2-2a and Figure 2-3c), as indicated by the rhombic impressions in the glauconite grains suggesting the growth of the dolomite crystals succeed the glauconite. The dolomite grains that have replaced glauconite may have formed due to recrystallization of the primary dolomite followed by pressure solution of glauconite (e.g., Rutter, 1983). Some Fe substitution during such processes likely caused the Fe-rich rims in some of the dolomite grains (Figure 2-2b). Carbonate minerals formed this way cannot be entirely accounted towards quantifying the CO₂ sequestration potentials as some of the carbonate consumed in these reactions was released by the primary dolomite.

2.4.1.3 Reaction Path Modeling of Glauconite Carbonation

Our initial thermodynamic modeling results (Figure 2-10a) suggest that, upon reaction with Mannville formation pore fluids, the Mannville glauconite should form abundant siderite, chalcedony, kaolinite, and K-feldspar, along with small amounts of pyrite, ankerite, and dolomite. The small amounts of dolomite formation predicted by the reaction path model are consistent with our petrographic observations of overgrowths on dolomite (Figure 2-2a,b). Although we do observe siderite, pyrite, kaolinite, and silica in our samples, we did not find any evidence of diagenetic K-feldspar formation. Since K-feldspar is predicted to be the most abundant, thermodynamically favorable mineral formed during the diagenesis of Mannville rocks, the K, Al, Si released from glauconite dissolution must be finding another sink. As discussed above, textural and geochemical evidence suggest that the reduction-facilitated, coupled glauconite carbonation reaction was not ultimately accompanied by significant Mg or K mobility, and only modest amounts of Al and Si transfer. Thus, the K-feldspar predicted to precipitate in our model is likely to have actually precipitated as an Al-enriched glauconite, which would be consistent with the observations of anticorrelated Al and Fe contents in EPMA analyses (Figure 2-5). To explore this possibility, we suppressed the precipitation of K-feldspar in the simulation presented in Figure

2-10b. Importantly, in this second simulation, Fe(II)-illite (which is equivalent to a recrystallized glauconite) is precipitated in lieu of K-feldspar while the precipitation of siderite remains almost completely identical to the simulation in which K-feldspar precipitated. This result suggests that the conceptual model for glauconite recrystallization is valid, and thus it is likely an important glauconite alteration process.

2.4.2 Implications for CO₂ Mineralization in Glauconite-rich Sediments

Overall, our observations demonstrate that glauconite-bearing sedimentary reservoirs are poised to mineralize CO₂. Although redox conditions of most hydrocarbon reservoirs are buffered by organic-inorganic carbon reactions (e.g., Helgeson et al., 1993; Cody and Hutcheon, 1994) at conditions that are likely too reducing to favor siderite precipitation following CO₂-induced glauconite dissolution (Figure 2-9), the generally limited amounts of S in reservoir fluids suggests that these conditions are unlikely to persist much past the initial stages of water-rock-CO₂ interaction. In addition, the injection of oxidized C in the form of CO₂ will tend to raise the reservoir fluid redox state above the inorganic-organic carbon buffer and thereby promote siderite formation.

The new insight into the process of reduction-facilitated glauconite recrystallization and siderite precipitation offers essential insights into the potential of GCS in glauconite-rich sediments. Indeed, these observations demonstrate that CO₂ mineralization in these rocks does not require complete glauconite dissolution as a first step, and thus that the sediment structure may stay mostly intact during carbonation reactions. Reductants in the reacting fluids are vital for glauconite conversion to siderite; these can be supplied in the form of reduced carbon in many hydrocarbon reservoirs worldwide, including the Mannville formation. Glauconite-rich sediments are often associated with carbonates such as ankerite and dolomite, and the presence of these

carbonates may facilitate the formation of siderite by lowering the barrier for its nucleation (Lasaga, 2014).

Glaucosite varies widely in its cation content, and assessing the development stage of glaucosite is critical in assessment of CO₂ mineralization potentials for a given glaucosite-bearing reservoir. In general, less evolved glaucosite contains more divalent cations and therefore should be more prone to mineralizing CO₂. We have demonstrated, using a combination of petrographic investigation, geochemical observations, and geochemical models, that the evolved glaucosite of the Mannville formation is capable of mineralizing significant amount of CO₂. This, in turn, suggests that glaucosite-bearing sandstones worldwide should be focus targets for injection of anthropogenic CO₂. Nevertheless, there are numerous complexities, including, for example, the potential of organic-metal complexing to promote and/or hinder mineralization reactions (e.g., Escario et al., 2020) that will require further evaluation as the potential for engineered carbon sequestration in these systems gains momentum.

2.5 Conclusions

Mineralization of CO₂ in glaucositic sandstones integrates a complex series of reactions, most importantly the reductive dissolution of glaucosite. We have applied an array of techniques to demonstrate that glaucosite carbonation in the Mannville Group is a reduction-facilitated, coupled glaucosite recrystallization and siderite precipitation reaction. Our geochemical modeling results illustrate that, although K-feldspar is favored to precipitate during reductive glaucosite dissolution, precipitation of this mineral is likely kinetically limited, and that an Fe-impoverished, Al-enriched glaucosite is likely precipitating instead. This observation is consistent with our microanalyses of glaucosite grains, which show that Fe and Al contents of glaucosite grains are inversely correlated. Our XANES analyses show that the Fe is reduced while still in the glaucosite structure, which provides us with new insights on glaucosite alteration mechanisms.

In addition to the mineral assemblage and the availability of CO₂, the overall redox state of the reacting fluid ultimately controls the conversion of glauconite into siderite, and fluids in hydrocarbon reservoirs worldwide are poised to promote Fe reduction during CO₂-glauconite-brine interaction. Initially, this Fe may precipitate as pyrite, but, once the initially limited supply of S is exhausted, Fe will be precipitated as siderite. We conclude that the carbonation reactions constitute an important alteration process of glauconite, and the potential for glauconite carbonation as an engineered GCS mechanism is likely immense.

Acknowledgements. The authors express their gratitude to the research and funding agencies who made this study possible: the Alberta Energy Regulator Core Research Centre, the Canada First Research Excellence Fund and NSERC Discovery Grant RGPIN-2018-03800. We would like to thank Christopher Debuhr and Robert Marr (University of Calgary) for performing the SEM and EPMA analyses, respectively. We would also like to thank Konstantin Ignatyev (Diamond Light Source) and Clancy Zhijian Jiang (Cambridge University) for assistance with XANES Analyses. Finally, we thank two anonymous reviewers for their thorough reading of this manuscript, which helped to improve it significantly.

3 Chapter 3 Kinetics of glauconite dissolution under anaerobic conditions as a function of pH and temperature

Abstract

Because it is an abundant, divalent cation-bearing mineral in sedimentary rocks and hydrocarbon reservoirs worldwide, glauconite has likely played a role in Earth's carbon cycle over geologic time and may be important for ongoing efforts to geologically store anthropogenic CO₂. Yet, due to glauconite's complicated chemistry and redox sensitivity, its dissolution kinetics have so far been difficult to constrain. To fill this significant knowledge gap, we have undertaken a study to quantify the far-from-equilibrium rates of glauconite dissolution using a novel experimental apparatus specifically designed to explore mineral dissolution kinetics under strictly anaerobic conditions. Steady-state glauconite dissolution rates were measured at varying pH from 1.7 to 11.2 and temperature from 24 to 80 °C. Temporal evolution of the differences between cation concentrations in the inlet and outlet solutions exhibit stoichiometric or close-to-stoichiometric glauconite dissolution for Fe, Mg, and Si. Fitting the experimental data to a standard Transition State Theory-derived, far-from-equilibrium rate law yields:

$$k = 2.21 \times 10^{-12} \cdot \exp \left[\left(\frac{-32.5}{R} \right) \cdot \left(\frac{1}{T} - \frac{1}{T_r} \right) \right] \cdot a_{H^+}^{0.37} + 2.97 \times 10^{-14} \cdot \exp \left[\left(\frac{-37.7}{R} \right) \cdot \left(\frac{1}{T} - \frac{1}{T_r} \right) \right],$$

where k is the rate constant (mol m⁻²s⁻¹) at the temperature (T , Kelvin) and H⁺ activity (a_{H^+}) of interest, T_r is the reference temperature (298.15 K), and R is the ideal gas constant (8.314 x 10⁻³ kJ mol⁻¹ K⁻¹). Our experimental results show that the mechanism of glauconite dissolution is highly dependent on temperature and on pH in acidic solutions. Geochemical calculations based on the fitted rate equation predict that complete carbonation of glauconite in a system with a 10:1 water-rock ratio and 50 bar of CO₂ fugacity can be expected after 17.5, 11.9, 7.1, and 3.8 kyr at 35°C, 45°C, 60°C and 80°C, respectively. While the lower-temperature simulations generally agree with previously published modelling efforts, the higher temperature reactions are significantly faster than previously predicted. These results highlight the importance of reservoir

temperature for glauconite diagenesis and suggest that, when appropriate attention is paid to reservoir temperature during site selection, glauconite carbonation may present significant opportunities for CO₂ mineralization.

3.1 Introduction

3.1.1 *Glauconite and the global Fe and C cycles*

Glauconite is an authigenic clay mineral that occurs mostly on continental shelves. It is widely distributed on present-day shelves from 50 °S to 65 °N at water depths between 50 and 500 m, particularly on the upper slope and outer shelf between 200 and 300 m (Odin and Matter, 1981). Due to its common occurrence throughout the geologic record, glauconite is commonly used to interpret paleoenvironmental conditions. Specifically, glauconite provides a mineralogical record of the long-term sequestration of elements such as K and Fe during marine diagenesis (Baldermann et al., 2022, 2015; López-Quirós et al., 2019) and the potential role of reverse weathering reactions in Earth's long-term carbon cycle (Isson and Planavsky, 2018; Ma et al., 2022). It is additionally a sensitive proxy of low sedimentation rates in the marine realm (e.g., Triplehorn, 1967; Ireland *et al.*, 1983; Odin, 1988; Huggett and Gale, 1997; Eder *et al.*, 2007; Harding *et al.*, 2014; López-Quirós *et al.*, 2019; Bansal *et al.*, 2020). Glauconite's chemistry and abundance therefore constitute a powerful tool for sedimentological and stratigraphic interpretations, especially when it occurs in conjunction with well-defined trends of sea-level changes (Bansal et al., 2020; Eder et al., 2007). However, some of the paleoenvironmental implications remain open to debate, in part, due to the lack of geochemical constraints on the mechanisms of glauconite alteration during sediment burial (Eder et al., 2007; Harding et al., 2014).

Glauconite has also been identified as an important cation provider for carbon mineralization in sedimentary basin-based geologic carbon storage (GCS) (Zhang and Tutolo, 2022). Yet, in spite

of its recognized importance for GCS, the rates of glauconite dissolution and the coupled conversion to carbonates (e.g., siderite and/or ferroan dolomite) have not been quantitatively determined (Zhang and Tutolo, 2021). In order to simulate the geochemical evolution of glauconitic sediments as they interact with CO₂-rich fluids, and to evaluate the feasibilities and limitations for sequestering CO₂ through glauconite carbonation reactions, it is critical to constrain glauconite dissolution rates, and most importantly, the rates of divalent cations released from glauconite structure.

3.1.2 *Measurements and estimates of glauconite dissolution rates*

Although recent efforts have sought to provide an up-to-date database of mineral dissolution rate parameters (Heřmanská et al., 2022), the most comprehensive and widely accepted database of these parameters is that of Palandri and Kharaka (2004). This database includes dissolution rates of glauconite, which were derived from the data compilation by Sverdrup (1990), which, in turn, was collected from Cloos *et al.* (1961). Depending on glauconite dissolution mechanisms at different temperature and pH conditions, these parameters may or may not produce useful predictions of glauconite dissolution rates. Specifically, because the original source, Cloos *et al.* (1961), conducted their dissolution experiments in solutions with very acidic pH (1.97-2.06 M HCl) and at high temperatures (40-650 °C), extrapolations to conditions relevant for sediment burial and/or GCS are highly uncertain. In other studies, for example, Xu *et al.* (2004), kinetic parameters for illite dissolution from Palandri and Kharaka (2004) were used for glauconite dissolution in their numerical model. Given the small amount (4.4%) of glauconite in the considered reservoir and a lack of other quantitative constraints, this assumption had negligible effect on the overall outcome of the simulations. Yet, in rocks where glauconite is more

abundant, it would likely lead to significant uncertainties, which may, in turn, propagate into even more significant uncertainties in predictions of carbonate mineral formation during GCS. Apart from these various, though limited, efforts at parameterizing glauconite dissolution rates, another line of research has also been used to explore glauconite dissolution kinetics in the context of its potential application as a potash (K) source for soil fertilization. Due to their focus, these studies typically only determine K release rates (e.g., Pratap *et al.*, 2020). These rates are, unfortunately, neither directly applicable to GCS applications nor generally relevant for paleoenvironmental extrapolations, because potash recovery often requires a roast-leaching method that heats the glauconite to 100-900 °C (much higher than typical reservoir temperatures, 30–80 °C), and heating glauconite in an uncontrolled atmosphere inevitably causes Fe oxidation (Pratap *et al.*, 2020; Rudmin *et al.*, 2019, 2018; Shekhar *et al.*, 2017; Yadav *et al.*, 2000). Because the redox state of structural Fe plays an important role in determining the fixation or release of structural K (e.g., Chen *et al.*, 1987; Huang, 2005; Sparks and Huang, 2015; Florence *et al.*, 2017), the successful assessment of glauconite kinetics in laboratory studies requires controlled redox conditions.

To better understand (paleo)environmental changes and accelerate industrial exploration and implementation of GCS in glauconite-rich sedimentary reservoirs, it is critical to constrain the kinetics of glauconite dissolution over the wide pH and temperature range necessary for rate calculations at relevant reservoir conditions. Here, we present glauconite dissolution rate data obtained under strictly anaerobic conditions and derive a kinetic rate equation for glauconite dissolution. The results show that glauconite dissolves incongruently under the considered experimental conditions. Glauconite dissolution rates are temperature dependent, and pH dependent in acidic solutions. Geochemical calculations using the derived rates indicate increasing glauconite carbonation rates with increasing temperature, implying that, if reducing

conditions are maintained, diagenetic and engineered CO₂ mineralization in elevated temperature glauconitic sandstone reservoirs may facilitate its rapid and permanent storage.

3.2 Methods

3.2.1 Mineral Preparation

Two types of glauconite, henceforth labeled Type I and Type II, were used in this study. Type I glauconite was obtained from Franconian Stage sandstone cores of the Tunnel City Group in the subsurface of Minnesota, USA (at about 212.14 m depth in Minnesota Unique Well Number 185810). These samples were chosen due to the well-preserved glauconite pellets as well as the detailed chemical characterization from a previous study, including the chemical composition as well as the Fe(II)/Fe(III) ratio (Tutolo et al., 2020). According to this previous work, a composition of $\text{Na}_{0.212}\text{Ca}_{0.0359}\text{K}_{0.679}\text{Fe(III)}_{1.175}\text{Mg}_{0.337}\text{Fe(II)}_{0.079}\text{Al}_{0.688}\text{Si}_{3.654}\text{O}_{10}(\text{OH})_2$ was calculated for Type I glauconite. Type I glauconite pellets were hand-picked from the core samples using a pair of anti-static stainless-steel tweezers. Type II glauconite used in this study was geostandard GL-O obtained from Centre de Recherches Pétrographique et Géochimiques Service d'Analyse des Roches et des Minéraux (SARM). The elemental composition of the glauconite given by SARM resulted in a composition of $\text{Na}_{0.01}\text{Ca}_{0.08}\text{K}_{0.75}\text{Fe(III)}_{0.95}\text{Mg}_{0.49}\text{Fe(II)}_{0.14}\text{Al}_{0.66}\text{Si}_{3.754}\text{O}_{10}(\text{OH})_2$. The mineral received was clean glauconite pellets with diameters of 100-350 μm.

Prior to experiments, both types of glauconite pellets were briefly treated with 0.1 M HCl to remove any carbonate cements. The cleaned and dried glauconite pellets were then mechanically crushed with an agate mortar and pestle under acetone to prevent oxidation. The crushed glauconite was then sieved to collect the 20–63 μm size fraction. This size fraction was transferred to the Coy anaerobic chamber (described below) and rinsed with ultrapure (18 MΩ-cm) deionized (DI) water to remove the residual acetone and ultrafine particles attached to

mineral surfaces. The glauconite was also imaged using an FEI Quanta 250 Field Emission Gun-Scanning Electron Microscope (SEM), which confirmed the purity of, and lack of contaminant phases in, the starting material (Figure 3-1). The specific surface areas of the crushed and cleaned glauconite used in the experiments are $41.55 \pm 0.13 \text{ m}^2/\text{g}$ (Type I), and $54.52 \pm 0.16 \text{ m}^2/\text{g}$ (Type II), as measured by N_2 adsorption with the Brunauer-Emmett-Teller (BET) method (Brunauer et al., 1938) at the University of Calgary. Upon completion of the experiments, reacted glauconite was collected on $0.22 \text{ }\mu\text{m}$ PVDF membranes via vacuum filtration. The filtered minerals were rinsed using DI water and then dried at 60°C in the Coy anaerobic chamber. Using the BET method, both types of glauconite showed $\sim 20\%$ increase in post-experimental surface areas, $55.33 \pm 0.14 \text{ m}^2/\text{g}$ (Type I), and $65.50 \pm 0.16 \text{ m}^2/\text{g}$ (Type II). Post-experimental glauconite was analyzed with a Thermo Scientific Phenom™ tabletop Scanning Electron Microscope (SEM) coupled with an Energy Dispersive Spectroscopy (EDS) detector to identify mineral reprecipitation or secondary precipitation. The major benefit of SEM-EDS to our study is that it can locate the very small amount of secondary precipitation *in situ*, which is often undetectable via bulk mineralogical methods (e.g., XRD) (Metz et al., 2005). However, because EDS is a semi-quantitative analytical method, the acquired spectra were only used to investigate the congruency of glauconite dissolution and not directly applied to any quantitative chemical calculations.

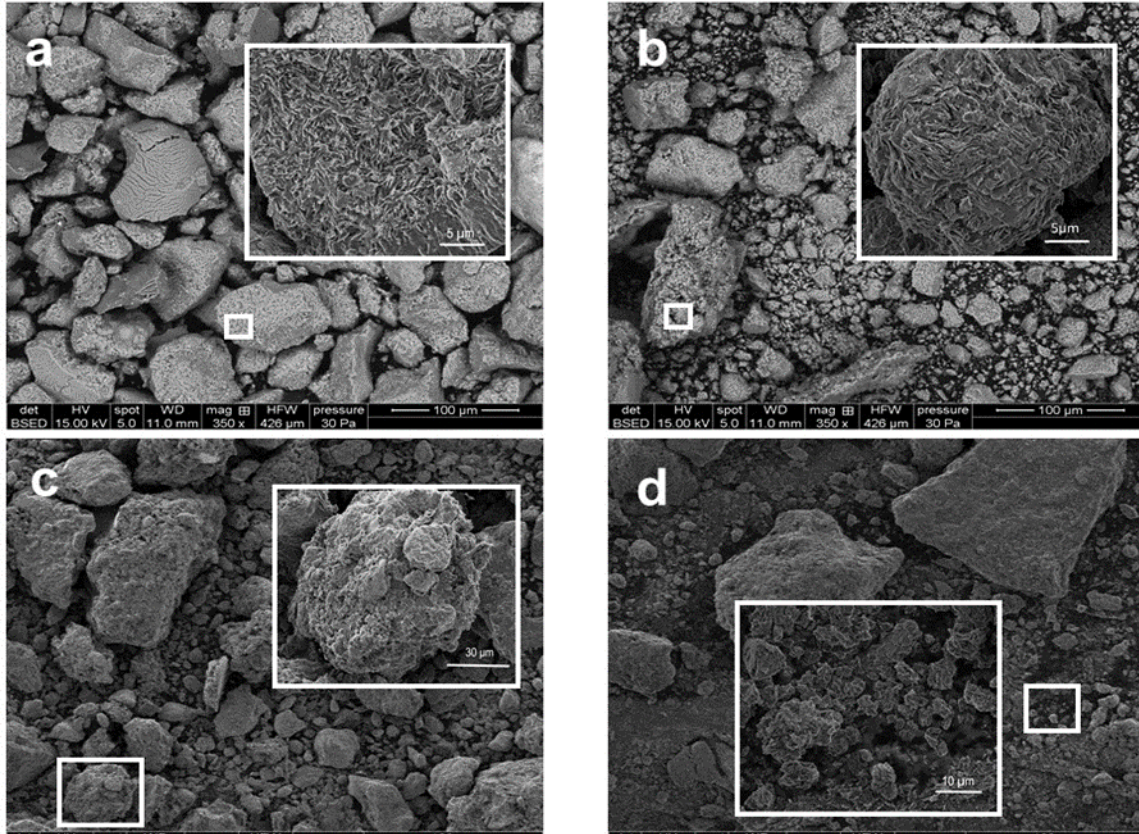


Figure 3-1 Scanning electron microscopy (SEM) images of pre-experimental glauconite grains Type I (a) and Type II (b), and post-experimental glauconite Type I (c) and Type II (d).

Pre-experimental glauconites were treated as described in Sect. 3.3.2.1. Both types of glauconite showed flaky/rosette-shaped internal microstructure (a, b). Dissolved glauconite after a series of dissolution experiments (c, d) showed that the microstructure was mostly maintained for both types of glauconite, but the grain sizes decreased dramatically. A slight increase in surface rugosity was also observed.

3.2.2 Experimental Setup

3.2.2.1 Redox Considerations

Previous research demonstrated that the redox state of the reacting fluid is the most important parameter governing the thermodynamics of glauconite conversion to siderite (Tutolo et al., 2020). Oxidizing conditions lead to at least partial oxidation of Fe in glauconite (Kisiel et al., 2018), which obfuscates the investigation of Fe release rates from the mineral structure. Because the

redox states of structural Fe play an important role in determining the fixation or release of structural K (Chen et al., 1987; Florence et al., 2017; Huang, 2005; Sparks and Huang, 2015), a controlled redox environment helps to constrain K behavior in relevant geological settings. Reducing environments are prevalent in glauconite-rich sedimentary formations suitable for GCS, which means rates measured in such environments can be directly used to evaluate diagenesis and CO₂ mineralization in sedimentary reservoirs (Zhang and Tutolo, 2021). Therefore, steps were taken to maintain a reducing environment for all the flow-through experiments.

The inlet solutions were prepared with 18 MΩ deionized water, which was first sparged with N₂ for at least 2 hours to remove dissolved O₂ (Butler et al., 1994), and then transferred to a Coy anaerobic chamber with an anoxic atmosphere (~97.5% N₂, ~2.5% H₂, and <1 ppm O₂) maintained by Pd catalysts and circulating fans. The N₂-sparged deionized water was stirred for at least 12 hours in an open container in the Coy anaerobic chamber to remove any residual O₂ and to create a slightly reducing headspace in the container. The inlet solutions were prepared in 4 L, acid-washed Low-Density Polyethylene (LDPE) collapsible bladders and sealed in the Coy anaerobic chamber. The inlet solutions were either never or only briefly (< 1 min) in contact with the lab atmosphere while being connected to the flow-through apparatus (Figure 3-2).

3.2.2.2 *Flow-through Apparatus*

All dissolution experiments were conducted in mixed-flow reactors. Lower temperature experiments (24, 40, and 60 °C) were performed in Savillex Purillex® PFA vessels (120 mL) with 10 μm outlet filters and floating Teflon supported magnetic stir bars. High temperature (80°C) experiments were mainly conducted in a 100 mL Parr Model 4590 reactor with a suspended stirrer and a 10 μm outlet filter. The 10 μm outlet filters ensured minimal mineral loss during the flow-through experiments, because the initial grain size was at least 20 μm (Sect. 3.2.1). We

therefore assumed the masses of the reacting glauconite within the reactor stayed constant throughout the experiment. Inlet solutions (Table 3-1) were prepared following Saldi *et al.* (2007), using DI water and American Chemical Society (ACS) reagent-grade chemicals including HCl, NaOH, NaCl, NH₄Cl, NH₄OH, KH₂PO₄, and MgCl₂. All inlet fluids had stoichiometric ionic strengths of 0.02 mol/kg. Fluid was injected into the reactors using either Watson Marlow 120S pumps (for PFA reactors) or Teledyne SSI LD-class pumps (for the Parr reactor), which maintained constant fluid flow rates of 3×10^{-7} - 1×10^{-6} kg s⁻¹ and resulted in residence times of ~2.5 days. Steady-state dissolution rates, as indicated by stabilized outlet Fe, Mg, and Si concentrations within analytical uncertainty, were obtained after an elapsed time ranging from 10 to 20 days. Over the course of the experiments, outlet solutions were collected in N₂-purged, sealed LDPE bottles to prevent fluid evaporation and oxidation of Fe. The accumulated masses of the outlet fluid over time intervals were used to calculate flow rates. In this way, the flow rates we report account for systematic errors produced by the pumps over time. The standard deviations of flow rates over the course of individual experiments were used in analytical error propagation calculations.

All of the 24 and 60 °C flow-through experiments were conducted in the Coy anaerobic chamber described in Sect. 3.2.2.1 (Figure 3-2b). The 24°C experiments were placed directly in the anaerobic chamber at room temperature (24 ± 1 °C), and the 60°C experiments were heated by a 2mag Stirring Drybath set at a temperature of 60 ± 0.5 °C. Due to the limited space in the Coy anaerobic chamber, most of the 80°C experiments were conducted externally in the Parr reaction vessel described above. All 40°C experiments were designed as illustrated in Figure 3-2a. To evaluate the possibility of redox condition changes (e.g., oxygen diffusion into the inlet solutions during experiments) in the water bath apparatus and the Parr reactor, we repeated certain experiments (Exps. #B-1, #47-1, #31-1, #34-1, and #36-1 are duplicates of #B, #47, #31, #34, and #36, respectively) using the same minerals and inlet solutions with different experimental setups. These duplicates also permit quantification of the standard deviations of the determined rates.

Expts. # 45, 47, 47-1, and 48 were used to test the effectiveness of the water bath apparatus at higher temperature, so we kept the reacting glauconite in the same reactor throughout these experiments and only changed solutions and experimental locations.

Table 3-1 Compositions (g/kg) of inlet solutions used for the glauconite dissolution experiments (modified after Saldi *et al.* (2007)).

pH (25 °C)	1 M HCl	NaCl(s)	KH₂PO₄(s)	NH₄Cl(s)	28% NH₃	1 M NaOH(l)
1.7	19.9525	0.0025	-	-	-	-
2	10	0.5844	-	-	-	-
2.3	5.0125	0.875	-	-	-	-
2.7	1.995	1.0525	-	-	-	-
3.3	0.5	1.1375	-	-	-	-
4	0.1	1.1688	-	-	-	-
4.3	0.05	1.165	-	-	-	-
5.5	-	1.165	-	-	-	-
6.5	-	-	6.805	-	-	17.35
7.5	-	-	-	1.0538	0.0182	-
8.03	-	-	-	1.0201	0.0566	-
8.55	-	-	-	0.9115	0.18	-
9.25	-	-	-	0.855	-	6.665
9.7	5.65	-	-	-	1.29	-
10	-	-	-	0.1654	1.0282	-
12	5.575	-	-	-	-	10

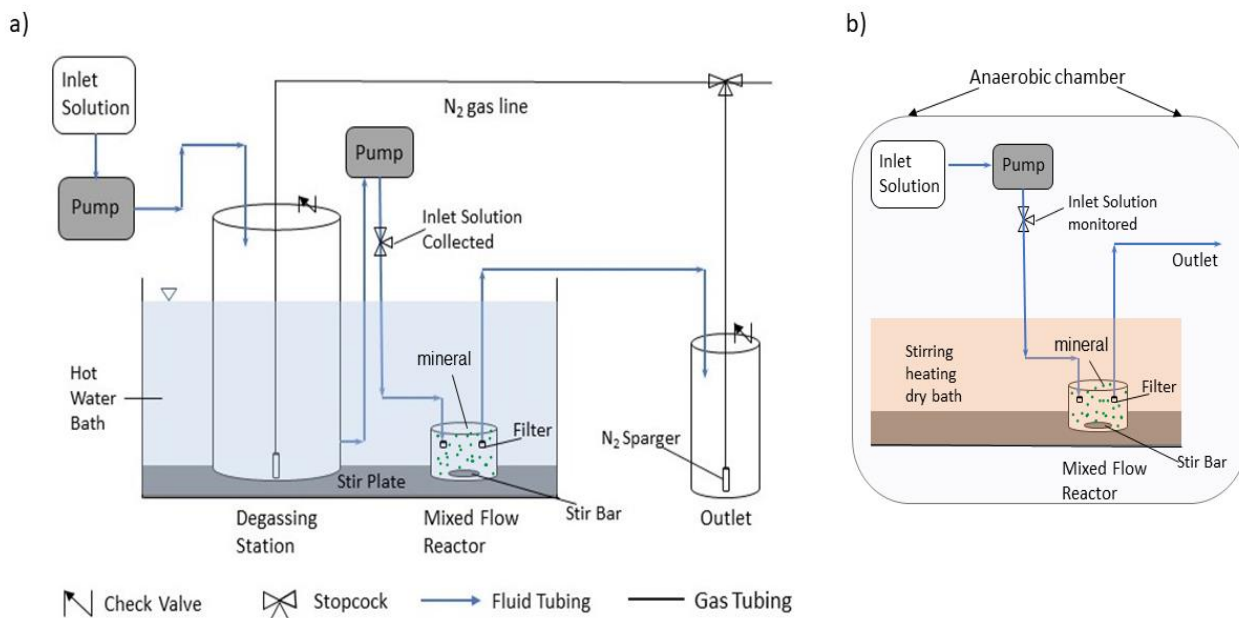


Figure 3-2 Experimental apparatus that maintained strictly anoxic environments and constant temperatures.

Experimental apparatus that maintained strictly anoxic environments and constant temperatures. a) Experiments were heated using a circulating water bath. Inlet solutions were prepared in 4L collapsible LDPE bladders and sealed in the Coy anaerobic chamber; all the tubings and connections were purged with N₂ prior to the flow started. The bulk inlet solutions were pumped through PTFE tubings into the degassing station. The degassing station consisted of an airtight Teflon bottle filled with inlet solutions (no head space), a N₂ sparger, and a check valve that allows gas to escape from the solutions. The degassing station serves two functions: 1) to remove any residual dissolved O₂ in the system, potentially introduced during the assemblage of the experiments and 2) to heat the inlet solution thoroughly and to release the degasification from heated solutions, this step is essential to prevent leakage due to gas buildup in the mixed flow reactor. The N₂ purged inlet solutions then slowly passed through the degassing station into the mixed flow reactor to react with the minerals. The reacted solutions were collected at the outlet in a sealed bottle with a N₂ sparger, which prevents oxidation of the fluids prior to sampling. b) Experimental setup in the Coy anaerobic chamber as described in Sect. 3.3.2.

3.2.3 Solution Analyses

Outlet solutions collected in sealed LDPE bottles were weighed prior to sampling to calculate flow rates. The pH was measured at room temperature (~23°C) on an aliquot of each sample using a Thermo Scientific™ PerpHecT™ Orion™ ROSS™ combination pH microelectrode, calibrated daily

using NIST-traceable pH 4, 7, and 10 buffers. In-situ pH values at the elevated experimental temperatures (Table 3-5) were computed using the Geochemist's Workbench (GWB) computer program (Bethke et al., 2018); the resultant in-situ pH values are typically within ± 0.02 pH units of the room-temperature measurements. Approximately 10 mL of the outlet fluids were sampled each time. Samples for cation analysis were filtered using 0.22 μm PVDF syringe filters, then acidified with trace-metal grade nitric acid (resulting in dilution factors (DFs) ≤ 1.05). The acidified fluid samples were stored in 15 mL centrifuge tubes and kept refrigerated prior to analysis.

Cation (K, Mg, Fe, Al, and Si) concentrations in experimental solutions were analyzed using a Varian 725-ES Inductively Coupled Plasma Optical Emission Spectrometer (ICP-OES) at the University of Calgary. Prior to each analysis, the ICP-OES was calibrated ($r^2 > 0.999$) via serial dilution of certified standards (BDH Limited). Analytical precision and accuracy for these analyses are typically better than $\pm 5\%$, and thus 5% is used to calculate the errors on fluid elemental concentrations discussed below. Although our Type I and Type II glauconites contain small amounts of Na and Ca, neither of these elements was analyzed in our outlet solutions. Na was not measured due to its high concentration in many inlet solutions that would overwhelm the signals caused by the dissolved load, and Ca was not measured because of its very low concentration in the dissolving glauconite.

3.2.4 Rate Calculation, Uncertainties, and the Propagation of Errors

The net glauconite dissolution rates (r) ($\text{mol m}^{-2} \text{s}^{-1}$) were computed from the measured steady-state effluent solution compositions using:

$$r = \frac{\Delta C_i Q}{V_i S_{BET} M} \quad \text{Eq. 3-1}$$

where ΔC_i represents the concentration differences between the inlet and outlet of the i -th element in the solution (mol kg^{-1}), Q is the fluid mass flow rate (kg s^{-1}), V_i refers to the stoichiometric number of moles of the i -th element in one mole of the glauconite, S_{BET} denotes the BET specific surface area of the initial glauconite ($\text{m}^2 \text{g}^{-1}$), and M is the initial mass of glauconite in the reactor (g).

Experimental determination of mineral dissolution rates is subject to several limitations resulting from uncertainties in the analytical methods and materials which are used to derive the rate parameters. In order to estimate the uncertainties of the calculated rate law, error propagation methods similar to that presented by Rimstidt (2014) are adopted in this study, which may be described as:

$$\delta q = \sqrt{\sum i \left(\frac{\partial q}{\partial x_i} \delta x_i \right)^2} \quad \text{Eq.3-2}$$

where δq is the error of the calculated parameters, δx_i is the error of the measured elements (Fe, Mg, Si and K) or the intermediate values produced during the calculations.

Uncertainties on fluid elemental concentrations, flow rates, reactive surface areas, and the masses of the reacting minerals were all incorporated into the error calculation. As mentioned above, 5% was used to represent the uncertainties of the ICP-OES elemental concentrations. The uncertainties of flow rates were estimated using the standard deviations of flow rates calculated during individual experiments, the values are typically 10^{-8} - $10^{-9} \text{ kg s}^{-1}$ (± 0.1 -1%). The masses of the reacting minerals were considered constant because the experimental setup prevents minerals from flowing out of the system. Finally, the uncertainties of the BET surface measurements were 0.1251 and 0.1577 m^2g^{-1} , for Type I and Type II glauconites, respectively. Pre-experimental glauconite BET surface areas were used in all calculations, because the 20% increase of surface area was most likely caused by the decrease in grain size over the course of the experiment (discussed below) rather than secondary mineral formation or mineral migration

out of the experimental vessels. Reactive surface areas bear the largest uncertainties in mineral kinetic studies, even if the pre- and post-experimental surface areas of the reacting minerals are known, other factors, such as dislocation density or the presence of disturbed layers, may influence the rates (Lasaga, 1984; Wintsch and Dunning, 1985). As a result, we considered the surface areas constant throughout the experiments, but incorporated the 20% surface area change in the error propagations calculations to provide a conservative estimate of uncertainties. The resultant values of analytical errors are reported in Table 3-5. Due to the very low elemental concentrations and slow flow rates, the values of errors are too small to reflect the variabilities in the experimentally derived dissolution rates as observed in our repeated rate determinations at identical pH and temperature conditions. As a result, we assumed that standard deviations of repeated rate determinations are more indicative of errors in rate determinations. To calculate representative standard deviations, rate determinations with pH differences ≤ 0.2 at a single temperature were combined to calculate the average pH and rate, as well as their respective standard deviations. In instances where only one rate was determined at a particular pH and temperature condition, the average value of the calculated standard deviation was assigned to the measurement.

3.2.5 Derivation of Rate Equation

Glauconite dissolution rates derived from Table 3-5 were used to fit an empirical form of the kinetic rate equation that assumes a pH dependence of the surface area-normalized kinetic rate:

$$Rate_{Glt} = A_{acid} \cdot e^{\frac{-Ea_{acid}}{RT}} \cdot a_{H^+}^n + A_{neutral} \cdot e^{\frac{-Ea_{neutral}}{RT}} \quad \text{Eq. 3-3}$$

where A is the Arrhenius pre-exponential factor ($\text{mol m}^{-2}\text{s}^{-1}$), E_a is the Activation energy (J mol^{-1}), and their subscripts “acid” and “neutral” refers to pH mechanisms considered in this study, R is the universal gas constant ($8.314 \text{ J mol}^{-1}\text{K}^{-1}$), T is the Temperature (K) and n_{H^+} is the reaction order with respect to H^+ ion. The rate dependence on H^+ activity (n) represents the degree of pH dependence of glauconite dissolution. In an effort to produce a rate expression that can be

straightforwardly incorporated into numerical simulators to calculate temperature- and pH-dependant rate constants (k , in $\text{mol m}^{-2} \text{s}^{-1}$), e.g.:

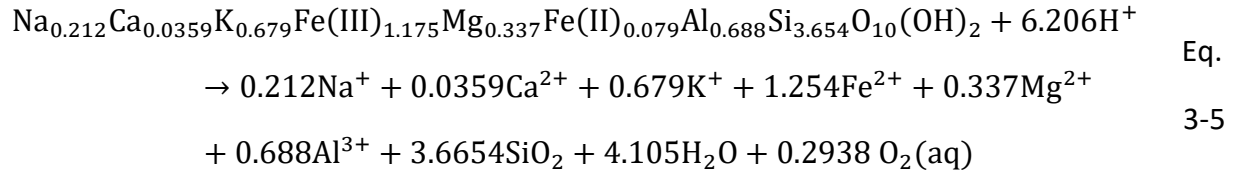
$$\text{rate} = k_{acid} \cdot \exp\left[\left(\frac{-E_{acid}}{R}\right) \cdot \left(\frac{1}{T} - \frac{1}{T_r}\right)\right] \cdot a_{H^+}^n + k_{neutral} \cdot \exp\left[\left(\frac{-E_{neutral}}{R}\right) \cdot \left(\frac{1}{T} - \frac{1}{T_r}\right)\right], \quad \text{Eq.3-4}$$

we used the values derived from fitting of Eq. 3-3 to the experimental data to calculate k_{acid} and $k_{neutral}$ at the reference temperature (T_r) of 298.15 K. Many minerals exhibit a U-shaped relationship between reaction rates and pH (Palandri and Kharaka, 2004), prompting the use of a piecewise linear regression to fit the Arrhenius equation (Eq. 3-3) of individual subsets of the rate data, classified into acid, neutral and basic mechanisms. As discussed below, our experimental data suggest that the glauconite dissolution rates do not exhibit the classic U-shaped relation, and thus the dissolution data was divided into acid and neutral groups with pH ranging from 1.7 to 4.5 and 6 to 12, respectively. Then, using the least-squares minimization method (*curve_fit* function of the Python SciPy module) based on the Levenberg-Marquardt algorithm (More et al., 1980), Eq.3-3 was set as an objective function to find an optimal set of parameters (A , E_a , and n_{H^+}) that best fits each group of experimental dissolution rate data.

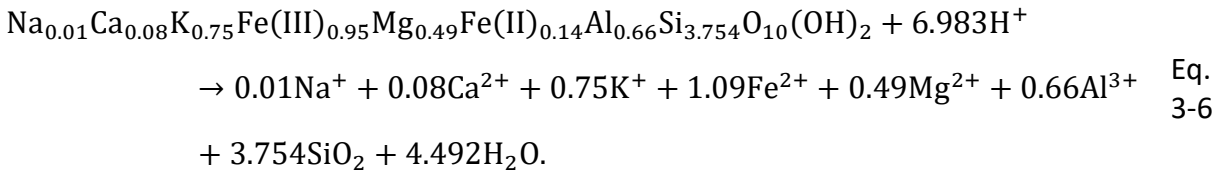
3.2.6 Geochemical Modelling

To put our lab-determined kinetic data into a geological context, we combined the derived glauconite dissolution rate law with a previously developed geochemical model for the CO₂-water-rock interactions in a glauconitic sandstone unit (Zhang and Tutolo, 2021). The modeling was carried out using the Geochemist's Workbench (GWB) software package (Bethke et al., 2018) with a custom thermodynamic database created using the PyGeochemCalc (PyGCC) software package (Awolayo and Tutolo, 2022). As mentioned in Sect. 3.3.1, the wide range of chemical variability of glauconite dictates that the geochemical properties of glauconites will range

significantly depending on their individual compositions. Moreover, few sources of thermodynamic data are available for complex clay minerals such as glauconite. Thus, we calculated the thermodynamic properties specific to the two glauconites based on approach described by Blanc et al. (Blanc et al., 2015) as implemented in PyGCC.



and dissolution of and Type (II) glauconite can be described according to:



In order to explore the impact of reservoir temperature on glauconite dissolution, we used GWB to simulate the reaction of 0.1 kg glauconite (Type II) with 1 kg of glauconitic sandstone reservoir fluid (Table 3-4 (based on Cody and Hutcheon, 1994)) at 35-80 °C. The resultant water-rock ratio of ~10 is consistent with petrological observations (Zhang and Tutolo, 2021). Because O₂ fugacity (log *f*O₂(g)) in these reservoir fluids closely agree with the correlation developed by Helgeson *et al.*, (1993) (Cody, 1993), we used this correlation to calculate the log *f*O₂(g) at each temperature. At 35°C, the O₂ fugacity (log *f*O₂(g)) of ~-73 was calculated using the empirical correlation developed by Helgeson *et al.*, (1993), consistent with Zhang and Tutolo, (2021). At 45, 60 and 80 °C, log *f*O₂(g) is -70, -66 and -63, respectively. We assumed that chalcedony, not quartz, was the dominant silica phase forming at the simulated temperatures (Arnórsson *et al.*, 1983). The reaction path model was initiated by equilibrating 1 kg of the aquifer fluid with a CO₂ fugacity of 50 bars, which is consistent with allowable injection pressures, and then reacting it with 0.1 kg of glauconite.

Table 3-2 Calculated thermodynamic properties of the two types of glauconites used in the flow-through experiments.

Glt	$\Delta G^{\circ}f$ kcal/mol	$\Delta H^{\circ}f$ kcal/mol	S° cal/mol/K	V° cm ³ /mol	a cal/mol/K	b kcal/mol/K ²	c 10 ⁻⁵ cal/mo/K
I ^a	-1169.92	-1253.39	90.79	141.34	77.7088	83.3645	-17.8419
II ^b	-1187.23	-1271.29	88.12	142.24	81.4231	70.9940	-18.6343
^a Na _{0.212} Ca _{0.0359} K _{0.679} Fe(III) _{1.175} Mg _{0.337} Fe(II) _{0.079} Al _{0.688} Si _{3.654} O ₁₀ (OH) ₂							
^b Na _{0.01} Ca _{0.08} K _{0.75} Fe(III) _{0.95} Mg _{0.49} Fe(II) _{0.14} Al _{0.66} Si _{3.754} O ₁₀ (OH) ₂							

Table 3-3 Equilibrium constants for calculating the solubility of glauconites as a function of temperature at steam saturation conditions. (Reactions shown as Eq. 3-5 and Eq. 3-6).

Type	logK							
	0.01°C	20°C	30 °C	40 °C	60 °C	80 °C	90 °C	100 °C
I	12.2587	9.5752	8.3877	7.2904	5.3311	3.6339	2.8671	2.1471
II	13.4061	10.7725	9.6089	8.5345	6.6175	4.2096	4.2097	3.5070

Table 3-4 Water chemistry data and calculated gas fugacity used to simulate the reaction between 0.1 kg glauconite and reservoir pore fluids at various temperatures. The initial activities of Fe⁺⁺ and Al⁺⁺⁺ were set by equilibrium with siderite and kaolinite, respectively.

Chemical	Concentration
Li (mmol/L)	0.586
Na (mmol/L)	123.97
Mg (mmol/L)	0.819
K (mmol/L)	2.24
Ca (mmol/L)	1.48
Fe (mmol/L)	0.003
SiO ₂ (mmol/L)	0.22
Cl (mmol/L)	38.87
HS ⁻ (mmol/L)	3.21
Alk (meq/L)	92.1
Alkc (meq/L)	88.1
Fe (mmol/kg)	10 ⁻²⁵
Al (mmol/kg)	10 ⁻²⁰

3.3 Results

3.3.1 Chemical Analyses

The flow-through experiments approached steady-state within about 7-9 days (~3 residence times) of experiment initialization (Figure 3-3a). Depending on sampling frequency, fluid chemistry measurements used to determine dissolution rates were generally acquired after 5-7

residence times. Typical solution chemistry data displaying the approach to steady-state behavior (Figure 3-3a) demonstrate initially elevated rates of dissolution likely associated with the rapid dissolution of remaining ultrafine particles and/or high-energy surface sites. Measured steady-state outlet solution compositions used to calculate steady-state glauconite dissolution rates were typically 1.4×10^{-5} - 6.8×10^{-7} mol/kg. Virtually no detectable Al was found in any of the effluent solutions, and these measurements are therefore not reported. Only five of the experiments resulted in detectable K concentrations, and thus the K-derived dissolution rates are reported separately in Table 3-6.

Steady-state glauconite dissolution rates were obtained from 41 flow-through experiments conducted at temperatures from 24 to 80 °C, and pH 1.7 to 11.2. If dissolution of the glauconite proceeds stoichiometrically, all elements should be released from the crystal structure in the same ratios as they are initially present (i.e., congruent dissolution). Therefore, we would observe the following elemental ratios in the effluent solutions: Si/Fe \approx 2.6, Si/Mg \approx 10.9 (Type I) and Si/Fe \approx 3.4, Si/Mg \approx 7.7 (Type II). These ratios were indeed observed in some experiments (Table 3-5), especially those with acidic pH (e.g., Figure 3-3b). Surface area-normalized dissolution rates show little difference between the two types of glauconite. For example, Exp. #A-1 is a duplicate of #A, using the same experimental setup and inlet solution, but different types of glauconite, and the 40°C experiments were conducted using both types of glauconite yet remain consistent. Together, these observations suggest that a generalized dissolution mechanism can be derived from our glauconite dissolution experiments conducted with glauconites with different chemistry by normalizing to element abundances in the corresponding glauconite structure.

Glauconite Si, Fe, Mg, and K dissolved nearly stoichiometrically under very acidic pH (pH <2.7) conditions at all experimentally investigated temperatures (Table 3-5 and Table 3-6). However, increasing degrees of K fixation were observed with increasing pH (Sect.3.4.1.2). At higher temperatures, Fe became undetectable in high pH experiments, while dissolved Si and Mg concentrations in outlet fluids remained close to stoichiometric ratios. These resulted in Fe- and K-enriched post-experimental residual glauconites (Figure 3-7). A small amount of secondary precipitate (<1% of the total reacting mineral) was recovered from the 60°C experiments, which

consisted almost entirely of Fe, Si and O, with a Si:Fe ratio of ~1:1. This Si,Fe precipitate, however, was not found in any other post-experimental material.

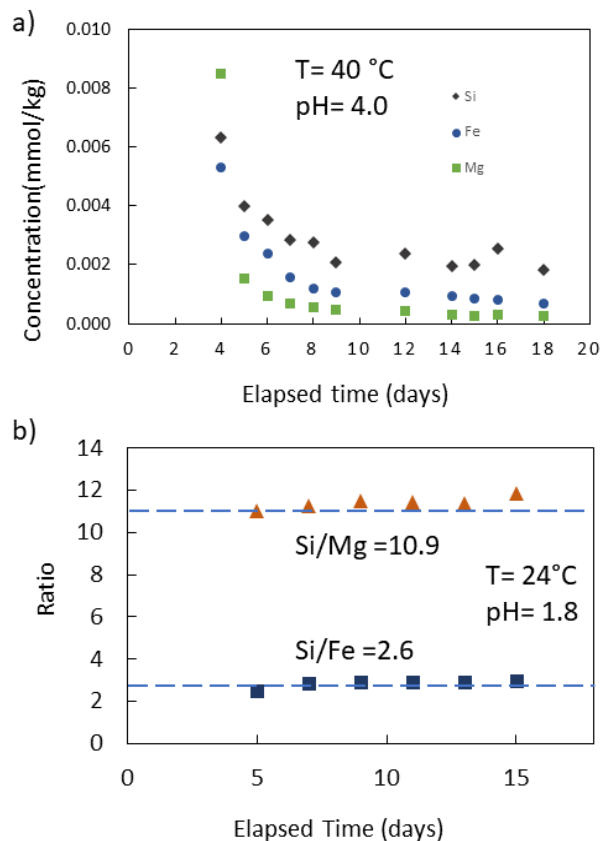


Figure 3-3 Elemental releases from glauconite dissolution experiments.

a) Glauconite dissolution at 40°C, pH=4. Differences of Si, Fe and Mg concentrations between the inlet and outlet solutions as a function of time. b) Steady state outlet Si/Mg and Si/Fe ratios show stoichiometric dissolution at 24°C, pH=1.8, the dashed lines indicate the stoichiometric ratios of the reacting glauconite.

3.3.2 Rate Equation

Kinetic rate parameters (Table 3-7) extracted from silica release rates yielded a rate equation for surface- area-normalized glauconite dissolution at temperatures up to 80 °C and pH 1.7-11.2 as:

$$k = 2.21 \times 10^{-12} \cdot \exp\left[\left(\frac{-32.5}{R}\right) \cdot \left(\frac{1}{T} - \frac{1}{T_r}\right)\right] \cdot a_{H^+}^{0.37} + 2.97 \times 10^{-14} \cdot \exp\left[\left(\frac{-37.7}{R}\right) \cdot \left(\frac{1}{T} - \frac{1}{T_r}\right)\right]$$

Eq. 3-7

The best-fit value for rate dependence of H⁺, n = 0.37, was achieved by fitting the data acquired across all three temperature regimes (Table AB-1 and Figure AB-2). Our experimentally derived dissolution rates at 25°C (log*k_{acid}* = -11.66 and log*k_{neutral}* = -13.53) are significantly lower than the values tabulated by Palandri and Kharaka (2004), log(*k_{acid}*)=-4.80 and log(*k_{neutral}*)=-9.10 ; *Ea* and *n* are also much lower compared to the values derived by Palandri and Kharaka (2004), 85 kJ mol⁻¹ and 0.700, respectively.

3.3.3 Geochemical Modelling

The geochemical modelling results (Figure 3-4) suggest that, under favorable redox conditions, glauconite reacts with reservoir fluids and injected CO₂, readily dissolves, and forms abundant chalcedony, K-feldspar, siderite, with small amounts of kaolinite, dolomite, and magnesite. The initial carbonates most likely sourced their cations from the pore fluid, but as glauconite dissolves, there is a significant increase in siderite. The near-complete reaction of glauconite (> 99% reacted) occurred at 35 °C, 45 °C, 60 °C and 80°C after 11.41, 8.07, 5.05, and 2.94 kyr, respectively.

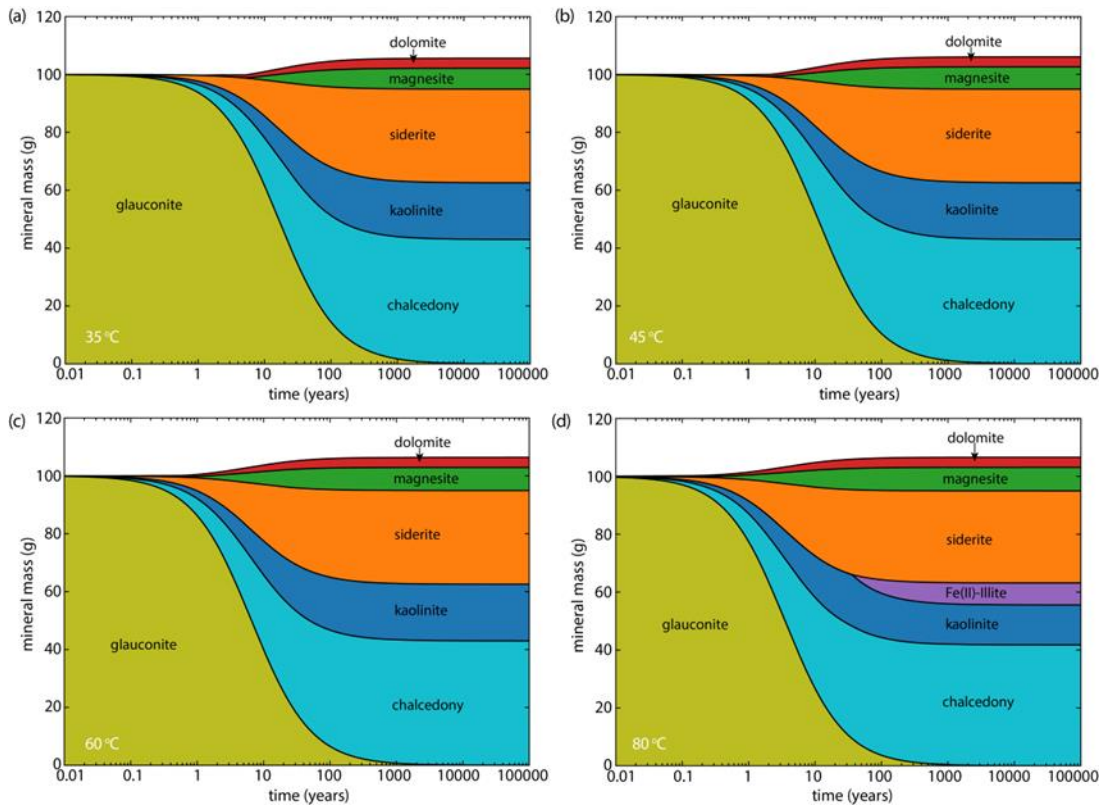


Figure 3-14 Reaction paths calculated by numerically reacting glauconite (Type II) with formation fluids (Table 3-4).

The reaction between 0.1 kg of glauconite and 1 kg of pore fluids at 35°C (a), 45°C (b), 60°C (c) and 80°C (d), respectively. Colored clocks represent the masses (g) of minerals remaining in the system. The reactions were considered completed when 99.9% glauconite had been consumed, which occurred after 17.5, 11.9, 7.1, and 3.8 kyr, respectively.

Table 3-5 Experimental conditions, steady-state chemical fluxes, reacting mineral masses, Mg, Fe, and Si-derived apparent dissolution rates, and analytical errors of glauconite flow-through experiments.

Exp#	T °C	Setup	pH In-situ	Mass g	Outlet		Outlet Si mol/kg	$\Delta\text{Si}/\Delta\text{Mg}$	$\Delta\text{Si}/\Delta\text{Fe}$	Flow Rate kg/s	logR	logR	logR	Error
					Outlet Mg mol/kg	Fe mol/kg					(Mg) mol/m ² /s	(Fe) mol/m ² /s	(Si) mol/m ² /s	
6**	24	Coy ^l	1.76	0.24	3.54E-06	1.41E-05	4.20E-05	11.84	2.98	3.88E-07	-12.39	-12.36	-12.35	0.09
6**	24	Coy ^l	1.76	0.24	3.67E-06	1.43E-05	4.18E-05	11.37	2.92	3.82E-07	-12.38	-12.36	-12.36	0.09
6**	24	Coy ^l	1.85	0.24	3.66E-06	1.44E-05	4.19E-05	11.44	2.91	3.89E-07	-12.37	-12.35	-12.35	0.09
6**	24	Coy ^l	1.88	0.24	3.65E-06	1.44E-05	4.20E-05	11.48	2.92	3.61E-07	-12.41	-12.38	-12.38	0.09
5**	24	Coy ^l	2.26	0.24	1.83E-06	5.79E-06	1.99E-05	10.84	3.43	5.03E-07	-12.56	-12.63	-12.56	0.09
4**	24	Coy ^l	2.64	0.24	1.52E-06	5.74E-06	1.08E-05	7.13	1.88	4.74E-07	-12.67	-12.66	-12.85	0.09
4**	24	Coy ^l	2.66	0.24	1.41E-06	5.76E-06	1.49E-05	10.58	2.59	4.93E-07	-12.68	-12.64	-12.70	0.09
2	24	Coy ^l	4.08	0.24	5.76E-07	1.48E-06	4.37E-06	7.60	2.96	4.72E-07	-13.09	-13.25	-13.25	0.09
2	24	Coy ^l	4.13	0.24	6.82E-07	1.89E-06	5.34E-06	7.82	2.82	4.67E-07	-13.02	-13.15	-13.17	0.09
11	24	Coy ^l	6.95	0.29		9.49E-07	6.23E-06		6.57	4.48E-07		-13.55	-13.20	0.11
12*	24	Coy ^l	7.44	0.29		8.22E-08	2.79E-07		3.39	4.23E-07		-14.64	-14.57	0.09
13*	24	Coy ^l	8.69	0.29	7.60E-07		3.84E-06	5.05		4.95E-07	-13.03		-13.37	0.09
16	24	Coy ^l	9.60	0.29	1.04E-06	3.76E-07	3.00E-06	2.88	7.98	4.00E-07	-12.99	-14.00	-13.57	0.09
16	24	Coy ^l	9.60	0.29	2.48E-07	5.19E-07	3.14E-06	12.66	6.05	4.00E-07	-13.61	-13.86	-13.54	0.09
C**	40	WB ^l	2.69	0.24	5.50E-07	1.25E-06	6.32E-06	11.49	5.06	5.13E-06	-12.08	-12.29	-12.05	0.09
B*	40	WB ^l	3.30	0.24		1.70E-06	2.88E-06		1.69	5.05E-06		-12.16	-12.40	0.10
B-1*	40	Coy ^l	3.30	0.24	2.30E-07	1.65E-06	3.05E-06	13.26	1.84	5.00E-06	-12.47	-12.18	-12.38	0.09

Exp#	T °C	Setup	pH In-situ	Mass g	Outlet		$\Delta\text{Si}/\Delta\text{Mg}$	$\Delta\text{Si}/\Delta\text{Fe}$	Flow Rate kg/s	logR	logR	logR	Error	
					Outlet Mg mol/kg	Outlet Fe mol/kg				(Mg) mol/m ² /s	(Fe) mol/m ² /s	(Si) mol/m ² /s		
B-1*	40	Coy ^I	3.30	0.24		1.04E-06	3.80E-06		3.65	5.00E-06	-12.38	-12.28	0.09	
A*	40	WB ^I	4.00	0.24	2.41E-07	6.90E-07	1.83E-06	7.61	2.66	4.91E-06	-12.45	-12.57	-12.61	0.09
A*	40	WB ^I	4.00	0.24	2.95E-07	8.12E-07	2.56E-06	8.69	3.15	4.95E-06	-12.36	-12.49	-12.46	0.08
A-1*	40	WB ^{II}	4.00	0.24	2.68E-07	8.41E-07	1.99E-06	7.42	2.37	4.89E-06	-12.41	-12.48	-12.57	0.09
D*	40	WB ^I	3.99	0.24	3.37E-07	1.15E-06	4.41E-06	13.08	3.85	6.18E-06	-12.21	-12.25	-12.13	0.09
E*	40	WB ^I	6.43	0.24	9.53E-08	5.57E-08	4.70E-07	4.93	8.44	6.63E-06	-12.73	-13.53	-13.07	0.09
G*	40	WB ^I	8.14	0.24	1.38E-07	5.63E-08	5.88E-07	4.26	10.45	6.19E-06	-12.59	-13.56	-13.00	0.09
X1**	40	Coy ^{II}	1.73	0.2574	1.23E-06	3.35E-06	1.47E-05	11.99	4.38	2.70E-06	-12.32	-12.27	-12.12	0.09
X2*	40	Coy ^{II}	2.30	0.2574	1.23E-06	1.75E-06	8.83E-06	7.17	5.04	2.33E-06	-12.38	-12.27	-12.41	0.09
X2*	40	Coy ^{II}	2.30	0.2574	1.33E-06	1.72E-06	8.12E-06	6.12	4.71	2.33E-06	-12.35	-12.61	-12.45	0.09
X2*	40	Coy ^{II}	2.30	0.2574	1.84E-06	1.84E-06	9.99E-06	5.44	5.44	2.33E-06	-12.21	-12.62	-12.36	0.09
X3	40	WB ^{II}	6.43	0.2574	9.83E-08	1.58E-07	7.81E-07	7.94	4.94	1.07E-06	-13.82	-12.59	-13.80	0.09
X4*	40	WB ^{II}	7.08	0.25	2.28E-07		2.41E-06	10.54		1.09E-06	-13.43		-13.29	0.10
Y2*	40	WB ^{II}	8.82	0.5031	4.40E-07		3.35E-06	7.60		1.19E-06	-13.41		-13.41	0.09
Y2*	40	WB ^{II}	8.82	0.5031	6.55E-07		5.63E-06	8.59		1.19E-06	-13.23		-13.18	0.09
Y4*	40	WB ^{II}	11.1	0.5031	6.80E-07	2.30E-07	6.75E-06	9.93	29.35	1.19E-06	-13.80	-14.08	-13.79	0.09
40*	60	Coy ^{II}	4.00	0.23	2.63E-06	1.78E-06	1.17E-05	4.47	6.59	1.04E-06	-12.35	-12.91	-12.59	0.09
42	60	Coy ^{II}	5.50	0.275	6.29E-06		1.93E-05	3.06		6.79E-07	-12.24		-12.63	0.12

Exp#	T °C	Setup	pH In-situ	Mass g	Outlet Mg mol/kg	Outlet		$\Delta\text{Si}/\Delta\text{Mg}$	$\Delta\text{Si}/\Delta\text{Fe}$	Flow Rate kg/s	logR	logR	logR	Error
						Fe mol/kg	Si mol/kg				(Mg) mol/m ² /s	(Fe) mol/m ² /s	(Si) mol/m ² /s	
44	60	Coy ^{II}	6.27	0.25	1.98E-06		8.13E-06	4.10		1.28E-06	-12.17		-12.29	0.24
41	60	Coy ^I	6.56	0.25	3.51E-06	1.59E-06	1.53E-05	4.35	9.60	1.24E-06	-12.05	-12.78	-12.97	0.09
43	60	Coy ^{II}	7.62	0.25	7.71E-07		4.43E-06	5.75		8.19E-07	-12.84		-12.93	0.13
45	60	Coy ^{II}	8.23	0.25	7.88E-07		5.70E-06	7.23		1.27E-06	-12.82		-12.85	0.10
47	60	Coy ^{II}	8.30	0.25	7.81E-07		4.43E-06	5.67		1.29E-06	-12.82		-12.95	0.09
47	60	Coy ^{II}	8.30	0.25	8.86E-07		3.92E-06	4.43		2.15E-07	-13.55		-13.78	0.17
47-1	60	WB ^{II}	8.30	0.25	6.48E-07		3.43E-06	5.29		2.14E-07	-13.68		-13.84	0.17
47-1	60	WB ^{II}	8.30	0.25	7.10E-07		3.76E-06	5.29		2.17E-07	-13.64		-13.80	0.17
48*	60	Coy ^{II}	9.06	0.25	5.81E-07		6.77E-06	11.65		2.17E-07	-13.72		-13.54	0.15
48*	60	Coy ^{II}	9.06	0.25	7.62E-07		6.72E-06	8.81		2.15E-07	-13.61		-13.55	0.15
39*	80	Parr ^{II}	2.70	0.28	2.86E-05	5.79E-05	1.68E-04	5.88	2.90	6.60E-07	-12.38	-11.68	-11.71	0.09
39*	80	Parr ^{II}	2.70	0.28	3.01E-05	6.12E-05	1.89E-04	6.29	3.09	6.60E-07	-12.30	-11.65	-11.71	0.09
39*	80	Parr ^{II}	2.70	0.28	2.13E-05	4.63E-05	1.21E-04	5.67	2.61	6.60E-07	-12.63	-11.77	-11.66	0.09
38	80	Parr ^{II}	3.30	0.28	9.27E-06	2.10E-05	5.66E-05	6.11	2.69	8.99E-07	-12.11	-11.98	-11.86	0.09
38	80	Parr ^{II}	3.30	0.28	8.39E-06	1.53E-05	5.25E-05	6.25	3.44	8.99E-07	-12.14	-12.12	-12.05	0.09
38	80	Parr ^{II}	3.30	0.28	9.92E-06	1.66E-05	6.09E-05	6.14	3.67	8.99E-07	-12.18	-12.08	-12.08	0.09
36	80	Parr ^{II}	4.00	0.28	6.09E-06		3.33E-05	5.47		9.00E-07	-12.26		-12.02	0.09
36-1	80	Coy ^{II}	4.00	0.28	6.67E-06		3.68E-05	5.52		8.97E-07	-12.39		-12.28	0.09

Exp#	T °C	Setup	pH In-situ	Mass g	Outlet Mg mol/kg	Outlet	Outlet	$\Delta\text{Si}/\Delta\text{Mg}$	$\Delta\text{Si}/\Delta\text{Fe}$	Flow Rate kg/s	logR	logR	logR	Error
						Fe mol/kg	Si mol/kg				(Mg) mol/m ² /s	(Fe) mol/m ² /s	(Si) mol/m ² /s	
34	80	Coy II	6.05	0.3	4.10E-06		1.96E-05	4.77		8.00E-07	-12.51		-12.24	0.44
34	80	Coy II	6.05	0.3	5.63E-06		2.67E-05	4.74		7.31E-07	-12.06		-12.63	0.44
34-1	80	Parr II	6.05	0.3	3.14E-06		1.48E-05	4.73		7.31E-07	-12.10		-12.50	0.44
33	80	Parr II	6.11	0.3	1.09E-05		5.62E-05	5.18		4.49E-07	-11.96		-12.75	0.09
33	80	Parr II	6.11	0.3	1.29E-05		6.24E-05	4.82		4.49E-07	-11.92		-12.39	0.09
33	80	Parr II	6.11	0.3	1.18E-05		5.83E-05	4.92		4.49E-07	-11.89		-12.34	0.09
32	80	Parr II	6.62	0.3	2.67E-06		3.08E-06	1.15		6.55E-07	-11.69		-12.37	0.09
31	80	Parr II	7.17	0.3	5.61E-06		4.13E-05	7.36		6.57E-07	-11.54		-13.48	0.09
31-1	80	Coy II	7.17	0.3	4.75E-06		3.49E-05	7.34		6.57E-07	-11.56		-12.35	0.09

Experimental setups are marked with “I” and “II” to represent Type I and Type II glauconite, respectively. Experiments conducted in the Coy anaerobic chamber are marked as “Coy”, in water bath (described in Figure 3-2) are marked as “WB”, and in Parr reactor are marked as “Parr”. Exp# with “-1” are duplicates of the previous experiments. BET surface area for Type I glauconite is 41.55 m²/g, and Type II glauconite is 54.52 m²/g.

*Experiments with Al and K measurements, but both values were close to detection limits.

**Experiments with Al and K measurements; Al was close to detection limits, and K values are reported in Table 3-6.

Table 3-6 Experimental conditions, steady-state chemical fluxes, reacting glauconite masses, BET surface area measurements, K-derived apparent dissolution rates, and analytical errors of glauconite flow-through experiments.

Exp#	T	Setup	pH	S _{BET}	Mass	Outlet K	Outlet Si	ΔSi/ΔK	Flow Rate	Rate	log(Rate)	Error
	°C		In-situ	m ² /g	g	mol/kg	mol/kg		kg/s	mol/m ² /s	mol/m ² /s	
6	24	Coy ^I	1.76	41.55	0.24	3.95E-06	4.18E-05	10.57	4.67E-07	2.72E-13	-12.56	0.09
6	24	Coy ^I	1.85	41.55	0.24	3.42E-06	4.19E-05	12.24	4.72E-07	2.38E-13	-12.62	0.09
6	24	Coy ^I	1.88	41.55	0.24	2.32E-06	4.2E-05	18.11	4.72E-07	1.61E-13	-12.79	0.09
5	24	Coy ^I	2.26	41.55	0.24	6.49E-06	1.99E-05	3.06	4.9E-07	4.70E-13	-12.33	0.09
4	24	Coy ^I	2.64	41.55	0.24	2.5E-06	8.36E-06	3.34	4.8E-07	1.78E-13	-12.75	0.09
4	24	Coy ^I	2.64	41.55	0.24	3.23E-06	1.07E-05	3.30	4.8E-07	2.29E-13	-12.64	0.09
C	40	WB ^I	2.69	41.55	0.24	1.34E-06	6.32E-06	4.72	4.63E-06	9.15E-13	-12.04	0.09
X1	40	Coy ^{II}	1.73	54.52	0.2574	2.88E-06	1.59E-05	5.50	3.00E-06	8.22E-13	-12.08	0.09
X1	40	Coy ^{II}	1.73	54.52	0.2574	2.82E-06	1.47E-05	5.21	3.00E-06	8.05E-13	-12.09	0.09

Table 3-7 Kinetic rate parameters derived from fitting Arrhenius equation to the measured glauconite dissolution rates.

Glauconite Rate Parameters						
Acid Mechanism				Neutral Mechanism		
log k ₂₅ (mol/m ² /s)	log A (mol/m ² /s)	Ea (kJ/mol)	n	log k ₂₅ (mol/m ² /s)	log A (mol/m ² /s)	Ea (kJ/mol)
-11.66	-6.01	32.20	0.37	-13.53	-6.97	37.45

3.4 Discussion

3.4.1 Elemental Releases from Glauconite

3.4.1.1 Fe, Mg, and Si

Over the experimental temperature range of 24–40 °C, we observed near-stoichiometric to stoichiometric releases of Fe and Mg with respect to Si (Figure 3-5). The Fe content, however, dropped below detection limit for most of the 60 and 80 °C experiments with high pH. To investigate the incongruity of glauconite dissolution at elevated temperature, we performed SEM-EDS measurements on the post-experimental glauconite. These analyses yielded a range of Si/Fe ratio = 0.22-0.92 (Table 3-8), significantly smaller than the pre-experimental ratios of 3.05-3.55 (determined by the same EDS measurement technique), or 3.4 (the reference value reported by SARM). This suggested that Fe was largely retained within the solid phase during these higher-temperature, higher-pH experiments. This observation may be explained by exploring the effect of temperature and pH on Fe solubility (Figure AB-1) – essentially, with increasing temperature, Fe becomes increasingly insoluble in high-pH solutions, such that Fe activity of even just 10⁻⁶ molal would supersaturate and precipitate magnetite (or an Fe₃O₄ component in recrystallized glauconite). It is therefore likely that Fe was undetectable in the neutral to high pH effluent solutions from the 60 to 80 °C experiments due to its retention in the solid phase.

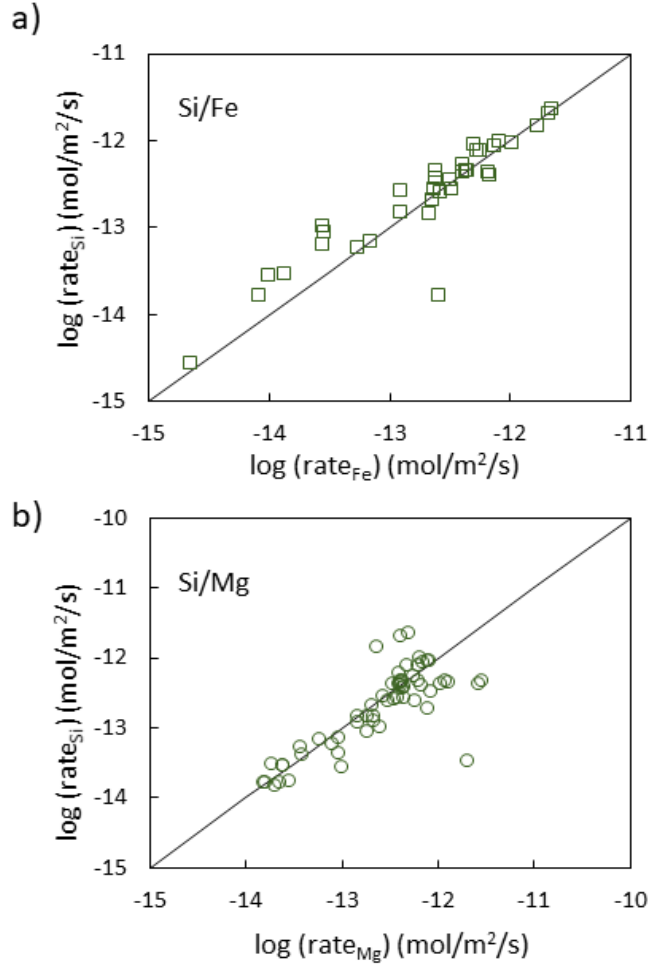


Figure 3-15 Comparison of Si versus Fe (a) and Si versus Mg (b) release rates.

The lines indicate 1:1 ratio. All release rates are normalized to cation abundances in the corresponding glauconite structure.

3.4.1.2 K and Al

Amongst all the experiments, only five contained measurable K in the effluent solutions (Table 3-6), and these were exclusively conducted at very acidic pH ($\text{pH} \leq 2.70$). The detection limit of the ICP-OES for K is $\sim 3 \mu\text{mol/L}$, and if K dissolved stoichiometrically with respect to Mg, Fe or Si, its concentrations in the fluid samples should have been on the order of $30 \mu\text{mol/L}$. However, measured K concentrations (Table 3-6) were an order of magnitude lower. Because the fluid samples were only slightly diluted ($\text{DF} \leq 1.05$) by the addition of small amounts of nitric acid,

dilution was not responsible for the lack of K detection. The pH = 6.5 inlet solution contains significant K (Table 3-1), so K was not analyzed for those experiments. K was below detection limit for all experiments marked with "*" (Table 3-5) and unmarked experiments were not measured due to the lack of detectable K in the majority of previous experiments and the discovery of K-enrichment of glauconite in all post-experimental material (Table 8). EDS spectra were acquired on multiple grains of post-experimental glauconite, resulting in a range of Si/K \approx 1.97-4.25 (cf. pre-experimental ratio Si/K \approx 4.64-5.29, Table 3-8). Since the Si release was close to stoichiometric with respect to Mg and Si (Fig. 5), the large change in Si/K ratios was mainly caused by the immobilization and/or retention of K.

Similar patterns of K dissolution were also observed by Knauss and Wolery (1989) in their muscovite dissolution experiments, where K concentrations were detectable in very acidic pH experiments, but dropped to detection limit in higher-pH experiments. Acidic pH leading to higher K dissolution rates has been observed from other phyllosilicates such as vermiculite and smectite (Huang, 2005). Moreover, soil clay K analyses showed that there is no K fixation by phyllosilicates when pH < 2.5; at higher pH, the degree of K fixation increases rapidly (Sparks and Huang, 2015). The pH-dependent K-release rates could be the one of the contributing factors for the lack of detectable K in many of our effluent solutions. Another mechanism that is known to affect K releases from phyllosilicates is layer charge alteration. This phenomenon is especially well-studied in the case of Fe-rich phyllosilicates in which redox processes change layer charge (reduction of structural Fe³⁺ to Fe²⁺) and promote immobilization of interlayer cations such as K⁺ and Li⁺ (Chen et al., 1987; Florence et al., 2017; Huang, 2005; Komadel et al., 2006; Simonsson et al., 2009). For example, through a series of Fe-reducing processes applied on phyllosilicates, Florence et al. (2017) observed an increase in structural Fe(II) content leading to increases in layer charge and K⁺ fixation, and, as the Fe was subsequently re-oxidized, the K that was previously fixed was released. Similar Fe reduction-induced charge imbalances stabilized by K⁺ uptake into the interlayer during diagenesis of glauconite were observed by López-Quirós et al. (2020).

The detection limit of the ICP-OES for Al is $\sim 0.8 \mu\text{mol/L}$, and virtually no Al was detected in any of our fluid samples. If Al was dissolving stoichiometrically with respect to Si, Mg, or Fe, Al concentrations in the effluent solutions would be on the order of $30 \mu\text{mol/L}$, well above the detection limit. Therefore, incongruent dissolution is likely the cause of the lack of Al in the effluent solutions. Previous studies concerning phyllosilicate dissolution have interpreted such behavior to result from the precipitation of aluminous phases or Al adsorption onto the solid, which in some cases is irreversible (Nagy et al., 1991; Robin et al., 2016; Rozalén et al., n.d.; Smith et al., 2017). Al-enrichment was indeed observed in the post-experimental mineral, where EDS analyses resulted in a range of $\text{Si/Al} \approx 2.06\text{-}4.08$ (cf. pre-experimental ratio $\text{Si/Al} \approx 4.08\text{-}6.17$, Table 3-8).

Table 3-8 Ratios of elements calculated from EDS measurements on glauconite Type II.

Number of measurements (n)= ^a10, ^b15, ^c10, ^d15, ^e15.

Ratios calculated from the chemical composition of Type II glauconite is shown in the last row (determined by SARM Analysis Service Rocks and Minerals).

Locations where some of the measurements were taken are indicated in Figure 3-7.

	Si/Al	Si/K	Si/Fe
Pre-exp Glt ^a	4.08-6.17	4.64-5.29	3.05-3.55
Post-exp Glt (80°C)^b	2.06-2.37	1.97-3.56	0.48-0.64
Post-exp Glt (60°C)^c	2.08-2.99	1.98-3.22	0.22-0.92
Fe-Si phase (60°C)^d	N/A	N/A	0.88-1.02
Post-exp Glt (40°C)^e	3.77-4.08	3.57-4.25	3.77-6.85
Type II Glt (by SARM)	5.7	5.0	3.4

3.4.2 Temperature and pH Dependence of Glauconite Dissolution

Consistent with previous research, we have also observed that higher dissolution rates occur in acidic pH, while neutral pH correlates to the lowest rates (Fernandez-Bastero et al., 2008;

Sverdrup, 1990). Measured rates did not fully develop the classic U-shape typical of silicate mineral dissolution rates (cf. Palandri and Kharaka 2004) as a function of pH (Figure 3-16). Rather, the pH dependence more closely resembles the talc dissolution behavior described by Saldi *et al.* (2007) , where the dissolution rates are highly pH-dependent in acidic pH, and pH-independent at neutral to high pH. While we did not observe much Al and K mobilization in this study, the Fe release rates (at 24 °C) are comparable to those reported by Fernandez-Bastero *et al.*, (2008), and the Si and Mg derived rates are typically lower.

Although 80 °C experiments generally resulted in higher dissolution rates of all elements at lower pH, Fe is virtually undetectable in most of the samples collected from the higher pH experiments (Table 3-5). We used the Parr reactor setup for most of the 80 °C experiments, which were exclusively conducted external to the Coy anaerobic chamber. To account for possible variations in redox conditions in the water bath apparatus and the Parr reactor, we duplicated certain experiments (Exps. #B-1, #47-1, #31-1, #34-1, and #36-1 are duplicates of #B, #47, #31, #34, and #36, respectively, see Table 3-5). Little difference in the resultant dissolution rates was observed (Table 3-5). The Coy anaerobic chamber certainly provides the most reliably reducing conditions, but other apparatuses seem compatible given our efforts to maintain anaerobic conditions. Therefore, the combination of high temperature and high pH is likely the reason for the lack of detectable Fe from 80 °C experiments (Sect. 3.4.1.1).

The calculated rates from the 60 °C experiments in acidic and neutral conditions compared well against the rest of the data (Table 3-5), although a steady decline in rates were observed across Exp. # 45, 47, 47-1, and 48. In the 60 °C post-experimental material, we identified a small amount (<1% of the total reacting mineral) of an Fe,Si-rich phase that had precipitated during the experiments (discovered after Exp. # 45, 47, 47-1, and 48); this phase contains virtually no elements other than Si, Fe and O, with a Si/Fe ratio ≈ 1 (Table 3-8). Although Fe was also largely undetectable from the 80 °C experiments, we did not find an Fe,Si-rich phase in material recovered from the reactor following those experiments. Because of the discovery of the Fe,Si precipitate from the 60 °C post-experimental solids (Figure 3-7), we determined that dissolution rates derived from these experiments do not represent the steady-state glauconite dissolution, rather, they are the bulk rates of a series of dissolution-reprecipitation reactions. One probable

cause for the Fe,Si-rich precipitate is that ultrafine particles that formed during the earlier experiment (Exp. #45) were carried over to the subsequent experiments (Exp. # 47, 47-1, and 48). In order to compare glauconite dissolution rates derived from different experimental conditions, we kept the same reactor and mineral for Exp. # 45, 47, 47-1, and 48, and only changed the inlet solutions and experimental locations (Coy chamber to WB). As a result, this batch of glauconite had reacted for a much longer time (~95 days) than others (~25-45 days). Importantly, using the same mineral for a series of flow-through experiments is a common practice (e.g., Oelkers and Schott, 2001), and generally has little effect on rates because the dissolved load is only a small fraction (< 0.01%) of the reacting mineral (i.e., the small amount of dissolution does not affect the mineral's mass or stoichiometry). This, however, may be less applicable for clay minerals due to their highly friable nature. The ultrafine particles formed from a previous experiment may have dissolved rapidly in the beginning of the next experiment, but effluent solutions from the first 1-6 days were typically not sampled because the system had not reached steady state. If the ultrafine particles had left the flow-through reactor prior to their dissolution (passed through the 10 μm outlet filter as solids) and subsequently accumulated in the outlet container, they would not be detected by the ICP-OES because fluid samples were filtered through 0.22 μm syringe filters prior to acidification. If the ultrafine particles had not exited the reactor, they might reprecipitate in the form of the Fe,Si-rich phase described above. In any case, analytical results would show smaller than expected effluent concentrations, which would result in lower calculated rates. For these reasons, we only used Si-derived rates at 24, 40 and 80 °C experiments to fit the rate equation.

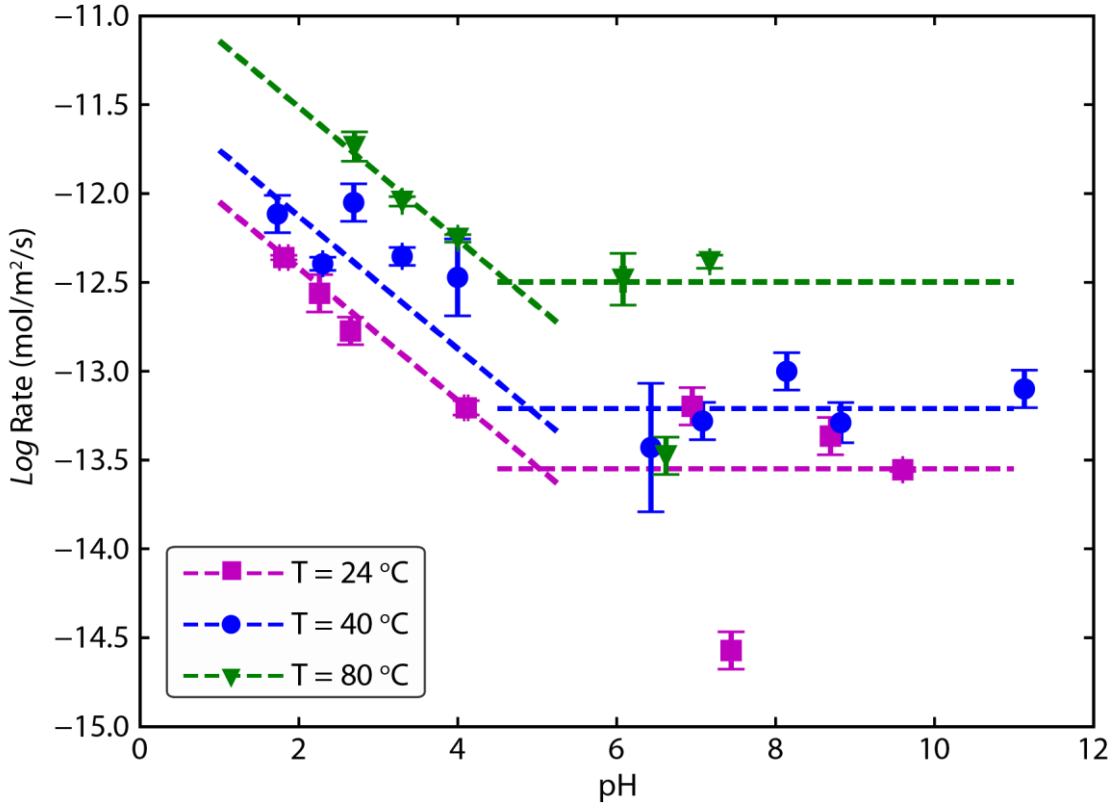


Figure 3-16 Variation of the logarithm of measured steady-state glauconite dissolution rates (derived by Si) as a function of pH.

Error bars represent standard deviations of rates. By combining datapoints with pH differences of ≤ 0.2 at a single temperature, we calculated the average pH and rate, as well as their respective standard deviations. The datapoints that are not combined (i.e., only one rate determination at a particular pH and temperature condition) are assigned the average value of the calculated standard deviations.

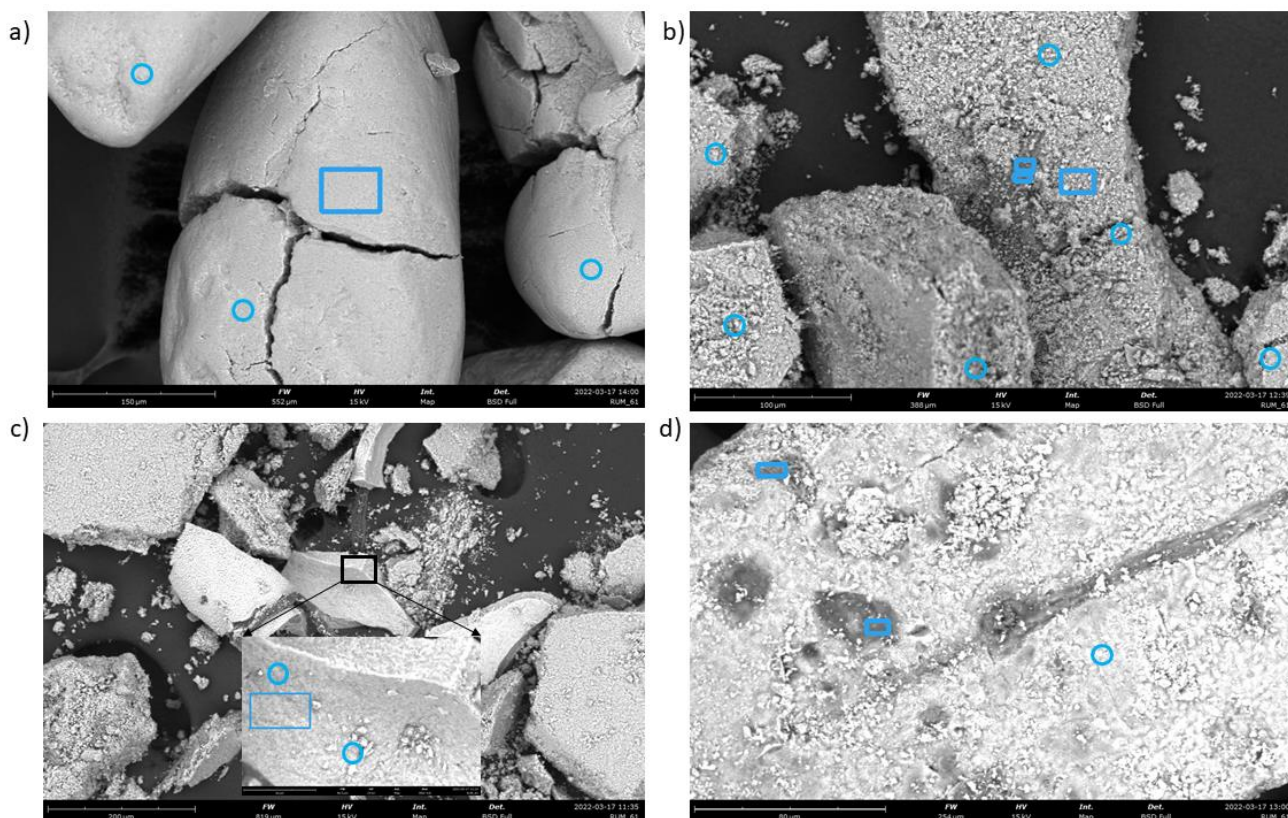


Figure 3-7 Pre-experimental glauconite (a), post-experimental glauconite (b&d) and a Fe-Si secondary precipitate (c).

Blue boxes indicate areas where regional EDS spectra were taken, and blue circles indicate spot EDS analyses. More measurements were taken on other grains and not are included in this figure.

Pre-experimental glauconite pellets (cleaned by 0.1M HCl, before crushing), (b) taken after 80°C experiments, (c) taken after 60°C, and (d) taken after 40°C experiments. The Fe-Si secondary precipitate (c) found in 60°C experiments were identified due to the smooth surface and the lack of rosette microstructure observed in glauconite.

3.4.3 Glauconite kinetics and implication for CO₂ sequestration in glauconite-rich sediments

Far-from-equilibrium glauconite dissolution rates derived by Si, Fe, and Mg release rates range from $\sim 10^{-12}$ to 10^{-13} mol m⁻²s⁻¹ over the examined range of pH and temperature. These rates are 1-2 orders of magnitude higher than the 10^{-14} mol m⁻²s⁻¹ applied by (Xu et al., 2004). As a result, glauconite's potential as a reactive mineral for CO₂ mineralization may have been previously underestimated. Because glauconite dissolution is redox sensitive, the elemental releases

observed in this study are quite different from those observed in oxidizing conditions (e.g., Cloos *et al.*, 1961; Fernandez-Bastero *et al.*, 2008). In efforts to estimate the potential for CO₂ mineralization, the target reservoir's redox state is likely the most important factor to consider, because oxidizing conditions will immobilize Fe as Fe(III) which prevent the formation of siderite (Tutolo *et al.*, 2020). Our geochemical models highlight the importance of temperature dependence of reaction rates. While Xu *et al.* (2004) predicted the complete dissolution of glauconite will take ~17 kyr in their 54°C reservoir, because of their lack of well-constrained glauconite kinetic data, this projection is even slower than our simulation at 45 °C, 11.9 kyr. Our 60°C and 80°C simulations predicted the complete carbonation of glauconite after 7.1 and 3.8 kyr, respectively. This, in turn, indicates that other modeling studies using illite kinetic data as a proxy for glauconite dissolution rates may have also significantly underestimated glauconite's reactivity.

The major issue associated with experimentally derived reaction rates is that such experiments commonly react freshly prepared minerals in well-mixed fluids over relatively short time intervals, thus producing the highest possible rates, and uncertainties are unavoidable when experimental rates are extrapolated to natural weathering environments (White and Brantley, 2003). Moreover, an important feature of the transition state theory (TST) rate law is the presence of a dissolution plateau at a condition far from equilibrium, but the rates plunge exponentially near equilibrium, where natural water-rock interactions commonly occur (Zhu, 2009). These factors, combined with the orders of magnitude difference in flow velocities in porous media, result in the common observation of field dissolution rates that are several orders of magnitude lower than lab-determined rates. Our numerical modelling results represent a simplified system of water-rock-CO₂ interaction which does not reproduce all of the complexities of diagenesis or CO₂ storage in subsurface porous media. Nevertheless, these results show that carbonation of glauconite will require tens of thousands to several thousands of years, depending on the reservoir temperature. The reaction rates, although slow, could still be fast enough to effectively trap CO₂ as minerals due to the long residence time of fluids in deep aquifers that are typically tens- to hundreds-of-thousands of years (Gunter *et al.*, 1997; Xu *et al.*, 2004).

3.5 Conclusions

Steady-state far-from-equilibrium glauconite dissolution rates were measured at pH from 1.7 to 11.2, and temperature from 24 to 80 °C, using mixed flow reactors under strictly anoxic conditions. The dissolution rate constant of glauconite can be best described as:

$$k = 2.21 \times 10^{-12} \cdot \exp \left[\left(\frac{-32.5}{R} \right) \cdot \left(\frac{1}{T} - \frac{1}{T_r} \right) \right] \cdot a_{H^+}^{0.37} + 2.97 \times 10^{-14} \cdot \exp \left[\left(\frac{-37.7}{R} \right) \cdot \left(\frac{1}{T} - \frac{1}{T_r} \right) \right].$$

Our experimental observations, combined with previous experimental and field observations, show that glauconite dissolution mechanisms depend strongly on both pH and solution redox state. Not only does Fe release from the glauconite structure depend on the pH and fluid redox state— i.e., Fe is generally immobile at oxidizing conditions and high pH (regardless of redox)— but the redox state of structural Fe also dictates the release or fixation of K and hence glauconite contribution to alkalinity production and nutrient release. Glauconite dissolution rates are pH dependent in acidic solutions, independent of pH in neutral to alkaline conditions, and generally conform to the Arrhenius equation for temperature dependence. The experimentally derived glauconite dissolution rates are overall higher than those incorporated by previous modelling studies (i.e, rates of illite), which indicates an underestimated potential of glauconite’s role in geologic storage of CO₂.

Acknowledgements

The authors express their gratitude to the funding agencies who made this study possible: the Canada First Research Excellence Fund (CFREF) and National Science and Engineering Research Council of Canada (NSERC) Discovery Grant RGPIN-2018-03800. A.N.A acknowledges financial support from NSERC Postdoctoral Fellowship. We would like to thank Christopher Debuhr and Adnan Younis (University of Calgary) for performing the SEM and BET analyses, respectively.

4 Chapter 4 Evaluation of the Potential of Glauconite in the Western Canadian Sedimentary Basin for Large-Scale Carbon Dioxide Mineralization

Abstract

Geological carbon dioxide (CO₂) storage is an essential and economical measure to mitigate global climate change. CO₂ storage potential in sedimentary reservoirs is commonly passed over in favor of more reactive rock formations, such as basalts, because the latter offer rapid, permanent storage as carbonate minerals while the former are thought to only offer less permanent physical trapping of CO₂. Nevertheless, recent research has demonstrated that carbonation reactions in glauconitic sandstones are favorable under realistic reservoir conditions, although the overall availability of glauconite for carbonation has not yet been quantified. Here, we use calculations based on 11,652 well logs to show that glauconitic sandstones offer significant and previously overlooked potential for sedimentary reservoir-based mineral carbonation. Our results demonstrate that hundreds of gigatons of CO₂ could be sequestered by carbonating the immense quantity of glauconite underlying Alberta, Canada alone. Importantly, these glauconitic sandstones, and others worldwide, have long been exploited for their favorable hydrocarbon production capacity. Thus, global societies eager to limit greenhouse gas emissions may need to look no further than the reservoirs they are already exploiting. Moreover, because the requisite injection infrastructure is oftentimes still active, glauconitic sandstones may present the highest priority, lowest capital cost substrate for mineral carbonation worldwide.

4.1 Introduction

The rapid increase of atmospheric carbon dioxide (CO₂) concentrations has been overwhelmingly attributed to the planet-wide, anthropogenic burning of fossil fuels to meet societal energy needs, a process which is expected to hold disastrous consequences for life on our planet (IPCC, 2021, 2018). The current rate of anthropogenic release of CO₂ into the atmosphere is expected to drive the climate system over tipping points beyond which limiting global warming to 1.5 °C scenarios presented by the IPCC are impossible (IPCC, 2021, 2018; Warszawski et al., 2021). Numerous consequences, such as severe weather, intensive forest fires, stronger hurricanes and floods, and diminishing fresh water supplies, are already being felt around the globe (Moss, 2010; Warszawski et al., 2021). To combat the devastating effects of anthropogenic climate change, global societies must actively reduce CO₂ emissions to the atmosphere. Continued use of fossil fuels as an energy source, even in an intentionally diminishing capacity, will require capturing CO₂, from both point source emitters and directly from the atmosphere, and the long-term prevention of its ever entering or returning to the atmosphere. A key technology for doing this is CO₂ storage and mineralization in geologic reservoirs (Bickle, 2009; DePaolo and Cole, 2013; Lackner, 2002; Seifritz, 1990; Warszawski et al., 2021; Zhang and DePaolo, 2017).

Geological carbon sequestration (GCS) has been explored worldwide by many branches of science and technology in response to the challenge of stabilizing global atmospheric CO₂ concentrations. In GCS, CO₂ can be physically trapped in porous rocks below an impermeable caprock (structural trapping), part of which may become trapped in small pores (residual trapping) or dissolved in groundwater (solubility trapping) and/or react with rocks to form stable carbonate minerals (mineral trapping) (Snæbjörnsdóttir et al., 2020). As the most stable of these mechanisms, mineral trapping is widely considered the most desirable outcome of GCS.

The process of trapping CO₂ by reacting it with cation-bearing silicate minerals to form stable carbonate minerals (herein referred as mineral carbonation, also known as carbon mineralization) was first proposed over 30 years ago (Seifritz, 1990) and was followed by later research that demonstrated its security and permanence (Bickle et al., 2013; DePaolo and Cole, 2013; Lackner, 2002; Oelkers et al., 2008; Snæbjörnsdóttir et al., 2020; Zhang and DePaolo, 2017).

Mineral carbonation requires the initial dissolution of gaseous or supercritical CO₂ into water, where it either forms carbonic acid and provokes silicate mineral dissolution or reacts directly with the cation-rich formation fluids. Alternatively, water is added to supercritical CO₂, and a thin water film forms on the minerals' surfaces (wet supercritical CO₂), creating a highly reactive front that leads to a potential 54% to 116% increase in mineral dissolution rates (Lacinska et al., 2017; Min and Jun, 2018; Thompson et al., 2013). Divalent cations released by silicate mineral dissolution then react with dissolved or wet supercritical CO₂ to form stable carbonate minerals. Rock formations with high supplies of reactive minerals (minerals that readily supply divalent cations such as Fe, Ca and Mg) are therefore crucial for CO₂ mineralization (Baines and Worden, 2004; DePaolo and Cole, 2013; Zhang and DePaolo, 2017). For this reason, (ultra)mafic rock formations, such as basalts and peridotites, are often seen as favorable locations for mineral carbonation reactions, while sedimentary reservoirs such as limestones and sandstones are often assumed to be too poor in these reactive minerals to present significant carbonation opportunities.

Both depleted and active fossil fuel reservoirs offer secure storage space for CO₂ in the subsurface because GCS can reuse the caprocks that were able to trap the buoyant oil and gas in these reservoirs over geologic time to physically trap CO₂. GCS in depleted oil and gas reservoirs is considered to be the most economical method, most importantly, because these reservoirs have been extensively surveyed during the exploitation stage, and pre-existing infrastructure such as wells and pipelines can be re-purposed for CO₂ transport and injection with minor modifications (Bickle, 2009; Fuss et al., 2018; Li et al., 2006; Voormeij and Simandl, 2002). Moreover, pore-pressure and poroelastic stress changes associated with prior oil and gas production make induced seismicity less likely, which means large-scale GCS in depleted oil and gas reservoirs is not only less expensive than, e.g., sub-seafloor strategies, but is also unlikely to cause seismic hazards in continental settings (Dvory and Zoback, 2021). In active reservoirs, CO₂ injection may result in enhanced oil or gas recovery (EOR) and simultaneous CO₂ sequestration, which could also lead to an economic benefit by offsetting the cost of capture (Bachu, 2008; Pooladi-Darvish et al., 2008; Voormeij and Simandl, 2002). By 2001, 69,300 tonnes/day of CO₂ were injected into oil reservoirs for EOR (Moritis, 2001). Although such operations may lead to net positive CO₂

emissions, the screening criteria for operation safety and the reservoir engineering for effective injection are valuable and readily adaptable to the development of CO₂ storage technologies (e.g., Bachu, 2016; Han et al., 2010; Kovscek, 2002).

Global estimates of CO₂ storage capacity in depleted oil and gas fields range from 458 to 923 GtCO₂ (Fuss et al., 2018; Yoshikazu et al., 1993). Nevertheless, these estimates only account for volumetric capacity for structural trapping because mineral trapping is considered negligible in sedimentary basins (Snæbjörnsdóttir et al., 2020). Here, we use the glauconitic sandstones in Alberta, Canada as an example to show that sedimentary basins, particularly glauconite-rich sandstones, not only provide pore space for the physical trapping of CO₂, but also abundant opportunities for stabilizing CO₂ via mineral carbonation, which ensures the security of storage by reducing the reliance on the caprocks over time. The analyses we present here suggest that similar, hydrocarbon-producing, glauconite-rich formations worldwide, such as the Shannon Sandstone Beds in Wyoming, US (Hansley and Whitney, 1991), Chadra sands in Gialo field, Libya (Al-Shaieb and Shelton, 1978), the Great Burgan oil field in Kuwait (El-Sharkawi and Al-Awadi, 1982) and the Sacha oil field of Ecuadorian Oriente (Canfield et al., 1982) likely also offer previously underestimated CO₂ mineralization capacities.

The glauconitic sandstone member of the Mannville Group in the Western Canada Sedimentary Basin (WCSB) was named due to the consistent presence and the widespread distribution of glauconite (Chiang, 1984). The Mannville Group glauconitic sandstone unit in Alberta has been studied as a CO₂ storage site and is amongst the most well-documented glauconitic sandstones in the world (e.g., Abercrombie et al., 2010; Chiang, 1984; Hayes et al., 1994). This wealth of information provides us with valuable and unmatched insights into the parameters governing the capacity for sedimentary reservoir-based CO₂ mineralization worldwide. The Mannville Group is a Cretaceous stratigraphic unit that mainly consists of interbedded continental sand and shale, calcareous sandstone, marine shale, glauconitic sandstone, coal seams and “salt-and-pepper” (often glauconitic) sandstone (Christopher, 1984; Hayes et al., 1994b; Williams, 1963). Mannville deposition was initiated in the Early Cretaceous, as accretion of terranes in the western Cordillera compressed passive margin sediments and thrust them onto the continental margin, creating the vast volume of sediments that shed from upthrust sheets into the foredeep (Hayes et al.,

1994b). The glauconitic sandstone member formed during the highly episodic transgression and subsequent regression of boreal Moosebar Sea in the southern and central parts of the basin (Christopher, 1984; Hayes et al., 1994b). The northern boundary of continental to marginal-marine facies contains a complex of progradational marine sandstone bodies, including the Pembina and Hoadley barriers (Chiang, 1984). In northern Alberta, open-marine conditions prevailed, as recorded by shallow-shelf deposits of the Clearwater Formation (Christopher, 1984; Hayes et al., 1994b). Persistent glauconitic sandstones have been recorded throughout Alberta (Chiang, 1984; Williams, 1963), and complex channel systems have been identified within the glauconitic sandstones (Sherwin, 1996). Although previous studies agreed that the glauconitic sandstones form excellent reservoirs (e.g., Chiang, 1984; Christopher, 1984; Hubbard et al., 1999; Sherwin, 1996), the complexity of the sedimentary environment should not be overlooked. Therefore, calculations in this study only provide a first-order estimate. Detailed, site-specific evaluations will be necessary to determine the effective CO₂ storage capacity.

Observations of some greensands formations, and numerical simulations based on these observations, suggest that glauconite is commonly diagenetically converted to carbonate minerals such as siderite, ankerite, and ferroan dolomite (Chafetz, 2007; Odin, 1988; Zhang and Tutolo, 2021). Harnessing the natural glauconite carbonation processes could thus provide an effective and secure mechanism for permanent sequestration of anthropogenic CO₂ (Zhang and Tutolo, 2021). Therefore, constraining the amount of glauconite available in the subsurface for mineral carbonation is a crucial first step for constraining the potential impact of glauconite carbonation on global CO₂ emissions. Despite the large amount of core data collected over the decades of hydrocarbon production from glauconite-bearing reservoirs, no attempt has been made to estimate the amount of glauconite, and hence mineral carbonation capacity, in relevant subsurface reservoirs. To address this problem, we perform an evaluation of the glauconite budget of the well-studied Mannville Group in Alberta, Canada.

4.1.1 Material and Methods

We extracted 11,856 core logs of wells that intersect with the glauconitic sandstone member within Alberta using the Petro Ninja database. We then selected the 11,652 that reported the glauconitic sandstone member deeper than 800 m, the desirable depth for CO₂ injection which provides the approximate pressure to compress CO₂ to the supercritical state (Voormeij and Simandl, 2002). Using the true vertical depths (TVDs) corresponding to the tops and bottoms of the formation in the well logs, we calculated the stratigraphic thickness of the member at each well location. We used ImageJ (Rasband, 2018) analysis of a geological map (Hayes et al., 1994a) to estimate the glauconitic sandstones' geographical area (Figure AC-1), through which we were able to precisely exclude the shales and fluvial sediments, as well as the area in northern Alberta where the Mannville Group has not been mapped. The specific gravity of glauconite is generally between 2.2 to 2.9, depending on the development stage (Odin and Matter, 1981). Glauconite grains from the glauconitic member of the Mannville Group (Zhang and Tutolo, 2021) were hand-picked and weighed, which resulted in a specific gravity of ~2.5. Virtually no record has been found in the core logs to quantify the amount of glauconite within the glauconitic sandstone member, we therefore assumed that the glauconite makes up at least 5%, and at most 50% by volume of the glauconitic sandstone formation based on petrographic observations (Zhang and Tutolo, 2021). Only ~300 core logs contain porosity data for the glauconitic member; we randomly selected 10% of the records and calculated the average porosity to be 0.14, with running averages of 0.11 - 0.19 at an interval of 5 (Table AC-1). Porosity data is only available if the glauconitic sandstone layer is the producing formation of the well; these records thus most likely represent the higher end of probable porosities. Using this average porosity value will thus result in a conservative estimate of the volume of glauconite in the formation.

We estimated the total available mass (M_{Glt}) of glauconite using a simple calculation with volume of the glauconitic sandstone (V_{SS}) and density (ρ_{Glt}):

$$M_{Glt} = V_{SS} \times (1 - \Phi_{SS}) \times Vol. \%_{Glt} \times \rho_{Glt} \quad \text{Eq. 4-1}$$

in which $Vol. \%_{Glt}$ stands for the percent volume of glauconite within the glauconitic sandstone formation, and Φ_{SS} represents the average porosity of the glauconitic sandstone.

Approximately 2% (270) of the glauconitic member thicknesses are too thin (1 - 5 m) to offer significant sediment input for CO₂ storage, these measurements were still included for statistical purposes. Because the thickness data distribution is positively skewed (Figure 4-1, large numbers >> median), excluding these data points may result in an overestimation of the overall formation thickness. We used the mean thickness (24.3 m) to estimate the total glauconitic sandstone sediment volume, and assigned three abundances (5%, 28% and 50% v/v. glauconite) to represent the three scenarios V_{min} , V_{med} and V_{max} . The glauconite masses were then calculated against three density values of 2200, 2500 and 2900 kg m⁻³ (ρ_{min} , ρ_{med} and ρ_{max}).

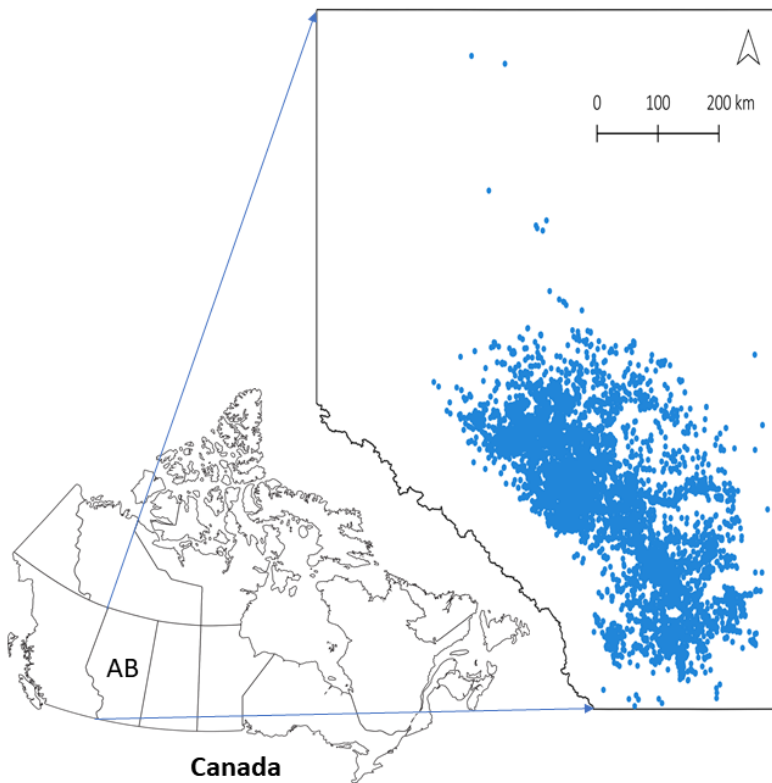


Figure 4-1 Distribution of wells (blue dots) that intersect with the Mannville glauconitic sandstones (> 800 m depth) in Alberta.

4.2 Results

The volume of the glauconitic sandstone member in Alberta is approximately $9.80 \cdot 10^{12} \text{ m}^3$ which results in a total pore volume of $1.37 \cdot 10^{12} \text{ m}^3$ and an estimated total mass of glauconite of 10^3 to 10^4 Gt (Table 4-1). Most of the glauconitic sandstone thickness measurements were between 5 and 50 m, and the average thickness is about 24.3 m (Figure 4-2). Amongst all the available well logs, 1,002 records are from wells currently (as of Aug. 2021) producing from the glauconitic sandstone unit. The mean glauconitic sandstones' thickness calculated from the TVDs of the producing units is 25.9 m. We therefore determined that the mean thickness from all well logs (24.3 m) is conservatively representative of the thicknesses of suitable reservoirs for CO₂ injection. The most conservative estimate of glauconite mass (927 Gt) was produced by the combination of V_{\min} and ρ_{\min} , and the maximum estimate (12,215 Gt) was produced by V_{\max} and ρ_{\max} . The available core logs were overwhelmingly collected from southern Alberta (Figure 4-1), and as mentioned above, the Mannville Group is typically not mapped in detail in northern Alberta. Naturally, the uncertainties of glauconite abundance in the north are much greater than those in the south. In spite of the regional differences and uncertainties, the minimum (927 Gt glauconite in Alberta) is likely an extremely underestimated value, because most characterized glauconitic sandstones contain more than 5% glauconite (Chiang, 1984; Williams, 1963; Zhang and Tutolo, 2021), and ρ_{\min} used in this estimate is the smallest glauconite density ever recorded, which is uncommon (Odin and Matter, 1981). Similarly, it is unlikely that the glauconitic sandstone member contains an average of 50% glauconite with ρ_{\max} . We therefore conclude that the amount of glauconite in Alberta is on the order of 10^3 Gt.

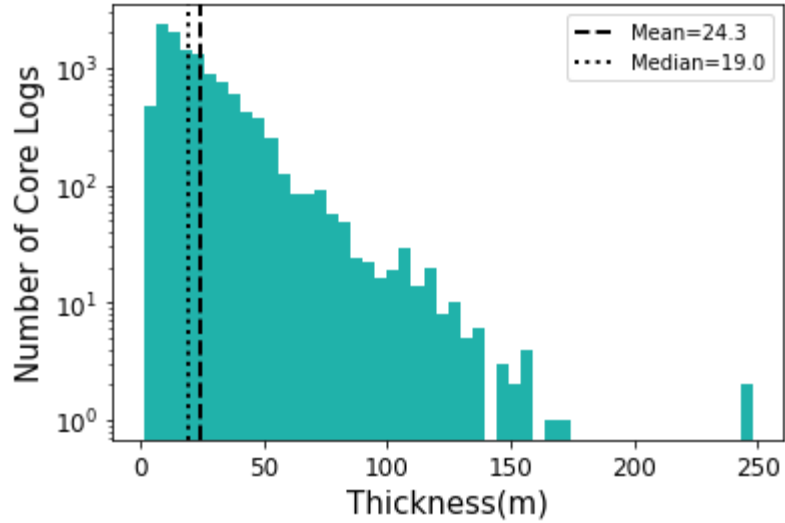


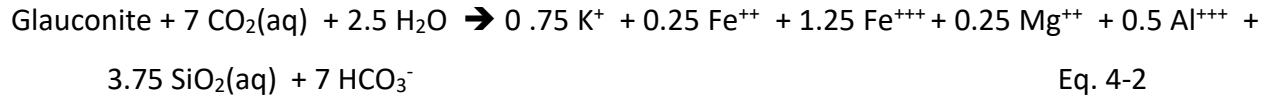
Figure 4-2 Glauconitic sandstone thicknesses calculated from the TVDs recorded in the core logs.

Thickness (m)	Area (km ²)	Φ_{SS}	Vol_{Glt} (%)	V_{Glt} (m ³)	M_{Glt} (Gt)		
					ρ_{min} 2200kgm ⁻³	ρ_{med} 2500kgm ⁻³	ρ_{max} 2900kgm ⁻³
24.3	403,443	0.14	5	$4.90 \cdot 10^{11}$	927 ^a	1,053	1,221
			28	$2.74 \cdot 10^{12}$	5,189	5,897 ^c	6,840
			50	$4.90 \cdot 10^{12}$	9,267	10,530	12,215 ^b

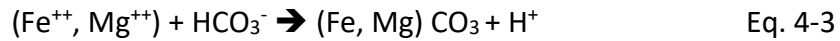
Table 4-1 Parameters used to calculate the total amount of glauconite (M_{Glt}) in the Mannville glauconitic sandstone member in Alberta. The minimum (a) and maximum (b) masses of glauconite. The medium (c) value was used in the following calculations.

4.3 Discussion

Assuming CO₂ is the dominant acid, “ideal” glauconite will dissolve according to (Zhang and Tutolo, 2021):



The dissolved Fe and Mg and alkalinity (HCO_3^-) produced through this reaction can then combine to form carbonate minerals, according to:



As shown in Reaction 2, glauconite naturally contains Fe in both ferrous (Fe(II)) and ferric (Fe(III)) forms. Analyses in the literature suggest that Fe(II)/Fe_{total} in glauconite ranges from ~10 - 20% to as high as 50% (Ali et al., 2001; Mackenzie et al., 1988; Tutolo et al., 2020; Zaitseva et al., 2008); the ideal glauconite in Reaction 2 is 0.167 Fe(II). Once liberated from the glauconite structure, this Fe is readily available to form ferroan carbonate minerals, according to Reaction 3. Under these conditions, 0.5 moles of cations are available to mineralize CO₂. Under favorable conditions (i.e., conditions where fluid redox state is reducing enough to reduce the liberated Fe(III) to Fe(II) (Tutolo et al., 2020b)), which is apparently the case in the Mannville Formation (discussed below), 1 mole of glauconite will produce as much as 1.75 moles of metal cations that can be then mineralize CO₂. Given these stoichiometric considerations, it is reasonable to expect that 0.5 – 1.75 moles of dissolved cations, in the form of Fe⁺⁺ and Mg⁺⁺, will be release per mole of glauconite dissolved.

With these stoichiometric constraints, we can estimate the amount of CO₂ that Mannville glauconite may be capable of mineralizing. To account for likely variations in reaction stoichiometry (e.g., some amount of the released cations may be sequestered as clays or variable amounts of Fe reduction may occur) and chemical variations in the glauconite itself, we perform two calculations: 1) as a minimum estimate, we consider a case in which 1 mole of glauconite can mineralize 0.25 moles of CO₂ (i.e., only half of the released Fe⁺⁺/Mg⁺⁺ and none of the Fe⁺⁺⁺ is available for carbonate formation); 2) as a maximum estimate, we consider a scenario in which 1 mole of glauconite will mineralize 1 mole of CO₂ (i.e., all of the Fe⁺⁺ and Mg⁺⁺ and 40% of the Fe⁺⁺⁺ is available for carbonate formation). Since the molar mass of glauconite (commonly ~450 - 470 g/mol) is ~ 10 times higher than that of CO₂ (44 g/mol), these calculations suggest that, at the minimum, approximately 10 - 40 Gt glauconite will be required to mineralize 1 GtCO₂. These

stoichiometric estimates, combined with our median estimate of 5,897 Gt glauconite in the Mannville Formation (Table 1), suggest that the glauconite in this formation could mineralize an astounding 150 to 590 GtCO₂.

For comparison, Xu et al. predicted a mineralization capacity of 17 kg CO₂ per m³ of rock medium for a glauconite-poor (4.4%) glauconitic sandstone reservoir with 12% porosity (Xu et al., 2004). Applying this capacity to our estimated volume of glauconitic sandstones in Alberta ($9.80 \cdot 10^{12}$ m³), approximately 167 GtCO₂ may be mineralized. This value is close to our minimum estimate (150 GtCO₂) because the capacity was calculated for a reservoir containing only 4.4 % glauconite. As mentioned above, glauconitic sandstones in the Mannville Group are much richer in glauconite than those in Xu's study. Since the CO₂ mineralization capacity is proportional to the availability of glauconite (Xu et al., 2004), applying our medium abundance of glauconite (28 %) in the glauconitic sandstones results in > 1000 GtCO₂ mineralization, a much higher capacity than our stoichiometric calculations estimated. As such, we use the lowest estimate, 150 GtCO₂, for the following discussion so that the most conservative scenario can be addressed.

Our calculations provide a first order estimate of glauconite carbonation capacity in Alberta's subsurface. Detailed geochemical sampling and modeling will result in better estimates of the CO₂ mineralization potential of sedimentary glauconite worldwide. Surveying reservoir conditions will also be necessary to determine the effective CO₂ mineralization capacity. Generally speaking, if the quantities of fossil fuels extracted and reactive minerals required to mineralize the CO₂ their combustion produces are of the same order of magnitude (Voormeij and Simandl, 2002), thousands of gigatons of fossil fuel emissions could be mineralized in the glauconitic sandstones of Alberta. Based on our estimate, at least 150 GtCO₂ could be mineralized in this glauconitic sandstone formation alone. This value is of the same order of magnitude as the lower boundary of global estimates (458 GtCO₂) for CO₂ storage capacity in all depleted oil and gas reservoirs (Fuss et al., 2018). This capacity is sufficient to offset over 200 years of greenhouse gas (GHG) emissions for Canada, based on the total GHG emissions in 2019 of 730 megatons of carbon dioxide equivalent (MtCO₂ eq) (Government of Canada, 2021). To put this into global perspective, the glauconitic sandstones in Alberta could mineralize around 1% of the total CO₂

emissions produced by combusting all fossil fuels on Earth (estimated 18,500 GtCO₂ (Archer, 2005)).

4.3.1 *Challenges and opportunities for glauconite carbonation*

Our previously published petrographic observations, geochemical analyses, and geochemical modeling suggest that pore fluids in the Mannville formation are reducing and able to facilitate the reduction of Fe(III) during glauconite dissolution (Zhang and Tutolo, 2021). In particular, x-ray absorption near-edge spectroscopy (XANES) analyses on glauconite grains suggest that Fe reduction occurs in close proximity to the pore water-glauconite interface, or even potentially while Fe is still in the glauconite structure (Zhang and Tutolo, 2021). Thermodynamic models based on pore water chemistry predict siderite precipitation accompanying glauconite dissolution and Fe reduction, which confirms the conceptual model of reduction-facilitated glauconite carbonation derived from the petrographic and geochemical observations. Based on these interpretations, one may reasonably conclude that much of the Fe present in the glauconite structure is ultimately available for carbonate formation and that the glauconite carbonation, and that the upper bounds of our carbonation capacity estimates may be more accurate. Injecting large quantities of CO₂, however, may perturb the reservoir redox state and prevent Fe⁺⁺ from being available for carbonation reactions. This is accounted for in our lower estimates of mineralization capacity, which, by assuming 0.25 moles of CO₂ could be mineralized per mole of glauconite dissolved, would be consistent with *all* of the liberated Mg⁺⁺ and *none* of the liberated Fe⁺⁺ being available for carbonation. Importantly, these lower-bound estimates still yield substantial estimates of CO₂ mineralization capacities.

In addition, numerous other factors may lead to favorable conditions for enhanced Fe reduction and coupled siderite precipitation. The Mannville group glauconitic sandstones typically have temperatures of ~25-50 °C and total pore water alkalinities in the range of ~10-130 meq/L (Cody and Hutcheon, 1994). Importantly, these reservoir temperatures are optimal for iron-reducing bacterial activity (Slobodkin et al., 1999; Varjani and Gnansounou, 2017), which, combined with the high alkalinity provide favorable conditions for microbially-assisted glauconite carbonation.

Injected CO₂ is commonly mixed with H₂S and NH₄, which are additional reductants that could facilitate glauconite carbonation reactions (Bachu, 2008).

Nevertheless, if CO₂ injection into the Mannville group is implemented at scale, it is likely that the injected CO₂ will overwhelm the reservoir fluid's buffering capacity and reduce the pH (cf. Tutolo et al., 2021). Since carbonate minerals are more soluble at lower pH, the initial injection may lead to dissolution of carbonate minerals in the formation before enough alkalinity can be generated via silicate mineral dissolution (e.g., Reaction 2) to yield net CO₂ carbonation. Provided the caprock seal remains robust, the injected CO₂ will be physically trapped in liquid or supercritical form in the pore space over this time. It is thus reasonable to expect that the pore fluid will eventually return to its pre-injection pH and alkalinity and thereby promote carbonate precipitation (Kharaka et al., 2006). A unique and important avenue for future research will be developing strategies for CO₂ injection, and chemical co-injection, that optimize alkalinity production, iron reduction, and, ultimately, permanent CO₂ mineralization.

Another challenge to utilizing glauconite for CO₂ mineralization lies in the uncertainties in reaction kinetics. Some modeling studies suggested that complete CO₂ mineralization in glauconitic sandstones may require tens of thousands of years (Bacon and Murphy, 2011; Xu et al., 2004), while others predicted hundreds of years (Gunter et al., 1997). The significant difference in reaction time scale is caused by the lack of relevant kinetic data for glauconite dissolution and coupled carbonation reactions. Regardless of the large uncertainties, glauconite reaction rates are most likely sluggish, so the injected CO₂ will require long-term physical trapping (structural/ stratigraphic trapping, residual trapping, and solubility trapping). In other words, even though we aim for the secure and permanent mineral trapping of CO₂, robust and intact caprocks are still one of the most important site-selection criteria.

It is also important to point out that CO₂ immobilization by glauconite carbonation would not overshadow the potential for physical trapping of CO₂ in the same sedimentary formations, because glauconite carbonation, i.e., the conversion of voluminous clays to compact carbonates, should tend to preserve porosity (Xu et al., 2004; Zhang and Tutolo, 2021). Moreover, sufficient porosity to store hundreds of GtCO₂ is available in the glauconitic sandstone in Alberta. Using the

Hoadley Pool of Alberta as an example, the glauconitic sandstones are at ~2000 m depth and the groundwater temperature is ~35 °C (Zhang and Tutolo, 2021), assuming normal hydrostatic pressure, these conditions lead to supercritical CO₂ density of 866 kg/m³. As such, the total porosity required to store 500 GtCO₂ is ~5.8 · 10¹¹ m³, much smaller than the estimated total porosity in the glauconitic sandstones (1.37 · 10¹² m³). This value, of course, is a first-order estimate and would need to be coupled with considerations of the reservoir's effective storage capacity, which is dictated by factors such as sealing ability, storage depth, pressure systems, and pore volume adjusted against residual oil/gas/pore water, to be made more accurate (Bachu, 2016; Bachu and Shaw, 2003; Shen et al., 2009).

Ultimately, commercial-scale GCS implementation is predicated on the cost efficiency of the overall operation. Capital expenditures on infrastructure account for a significant cost driver in GCS implementation, and can impact where CO₂ is best captured and stored and indeed whether an individual GCS operation is economically viable (Middleton and Yaw, 2018).

Hydrocarbon production infrastructure such as injection and production wells and pipelines commonly have service lifetimes that exceed their intended purpose (Noothout et al., 2014). Repurposing the infrastructure for CO₂ storage can thus drastically reduce GCS project costs (Bickle, 2009; Fuss et al., 2018; Li et al., 2006; Voormeij and Simandl, 2002). Although numerous factors (e.g., pressure, volume, and corrosion specifications) dictate whether a particular piece of existing infrastructure can be repurposed for use in GCS (Noothout et al., 2014), the sheer abundance of such infrastructure in hydrocarbon-producing regions such as Alberta suggests that cost reductions will be realized in this way. Thus, in addition to the Mannville formation's significant capacity for permanently immobilizing CO₂ as solid carbonate minerals, GCS in this formation may also be particularly cost-effective compared to other locations, due to the abundance of pre-existing production and CO₂-based EOR infrastructure (Bachu, 2016, 2008; Bachu and Shaw, 2003).

4.4 Conclusions

Hydrocarbon-producing glauconitic sandstone formations similar to the Mannville formation are common worldwide, suggesting global CO₂ mineralization capacity estimates likely need to be re-examined in light of the significant potential for CO₂ mineralization in glauconitic sandstones. Indeed, glauconite-rich sedimentary basins, including not only the Upper Mannville Formation in southern Alberta, Canada that is the focus of this study, but also the Shannon Sandstone Beds in Wyoming, US (Hansley and Whitney, 1991), Chadra sands in Gialo field, Libya (Al-Shaieb and Shelton, 1978), the Great Burgan oil field in Kuwait (El-Sharkawi and Al-Awadi, 1982) and the Sacha oil field of Ecuadorian Oriente (Canfield et al., 1982), and others should be a major focus for future geological CO₂ mineralization efforts. Hydrocarbon-producing glauconitic sandstones are often documented extensively during the exploration stage, such that less investment will be required for geological surveys prior to CO₂ injection. Additionally, CO₂ transportation costs should be minimized if CO₂ transported using existing pipelines or captured at point sources nearby. Moreover, the requisite injection infrastructure may be reusable from the production stage, which could considerably lower the cost of CO₂ injection. Therefore, glauconitic sandstones may present a widely accessible, low capital cost opportunity for permanent CO₂ immobilization as the world seeks to avert the most catastrophic consequences of global climate change.

Acknowledgements

This work was supported by the Canada First Research Excellence Fund and NSERC through a Discovery Grant [RGPIN-2018- 03800]. We would like to thank Per K. Pedersen (University of Calgary) for assistance with the Petro Ninja database. Finally, we thank two anonymous reviewers for their comments on this manuscript, which helped to improve it significantly.

5 Chapter 5 Conclusions

5.1 Summary

This thesis has been devoted to investigating the potential of glauconite as a resource for mineral storage of anthropogenic CO₂. Chapter 2 has focused on the thermodynamic aspect of glauconite carbonation using the Mannville group in Alberta, Canada, as a natural analogue. We have applied an array of techniques to demonstrate that glauconite carbonation in the Mannville group is a reduction-facilitated, coupled glauconite recrystallization and siderite precipitation reaction. Our geochemical modeling results illustrate that, during reductive glauconite dissolution, Fe is released from the glauconite structure, and an Fe-impoverished, Al-enriched glauconite reprecipitates. This observation is consistent with our microanalyses of glauconite grains, which show that Fe and Al contents of glauconite grains are inversely correlated. The XANES analyses shows that the Fe is reduced while still in the glauconite structure, which provides us with new insights on glauconite alteration mechanisms. In addition to the mineral assemblage and the availability of CO₂, the overall redox state of the reacting fluid ultimately controls the conversion of glauconite into siderite, and fluids in hydrocarbon reservoirs worldwide are poised to promote Fe reduction during CO₂-glauconite-brine interaction. Initially, this Fe may precipitate as pyrite, but, once the initially limited supply of S is exhausted, Fe will be precipitated as siderite. We conclude that the carbonation reactions constitute an important alteration process of glauconite, and the potential for glauconite carbonation as an engineered GCS mechanism is likely immense. Moreover, this chapter demonstrates that mineralization of CO₂ in glauconitic sandstones integrates a complex series of reactions, most importantly the reductive dissolution of glauconite, which highlights the importance of maintaining reducing conditions for the kinetic experiments in the next chapter.

Chapter 3 has been devoted to the development of kinetic parameters of glauconite dissolution in relevant reservoir conditions. Steady-state glauconite dissolution rates, at far-from-equilibrium conditions, were measured at pH from 1.7 to 11.2, and temperature from 24 to 80 °C, using mixed flow reactors in strictly anoxic atmospheres. Glauconite dissolution rate constant can be best described as:

$$k = 2.21 \times 10^{-12} \cdot \exp \left[\left(\frac{-32.5}{R} \right) \cdot \left(\frac{1}{T} - \frac{1}{T_r} \right) \right] \cdot a_{H^+}^{0.37} + 2.97 \times 10^{-14} \cdot \exp \left[\left(\frac{-37.7}{R} \right) \cdot \left(\frac{1}{T} - \frac{1}{T_r} \right) \right],$$

Our experimental observations, combined with previous experimental and field observations, show that glauconite dissolution mechanisms are highly redox dependent – not only does Fe mobilization depend on the fluid redox state, but the redox state of structural Fe also dictates the release or fixation of K and hence glauconite contribution to alkalinity production and nutrient release. Glauconite dissolution rates are highly pH dependent in acidic solutions, and pH independent in neutral to alkaline conditions. The temperature dependence of glauconite dissolution generally conforms to the Arrhenius equation. The experimentally derived glauconite dissolution rates are overall higher than those incorporated by previous modelling studies (i.e., rates of illite), which indicates an underestimated potential of glauconite’s role in geological storage of CO₂.

Chapter 4 seeks to quantitatively constrain the budget of glauconite available for CO₂ mineralization. Using the well-studied Mannville group as an example, we demonstrate that hydrocarbon-producing glauconitic sandstone formations worldwide similar to the Mannville formation may provide immense CO₂ mineralization potential, suggesting global CO₂ mineralization capacity estimates likely need to be re-examined in light of the significant potential for CO₂ mineralization in glauconitic sandstones. Glauconite-rich sedimentary basins, including not only the Upper Mannville Formation in southern Alberta, Canada that is the focus of this study, but also the Shannon Sandstone Beds in Wyoming, US (Hansley and Whitney, 1991), Chadra sands in Gialo field, Libya (Al-Shaieb and Shelton, 1978), the Great Burgan oil field in Kuwait (El-Sharkawi and Al-Awadi, 1982) and the Sacha oil field of Ecuadorian Oriente (Canfield et al., 1982), and others should be a major focus for future geologic CO₂ mineralization efforts. Hydrocarbon-producing glauconitic sandstones are often documented extensively during the exploration stage, such that less investment will be required for geological surveys prior to CO₂ injection. Additionally, CO₂ transportation costs should be minimized if CO₂ is transported using existing pipelines or captured at point sources nearby. Moreover, the requisite injection infrastructure may be reusable from the production stage, which could considerably lower the cost of CO₂ injection. Therefore, glauconitic sandstones may present a widely accessible, low

capital cost opportunity for permanent CO₂ immobilization as the world seeks to avert the most catastrophic consequences of global climate change.

5.2 Implications for Geological CO₂ Storage

As scientists continue to advocate aggressive actions to curb greenhouse gas emissions in order to seize the opportunity to prevent the worst impacts of climate change, it has become clear that dialing back emissions will not be enough, and global societies will need to extract CO₂ from the atmosphere (IPCC, 2022). In spite of many lines of science and technology that are rapidly developing new methods and improving our knowledge for sequestering CO₂, there has not been a single technology implemented to the necessary scale to make a significant impact (IPCC, 2022). Such inaction may result from complex political and cultural environments, but ultimately, commercial-scale CO₂ storage implementation is predicated on the cost efficiency of the overall operation. Capital expenditures on infrastructure account for a significant cost driver in GCS implementation and can impact where CO₂ is best captured and stored and indeed whether an individual GCS operation is economically viable (Middleton and Yaw, 2018). Hydrocarbon production infrastructure such as injection and production wells and pipelines commonly have service lifetimes that exceed their intended purpose (Noothout et al., 2014). Re-purposing the infrastructure for CO₂ storage can thus drastically reduce GCS project costs (Bickle, 2009; Fuss et al., 2018; Li et al., 2006; Voormeij and Simandl, 2002). Although numerous factors (e.g., pressure, volume, and corrosion specifications) dictate whether a particular piece of existing infrastructure can be repurposed for use in GCS (Noothout et al., 2014), the sheer abundance of such infrastructure in hydrocarbon-producing regions such as Alberta suggests that cost reductions will be realized in this way. Thus, in addition to the Mannville formation's significant capacity for permanently immobilizing CO₂ as solid carbonate minerals, GCS in this formation may also be particularly cost-effective compared to other locations, due to the abundance of pre-existing

production and CO₂-based EOR infrastructure (Bachu, 2016, 2008; Bachu and Shaw, 2003). Importantly, this thesis identifies glauconite as a resource (i.e., amount of glauconite that exists in discovered deposits), which is not necessarily a reserve (i.e., amount of glauconite that can be technically used for CO₂ storage at a cost that is financially feasible). Future work such as site-specific surveys and life cycle assessments will be critical to the successful application of GCS in glauconite-rich sediments. Our new understandings about glauconite chemical properties combined with the mineral resource budget of the Mannville Group glauconitic sandstones indicate the necessity of re-evaluating the potential of CO₂ storage in sedimentary reservoirs in Alberta, as well as similar reservoirs worldwide.

Bibliography

- Abercrombie, H.J., Cody, J., Hutcheon, I., Myers, T., 1994. Fluid geochemistry of the Mannville Group, Alberta: physical and chemical processes, implications for basin evolution, in: Calgary: Western Canadian and International Expertise. pp. 307–308.
- Al-Shaieb, Z., Shelton, J.W., 1978. Secondary Ferroan Dolomite Rhombs in Oil Reservoirs, Chadra Sands, Gialo Field, Libya. *Am. Assoc. Pet. Geol. Bull.* 62, 463–468. <https://doi.org/10.1306/C1EA486A-16C9-11D7-8645000102C1865D>
- Andreani, M., Muñoz, M., Marcaillou, C., Delacour, A., 2013. μ XANES study of iron redox state in serpentine during oceanic serpentinization. *Lithos* 178, 70–83. <https://doi.org/10.1016/j.lithos.2013.04.008>
- Archer, D., 2005. Fate of fossil fuel CO₂ in geologic time. *J. Geophys. Res. C Ocean.* 110, 1–6. <https://doi.org/10.1029/2004JC002625>
- Arnórsson, S., Gunnlaugsson, E., Svavarsson, H., 1983. The chemistry of geothermal waters in Iceland. III. Chemical geothermometry in geothermal investigations. *Geochim. Cosmochim. Acta* 47, 567–577. [https://doi.org/10.1016/0016-7037\(83\)90278-8](https://doi.org/10.1016/0016-7037(83)90278-8)
- Awolayo, A.N., Tutolo, B.M., 2022. PyGeochemCalc: A python package for geochemical thermodynamic calculations from ambient to deep Earth conditions.
- Bachu, S., 2016. Identification of oil reservoirs suitable for CO₂-EOR and CO₂ storage (CCUS) using reserves databases, with application to Alberta, Canada. *Int. J. Greenh. Gas Control* 44, 152–165. <https://doi.org/10.1016/j.ijggc.2015.11.013>
- Bachu, S., 2008. CO₂ storage in geological media: Role, means, status and barriers to deployment. *Prog. Energy Combust. Sci.* 34, 254–273. <https://doi.org/10.1016/J.PECS.2007.10.001>
- Bachu, S., Shaw, J., 2003. Evaluation of the CO₂ Sequestration Capacity in Alberta's Oil and Gas Reservoirs at Depletion and the Effect of Underlying Aquifers. *J. Can. Pet. Technol.* 42, 51–61. <https://doi.org/10.2118/03-09-02>
- Bacon, D.H., Murphy, E.M., 2011. Managing Chemistry Underground: Is Co-Sequestration an Option in Selected Formations? *Energy Procedia* 4, 4457–4464. <https://doi.org/10.1016/J.EGYPRO.2011.02.400>

- Baines, S.J., Worden, R.H., 2004. The long-term fate of CO₂ in the subsurface: natural analogues for CO₂ storage. *Geol. Soc. London, Spec. Publ.* 233, 49–85.
- Baldermann, A., Banerjee, S., Czuppon, G., Dietzel, M., Farkaš, J., Löhr, S., Moser, U., Scheibelhofer, E., Wright, N.M., Zack, T., 2022. Impact of green clay authigenesis on element sequestration in marine settings. *Nat. Commun.* 13, 1–11. <https://doi.org/10.1038/s41467-022-29223-6>
- Baldermann, A., Warr, L.N., Letofsky-Papst, I., Mavromatis, V., 2015. Substantial iron sequestration during green-clay authigenesis in modern deep-sea sediments. *Nat. Geosci.* 8, 885–889. <https://doi.org/10.1038/ngeo2542>
- Bansal, U., Banerjee, S., Pande, K., Ruidas, D.K., 2020. Unusual seawater composition of the Late Cretaceous Tethys imprinted in glauconite of Narmada basin, central India. *Geol. Mag.* 157, 233–247. <https://doi.org/10.1017/S0016756819000621>
- Berner, R.A., 1981. A New Geochemical Classification of Sedimentary Environments. *SEPM J. Sediment. Res.* Vol. 51, 359–365. <https://doi.org/10.1306/212F7C7F-2B24-11D7-8648000102C1865D>
- Bethke, C.M., Farrell, B., Sharifi, M., 2018. *GWB Reaction Modeling Guide* 151.
- Bickle, M., Kampman, N., Wigley, M., 2013. Natural Analogues. *Rev. Mineral. Geochemistry* 77, 15–71. <https://doi.org/10.2138/rmg.2013.77.2>
- Bickle, M.J., 2009. Geological carbon storage. *Nat. Geosci.* <https://doi.org/10.1038/ngeo687>
- Blanc, P., Vieillard, P., Gailhanou, H., Gaboreau, S., Gaucher, É., Fialips, C.I., Madé, B., Giffaut, E., 2015. A generalized model for predicting the thermodynamic properties of clay minerals. *Am. J. Sci.* 315, 734–780. <https://doi.org/10.2475/08.2015.02>
- Bornhold, B.D., Giresse, P., 1985. Glauconitic sediments on the continental shelf off Vancouver Island, British Columbia, Canada. *J. Sedimentol. Petrol.* 55, 653–664.
- Brunauer, S., Emmett, P.H., Teller, E., 1938. Adsorption of Gases in Multimolecular Layers. *J. Am. Chem. Soc.* 60, 309–319. <https://doi.org/10.1021/ja01269a023>
- Burst, J., 1958. Glauconite Pellets: Their Mineral Nature and Applications to Stratigraphic

Interpretations". Am. Assoc. Pet. Geol. Bull. 42, 310–327.
<https://doi.org/10.1306/0bda5a7d-16bd-11d7-8645000102c1865d>

Bustin, R.M., 1991. Organic maturity in the western Canada sedimentary basin. *Int. J. Coal Geol.* 19, 319–358. [https://doi.org/10.1016/0166-5162\(91\)90026-F](https://doi.org/10.1016/0166-5162(91)90026-F)

Butler, I.B., Schoonen, M.A.A., Rickard, D.T., 1994. Removal of dissolved oxygen from water: A comparison of four common techniques. *Talanta* 41, 211–215.
[https://doi.org/10.1016/0039-9140\(94\)80110-X](https://doi.org/10.1016/0039-9140(94)80110-X)

Canfield, R.W., Bonilla, G., Robbins, R.K., 1982. Sacha Oil Field of Ecuadorian Oriente. *AAPG BULL* V 66, 1076–1090. <https://doi.org/10.1306/03b5a642-16d1-11d7-8645000102c1865d>

Chafetz, H.S., 2007. Paragenesis of the Morgan Creek Limestone, Late Cambrian, central Texas: Constraints on the formation of glauconite. *Deep. Res. II* 54, 1350–1363.
<https://doi.org/10.1016/j.dsr2.2007.04.002>

Chen, S.Z., Low, P.F., Roth, C.B., 1987. Relation Between Potassium Fixation and the Oxidation State of Octahedral Iron. *Soil Sci. Soc. Am. J.* 51, 82–86.
<https://doi.org/10.2136/sssaj1987.03615995005100010017x>

Chiang, K.K., 1984. The Giant Hoadley Gas Field, South-Central Alberta. *AAPG Special Volumes*, pp. 297–313. <https://doi.org/10.1306/m38441c13>

Christopher, J.E., 1984. The Lower Cretaceous Mannville Group, northern Williston Basin region, Canada. *Can. Soc. Pet. Geol. Mem.* 9 Mesozoic Middle North Am. 9, 109–126.

Cloos, P., Gastuche, M.C., Croegaert, M., 1961. Cinétique de la destruction de la glauconite par l'acide chlorhydrique, étude préliminaire. *Geol. Congr.*

Cody, J., 1993. *Geochemistry of Formation Fluids in the Mannville Group, Southern Alberta: Sources, controls and water-rock interaction of carbon dioxide rich fluids.* University of Calgary.

Cody, J.D., Hutcheon, I.E., 1994. Regional water and gas geochemistry of the Mannville Group and associated horizons, southern Alberta. *Bull. Can. Pet. Geol.* 42, 449–464.

- Cody, J.D., Hutcheon, I.E., Krouse, H.R., 1999. Fluid flow, mixing and the origin of CO₂ and H₂S by bacterial sulphate reduction in the Mannville Group, southern Alberta, Canada. *Mar. Pet. Geol.* 16, 495–510. [https://doi.org/10.1016/S0264-8172\(99\)00012-4](https://doi.org/10.1016/S0264-8172(99)00012-4)
- DePaolo, D.J., Cole, D.R., 2013. Geochemistry of Geologic Carbon Sequestration: An Overview. *Rev. Mineral. Geochemistry* 77, 1–14. <https://doi.org/10.2138/rmg.2013.77.1>
- Dvory, N.Z., Zoback, M.D., 2021. Prior Oil and Gas Production Limits the Occurrence of Injection-Induced Seismicity in the Delaware Basin of West Texas and Southeastern New Mexico. *Geology* 49, 1198–1203. <https://doi.org/10.1130/G49015.1/5346474/g49015.pdf>
- Dyar, M., Melinda, G., E., M., Tasa., D., 2008. *Mineralogy and optical mineralogy*. Mineralogical Society of America, Chantilly, VA.
- Dyar, M.D., Breves, E.A., Gunter, M.E., Lanzirrotti, A., Tucker, J.M., Carey, C.J., Peel, S.E., Brown, E.B., Oberti, R., Lerotic, M., Delaney, J.S., 2016. Use of multivariate analysis for synchrotron micro-XANES analysis of iron valence state in amphiboles. *Am. Mineral.* 101, 1171–1189. <https://doi.org/10.2138/am-2016-5556>
- Eder, V.G., Martín-Algarra, A., Sánchez-Navas, A., Zanin, Y.N., Zamirailova, A.G., Lebedev, Y.N., 2007. Depositional controls on glaucony texture and composition, Upper Jurassic, West Siberian Basin. *Sedimentology* 54, 1365–1387. <https://doi.org/10.1111/j.1365-3091.2007.00885.x>
- El-Sharkawi, M.A., Al-Awadi, S.A., 1982. Alteration products of glauconite in Burgan oil field, Kuwait. *J. Sediment. Petrol.* 52, 999–1002. <https://doi.org/10.1306/212F80AD-2B24-11D7-8648000102C1865D>
- Ellison, E.T., Mayhew, L.E., Miller, H.M., Templeton, A.S., 2020. Quantitative microscale Fe redox imaging by multiple energy X-ray fluorescence mapping at the Fe K pre-edge peak. *Am. Mineral.* 105, 1812–1829. <https://doi.org/10.2138/am-2020-7359>
- Escario, S., Nightingale, M., Humez, P., Tutolo, B.M., 2020. The contribution of aqueous catechol-silica complexes to silicification during carbonate diagenesis. *Geochim. Cosmochim. Acta* 280, 185–201. <https://doi.org/10.1016/j.gca.2020.04.016>
- Farshori, M.Z., 1983. Glauconitic Sandstone, Countess Field “H” Pool, Southern Alberta. *Am. Assoc. Pet. Geol. Bull.* 27–41.

- Fernandez-Bastero, S., Gil-Lozano, C., Briones, M.J.I., Gago-Duport, L., 2008. Kinetic and structural constraints during glauconite dissolution: implications for mineral disposal of CO₂. *Mineral. Mag.* 72, 27–31. <https://doi.org/10.1180/minmag.2008.072.1.27>
- Florence, A., Ransom, M., Mengel, D., 2017. Potassium Fixation by Oxidized and Reduced Forms of Phyllosilicates. *Soil Sci. Soc. Am. J.* 81, 1247–1255. <https://doi.org/10.2136/SSSAJ2016.12.0420>
- Fuss, S., Lamb, W.F., Callaghan, M.W., Hilaire, J., Creutzig, F., Amann, T., Beringer, T., De Oliveira Garcia, W., Hartmann, J., Khanna, T., Luderer, G., Nemet, G.F., Rogelj, J., Smith, P., Vicente, J.V., Wilcox, J., Del Mar Zamora Dominguez, M., Minx, J.C., 2018. Negative emissions - Part 2: Costs, potentials and side effects. *Environ. Res. Lett.* 13. <https://doi.org/10.1088/1748-9326/aabf9f>
- Government of Canada, 2021. Greenhouse gas emissions [WWW Document]. Gov. Canada. URL <https://www.canada.ca/en/environment-climate-change/services/environmental-indicators/greenhouse-gas-emissions.html> (accessed 8.8.21).
- Gunter, W.D., Wiwehar, B., Perkins, E.H., 1997. Aquifer disposal of CO₂-rich greenhouse gases: Extension of the time scale of experiment for CO₂-sequestering reactions by geochemical modelling. *Mineral. Petrol.* 59, 121–140. <https://doi.org/10.1007/BF01163065>
- Han, W.S., McPherson, B.J., Lichtner, P.C., Wang, F.P., 2010. Evaluation of trapping mechanisms in geologic CO₂ sequestration: Case study of SACROC northern platform, A 35-year CO₂ injection site. *Am. J. Sci.* 310, 282–324. <https://doi.org/10.2475/04.2010.03>
- Hansley, P., Whitney, C., 1991. Petrology, diagenesis, and sedimentology of oil reservoirs in Upper Cretaceous Shannon Sandstone beds, Powder River basin, Wyoming. US Government Printing Office.
- Harding, S.C., Nash, B.P., Petersen, E.U., Ekdale, A.A., Bradbury, C.D., Dyar, D., 2014. Mineralogy and Geochemistry of the Main Glauconite Bed in the Middle Eocene of Texas: Paleoenvironmental Implications for the Verdine Facies 9. <https://doi.org/10.1371/journal.pone.0087656>
- Hayes, B.J.R., Christopher, J.E., L. Rosenthal, G.L., McKercher, B., Minken, D., Y.M.Tremblay, Fennell, J., 1994a. Lower Upper Mannville (Glauconitic/Bluesky) Paleogeography [WWW Document]. URL https://static.ags.aer.ca/files/image-content/fg17_05.jpg

- Hayes, B.J.R., Christopher, J.E., Rosenthal, L., Los, G., McKercher, B., Minken, D., Tremblay, Y.M., Fennell, J., Smith, D.G., 1994b. Cretaceous Mannville Group of the western Canada sedimentary basin. *Geol. Atlas West. Canada Sediment. Basin 4*, 317–334.
- Helgeson, H.C., Knox, A.M., Owens, C.E., Shock, E.L., 1993a. Petroleum, oil field waters, and authigenic mineral assemblages Are they in metastable equilibrium in hydrocarbon reservoirs. *Geochim. Cosmochim. Acta* 57, 3295–3339. [https://doi.org/10.1016/0016-7037\(93\)90541-4](https://doi.org/10.1016/0016-7037(93)90541-4)
- Helgeson, H.C., Knox, A.M., Owens, C.E., Shock, E.L., 1993b. Petroleum, oil field waters, and authigenic mineral assemblages: Are they in metastable equilibrium in hydrocarbon reservoirs? *Geochim. Cosmochim. Acta* 57, 3295–3339. [https://doi.org/10.1016/0016-7037\(93\)90541-4](https://doi.org/10.1016/0016-7037(93)90541-4)
- Heřmanská, M., Voigt, M.J., Marieni, C., Declercq, J., Oelkers, E.H., 2022. A comprehensive and internally consistent mineral dissolution rate database: Part I: Primary silicate minerals and glasses. *Chem. Geol.* 597, 120807. <https://doi.org/10.1016/j.chemgeo.2022.120807>
- Hesselbo, S.P., Huggett, J.M., 2001. Glaucony in Ocean-Margin Sequence Stratigraphy (Oligocene-Pliocene, Offshore New Jersey, U.S.A.; ODP Leg 174A). *J. Sediment. Res.* 71, 599–607. <https://doi.org/10.1306/112800710599>
- Hradsky, M., Griffin, M., 1984. Sandstone Body Geometry, Reservoir Quality and Hydrocarbon Trapping Mechanisms in Lower Cretaceous Mannville Group, Taber/ Turin Area, Southern Alberta. *Am. Assoc. Pet. Geol. Bull.*
- Huang, P.M., 2005. Chemistry of potassium in soils, in: *Chemical Processes in Soils*. pp. 227–292. <https://doi.org/10.2136/sssabookser8.c4>
- Hubbard, S.M., Pemberton, S.G., Howard, E.A., 1999. Regional geology and sedimentology of the basal Cretaceous Peace River oil sands deposit, north-central Alberta. *Bull. Can. Pet. Geol.* 47, 270–297.
- Huggett, J., Dennis, P., Gale, A., 2000. Geochemistry of Early Siderite Cements from the Eocene Succession of Whitecliff Bay, Hampshire Basin, U.K. *J. Sediment. Res.* 70, 1107–1117. <https://doi.org/10.1306/112399701107>
- Huggett, J.M., Gale, A.S., 1997. Petrology and palaeoenvironmental significance of glaucony in the Eocene succession at Whitecliff Bay, Hampshire Basin, UK, *Journal of the Geological*

Society.

IPCC, 2022. *Climate Change 2022: Impacts, Adaptation, and Vulnerability. Contribution of Working Group II to the Sixth Assessment Report of the Intergovernmental Panel on Climate Change*. Cambridge Univ. Press.

IPCC, 2021. *Summary for Policymakers*. In: *Climate Change 2021: The Physical Science Basis. Contribution of Working Group I to the Sixth Assessment Report of the Intergovernmental Panel on Climate Change* [Masson-Delmotte, V., P. Zhai, A. Pirani, S. L. Connors, C. Péan. Cambridge Univ. Press.

IPCC, 2018. *Global warming of 1.5°C*. IPCC Spec. Rep. <https://doi.org/10.1038/291285a0>

Ireland, B.J., Curtis, C.D., Whiteman, J.A., 1983. Compositional variation within some glauconites and illites and implications for their stability and origins. *Sedimentology* 30, 769–786. <https://doi.org/10.1111/j.1365-3091.1983.tb00710.x>

Isson, T.T., Planavsky, N.J., 2018. Reverse weathering as a long-term stabilizer of marine pH and planetary climate. *Nature* 560, 471–475. <https://doi.org/10.1038/s41586-018-0408-4>

Ivanovskaya, T.A., Geptner, A.R., Savichev, A.T., Pokrovskii, B.G., Pokrovskaya, E. V., 2014. Siderite microconcretions in the glauconite-bearing clayey-silty rocks of the Khaipakh Formation (Middle Riphean, Olenek Uplift). *Lithol. Miner. Resour.* 49, 519–545. <https://doi.org/10.1134/s0024490214060054>

Jach, R., Starzec, K., 2003. Glaucony from the condensed Lower-Middle Jurassic deposits of the Krizna Unit, Western Tatra Mountains, Poland. *Ann. Soc. Geol. Pol.* 73, 183–192.

Karvonen R.L., Pemberton, S.G., 1989. Reservoir geology of the Upper Mannville Group Jenner O, Jenner F and Suffield J pools in southeast Alberta: an example of multiple incised valley-fill deposits, in: *Geology and Reservoir Heterogeneity*. pp. 9–33.

Kisiel, M., Skiba, M., Skoneczna, M., Maj-Szeliga, K., Błachowski, A., 2018. Weathering of glauconite in an alkaline environment — A case study from Krakow area, Poland. *Catena* 171, 541–551. <https://doi.org/10.1016/j.catena.2018.08.003>

Knauss, K.G., Wolery, T.J., 1989. Muscovite dissolution kinetics as a function of pH at 70°C. *Geochim. Cosmochim. Acta* 53, 1493–1501.

<https://doi.org/10.1016/j.chemgeo.2017.06.003>

Komadel, P., Madejová, J., Stucki, J.W., 2006. Structural Fe(III) reduction in smectites. <https://doi.org/10.1016/j.clay.2005.10.016>

Kong, X.Z., Tutolo, B.M., Saar, M.O., 2013. DBCreate: A SUPCRT92-based program for producing EQ3/6, TOUGHREACT, and GWB thermodynamic databases at user-defined T and P. *Comput. Geosci.* 51, 415–417. <https://doi.org/10.1016/j.cageo.2012.08.004>

Kovscek, A.R., 2002. Screening criteria for CO₂ storage in oil reservoirs. *Pet. Sci. Technol.* 20, 841–866. <https://doi.org/10.1081/LFT-120003717>

Kronen, J.D., Glenn, C.R., 2000. Pristine To Reworked Verdine: Keys To Sequence Stratigraphy in Mixed Carbonate-Siliciclastic Forereef Sediments (Great Barrier Reef). *Mar. Authigenes. From Glob. to Microb.* 387–403. <https://doi.org/10.2110/pec.00.66.0387>

Lacinska, A.M., Styles, M.T., Bateman, K., Hall, M., Brown, P.D., 2017. An experimental study of the carbonation of serpentinite and partially serpentinitised peridotites. *Front. Earth Sci.* 5. <https://doi.org/10.3389/feart.2017.00037>

Lackner, K.S., 2002. Carbonate chemistry for sequestering fossil carbon. *Annu. Rev. Energy Environ.* 27, 193–232. <https://doi.org/10.1146/annurev.energy.27.122001.083433>

Lasaga, A.C., 2014. Kinetic theory in the earth sciences. *Kinet. Theory Earth Sci.* 1–811. <https://doi.org/10.5860/choice.36-4499>

Lasaga, A.C., 1984. CHEMICAL KINETICS OF WATER-ROCK INTERACTIONS., in: *Journal of Geophysical Research*. pp. 4009–4025. <https://doi.org/10.1029/jb089ib06p04009>

Li, Z., Dong, M., Li, S., Huang, S., 2006. CO₂ sequestration in depleted oil and gas reservoirs-caprock characterization and storage capacity. *Energy Convers. Manag.* 47, 1372–1382. <https://doi.org/10.1016/j.enconman.2005.08.023>

López-Quirós, A., Escutia, C., Sánchez-Navas, A., Nieto, F., Garcia-Casco, A., Martín-Algarra, A., Evangelinos, D., Salabarnada, A., 2019. Glaucony authigenesis, maturity and alteration in the Weddell Sea: An indicator of paleoenvironmental conditions before the onset of Antarctic glaciation. *Sci. Rep.* 9. <https://doi.org/10.1038/s41598-019-50107-1>

- López-Quirós, A., Sánchez-Navas, A., Nieto, F., Escutia, C., 2020. New insights into the nature of glauconite. *Am. Mineral.* 105, 674–686. <https://doi.org/10.2138/am-2020-7341>
- Lovejoy, T.E., Nobre, C., 2019. Amazon tipping point: Last chance for action. *Sci. Adv.* <https://doi.org/10.1126/sciadv.aba2949>
- Luhmann, A.J., Tutolo, B.M., Bagley, B.C., Mildner, D.F.R., Scheuermann, P.P., Feinberg, J.M., Ignatyev, K., Seyfried, W.E., 2017. Chemical and physical changes during seawater flow through intact dunite cores: An experimental study at 150–200 °C. *Geochim. Cosmochim. Acta* 214, 86–114. <https://doi.org/10.1016/J.GCA.2017.07.020>
- Ma, J., Shi, X., Lechte, M., Zhou, X., Wang, Z., Huang, K., Rudmin, M., Tang, D., 2022. Mesoproterozoic seafloor authigenic glauconite-berthierine: Indicator of enhanced reverse weathering on early Earth. *Am. Mineral.* 107, 116–130. <https://doi.org/10.2138/am-2021-7904>
- Marcaillou, C., Muñoz, M., Vidal, O., Parra, T., Harfouche, M., 2011. Mineralogical evidence for H₂ degassing during serpentinization at 300°C/300bar. *Earth Planet. Sci. Lett.* 303, 281–290. <https://doi.org/10.1016/j.epsl.2011.01.006>
- Masters, J.A., 2020. Paleogeography of the Lower Cretaceous Mannville Group of Western Canada, in: *Elmworth*. pp. 49–77. <https://doi.org/10.1306/m38441c3>
- McConchie, D.M., Ward, J.B., McCann, V.H., Lewis, D.W., 1979. A Mossbauer investigation of glauconite and its geological significance. *Clays Clay Miner.* 27, 339–348. <https://doi.org/10.1346/CCMN.1979.0270504>
- McRae, S.G., 1972. Glauconite. *Earth-Science Rev.* 8, 397–440. [https://doi.org/10.1016/0012-8252\(72\)90063-3](https://doi.org/10.1016/0012-8252(72)90063-3)
- Metz, V., Amram, K., Ganor, J., 2005. Stoichiometry of smectite dissolution reaction. *Geochim. Cosmochim. Acta* 69, 1755–1772. <https://doi.org/10.1016/j.gca.2004.09.027>
- Middleton, R.S., Yaw, S., 2018. The cost of getting CCS wrong: Uncertainty, infrastructure design, and stranded CO₂. *Int. J. Greenh. Gas Control* 70, 1–11. <https://doi.org/10.1016/j.ijggc.2017.12.011>
- Min, Y., Jun, Y.S., 2018. Wollastonite carbonation in water-bearing supercritical CO₂: Effects of

- water saturation conditions, temperature, and pressure. *Chem. Geol.* 483, 239–246.
<https://doi.org/10.1016/j.chemgeo.2018.01.012>
- More, J.J., Garbow, B.S., Hillstrom, K.E., 1980. User Guide for MINPACK-1. R102 SciPy 0.13.0 Ref. Guid. Bibliogr.
- Moss, B., 2010. Climate change, nutrient pollution and the bargain of Dr Faustus. *Freshw. Biol.* 55, 175–187. <https://doi.org/10.1111/j.1365-2427.2009.02381.x>
- Nagy, K.L., Blum, A.E., Lasaga, A.C., 1991. Dissolution and precipitation kinetics of kaolinite at 80°C and pH 3: the dependence on solution saturation state.
- Noothout, P., Wiersma, F., Hurtado, O., Macdonald, D., Kemper, J., Van Alphen, K., 2014. CO₂ pipeline infrastructure - lessons learnt. *Energy Procedia* 63, 2481–2492.
<https://doi.org/10.1016/j.egypro.2014.11.271>
- Odin, G.S., 1988. Green marine clays : oolitic ironstone facies, verdine facies, glaucony facies, and celadonite-bearing facies : a comparative study. Elsevier.
- Odin, G.S., Matter, A., 1981. De glauconiarum origine. *Sedimentology* 28, 611–641.
<https://doi.org/10.1111/j.1365-3091.1981.tb01925.x>
- Oelkers, E.H., Gislason, S.R., Matter, J., 2008. Mineral carbonation of CO₂. *Elements* 4, 333–337.
<https://doi.org/10.2113/gselements.4.5.333>
- Oelkers, E.H., Schott, J., 2001. An experimental study of enstatite dissolution rates as a function of pH, temperature, and aqueous Mg and Si concentration, and the mechanism of pyroxene/pyroxenoid dissolution. *Geochim. Cosmochim. Acta* 65, 1219–1231.
[https://doi.org/10.1016/S0016-7037\(00\)00564-0](https://doi.org/10.1016/S0016-7037(00)00564-0)
- Palandri, J.L., Kharaka, Y.K., 2004. A compilation of rate parameters of water-mineral interaction kinetics for application to geochemical modeling. USGS Open File Rep. 2004–1068.
<https://doi.org/10.1098/rspb.2004.2754>
- Pestitschek, B., Gier, S., Essa, M., Kurzweil, H., 2012. Effects of Weathering on Glauconite: Evidence from the Abu Tartur Plateau, Egypt. *Clays Clay Miner.* 60, 76–88.
<https://doi.org/10.1346/CCMN.2012.0600107>

- Pooladi-Darvish, M., Hong, H., Theys, S., Stocker, R., Bachu, S., Dashtgard, S., 2008. CO₂ injection for enhanced gas recovery and geological storage of CO₂ in the Long Coulee Glauconite F Pool, Alberta. Proc. - SPE Annu. Tech. Conf. Exhib. 4, 2271–2281. <https://doi.org/10.2118/115789-ms>
- Pratap, Y., Tanvar, H., Moreira, D., Dhawan, N., 2020. Processing of Glauconitic Siltstone for Potash Recovery. Mining, Metall. Explor. 37, 1231–1239. <https://doi.org/10.1007/s42461-020-00218-5>
- R. Perry Glaister, 1959. Lower Cretaceous of Southern Alberta and Adjoining Areas. Am. Assoc. Pet. Geol. Bull. 43, 590–640. <https://doi.org/10.1306/0bda5cc6-16bd-11d7-8645000102c1865d>
- Rasband, W.S., 2018. ImageJ [WWW Document]. Natl. Institutes Heal. Bethesda, Maryland, USA. URL <https://imagej.nih.gov/ij/>
- Rimstidt, J.D., 2014. Geochemical rate models: An introduction to geochemical kinetics, Geochemical Rate Models: An Introduction to Geochemical Kinetics. <https://doi.org/10.1017/CBO9781139342773>
- Robin, V., Tertre, E., Regnault, O., Descostes, M., 2016. Dissolution of beidellite in acidic solutions: Ion exchange reactions and effect of crystal chemistry on smectite reactivity. Geochim. Cosmochim. Acta 180, 97–108. <https://doi.org/10.1016/j.gca.2016.02.009>
- Rozalén, M.L., Huertas, F.J., Brady, P. V, Cama, J., García-Palma, S., Linares, J., n.d. Experimental study of the effect of pH on the kinetics of montmorillonite dissolution at 25 °C. <https://doi.org/10.1016/j.gca.2008.05.065>
- Rudmin, M., Banerjee, S., Makarov, B., Mazurov, A., Ruban, A., Oskina, Y., Tolkachev, O., Buyakov, A., Shaldybin, M., 2019. An investigation of plant growth by the addition of glauconitic fertilizer. Appl. Clay Sci. 180. <https://doi.org/10.1016/j.clay.2019.105178>
- Rudmin, M., Oskina, Y., Banerjee, S., Mazurov, A., Soktoev, B., Shaldybin, M., 2018. Roasting-leaching experiments on glauconitic rocks of Bakchar ironstone deposit (Western Siberia) for evaluation their fertilizer potential. Appl. Clay Sci. 162, 121–128. <https://doi.org/10.1016/j.clay.2018.05.033>
- Saldi, G.D., Köhler, S.J., Marty, N., Oelkers, E.H., 2007. Dissolution rates of talc as a function of solution composition, pH and temperature. Geochim. Cosmochim. Acta 71, 3446–3457.

<https://doi.org/10.1016/j.gca.2007.04.015>

Seifritz, W., 1990. CO₂ disposal by means of silicates. *Nature* 345, 486.

Shekhar, S., Mishra, D., Agrawal, A., Sahu, K.K., 2017. Physical and chemical characterization and recovery of potash fertilizer from glauconitic clay for agricultural application. *Appl. Clay Sci.* 143, 50–56. <https://doi.org/10.1016/j.clay.2017.03.016>

Shen, P., Liao, X., Liu, Q., 2009. Methodology for estimation of CO₂ storage capacity in reservoirs. *Pet. Explor. Dev.* 36, 216–220. [https://doi.org/10.1016/S1876-3804\(09\)60121-X](https://doi.org/10.1016/S1876-3804(09)60121-X)

Sherwin, M.D., 1996. Channel trends in the Glauconitic Member, southern Alberta. *Bull. Can. Pet. Geol.* 44, 530–540.

Simonsson, M., Hillier, S., Öborn, I., 2009. Changes in clay minerals and potassium fixation capacity as a result of release and fixation of potassium in long-term field experiments. *Geoderma* 151, 109–120. <https://doi.org/10.1016/j.geoderma.2009.03.018>

Slobodkin, A.I., Jeanthon, C., L'Haridon, S., Nazina, T., Miroshnichenko, M., Bonch-Osmolovskaya, E., 1999. Dissimilatory reduction of Fe(III) by thermophilic bacteria and archaea in deep subsurface petroleum reservoirs of Western Siberia. *Curr. Microbiol.* 39, 99–102. <https://doi.org/10.1007/s002849900426>

Smith, M.M., Dai, Z., Carroll, S.A., 2017. Illite dissolution kinetics from 100 to 280 ° C and pH 3 to 9. *Geochim. Cosmochim. Acta* 209, 9–23. <https://doi.org/10.1016/j.gca.2017.04.005>

Snæbjörnsdóttir, S.Ó., Sigfússon, B., Marieni, C., Goldberg, D., Gislason, S.R., Oelkers, E.H., 2020. Carbon dioxide storage through mineral carbonation. *Nat. Rev. Earth Environ.* 1, 90–102. <https://doi.org/10.1038/s43017-019-0011-8>

Sparks, D.L., Huang, P.M., 2015. Physical Chemistry of Soil Potassium. *Potassium Agric.* 201–276. <https://doi.org/10.2134/1985.POTASSIUM.C9>

Stork, A.L., Nixon, C.G., Hawkes, C.D., Birnie, C., White, D.J., Schmitt, D.R., Roberts, B., 2018. Is CO₂ injection at Aquistore aseismic? A combined seismological and geomechanical study of early injection operations. *Int. J. Greenh. Gas Control* 75, 107–124. <https://doi.org/10.1016/j.ijggc.2018.05.016>

- Sverdrup, H.U., 1990. The kinetics of base cation release due to chemical weathering. Krieger Publishing Company.
- Thompson, C.J., Loring, J.S., Rosso, K.M., Wang, Z., 2013. Comparative reactivity study of forsterite and antigorite in wet supercritical CO₂ by in situ infrared spectroscopy. *Int. J. Greenh. Gas Control* 18, 246–255. <https://doi.org/10.1016/j.ijggc.2013.07.007>
- Tilley, B.J., Longstaffe, F.J., 1984. Controls on hydrocarbon accumulation in glauconitic sandstone, Suffield heavy oil sands, southern Alberta. *Am. Assoc. Pet. Geol. Bull.* 68, 1004–1023. <https://doi.org/10.1306/ad4616b5-16f7-11d7-8645000102c1865d>
- Triplehorn, D.M., 1967. Morphology, Internal Structure, and Origin of Glauconite Pellets: a Reply. *Sedimentology* 8, 170–171. <https://doi.org/10.1111/j.1365-3091.1967.tb01319.x>
- Tutolo, B.M., Awolayo, A., Brown, C., 2021. Alkalinity Generation Constraints on Basalt Carbonation for Carbon Dioxide Removal at the Gigaton-per-Year Scale. *Environ. Sci. Technol.* <https://doi.org/10.1021/acs.est.1c02733>
- Tutolo, B.M., Kiesel, T., Luhmann, A.J., Solheid, P., Seyfried, W.E., 2020a. Applied Geochemistry Experimental evaluation of the role of redox during glauconite-CO₂-brine interactions. *Appl. Geochemistry* 115, 104558. <https://doi.org/10.1016/j.apgeochem.2020.104558>
- Tutolo, B.M., Kiesel, T., Luhmann, A.J., Solheid, P., Seyfried, W.E., 2020b. Experimental evaluation of the role of redox during glauconite-CO₂-brine interactions. *Appl. Geochemistry* 115. <https://doi.org/10.1016/j.apgeochem.2020.104558>
- Varjani, S.J., Gnansounou, E., 2017. Microbial dynamics in petroleum oilfields and their relationship with physiological properties of petroleum oil reservoirs. *Bioresour. Technol.* 245, 1258–1265. <https://doi.org/10.1016/j.biortech.2017.08.028>
- Voormeij, D.A., Simandl, G.J., 2002. Geological and mineral CO₂ sequestration options: A technical review. *Geosci. Canada* 31, 11–22.
- Warszawski, L., Kriegler, E., Lenton, T.M., Gaffney, O., Jacob, D., Klingensfeld, D., Koide, R., Costa, M.M., Messner, D., Nakicenovic, N., Schellnhuber, H.J., Schlosser, P., Takeuchi, K., van der Leeuw, S., Whiteman, G., Rockström, J., 2021. All options, not silver bullets, needed to limit global warming to 1.5 °C: A scenario appraisal. *Environ. Res. Lett.* 16, 64037. <https://doi.org/10.1088/1748-9326/abfeec>

- Wermund, E.G., 1961. Glauconite in Early Tertiary Sediments of Gulf Coastal Province. *Am. Assoc. Pet. Geol. Bull.* 45, 1667–1696. <https://doi.org/10.1306/bc743719-16be-11d7-8645000102c1865d>
- White, A.F., Brantley, S.L., 2003. The effect of time on the weathering of silicate minerals: why do weathering rates differ in the laboratory and field? *Chem. Geol.* 202, 479–506. <https://doi.org/10.1016/j.chemgeo.2003.03.001>
- Wigley, R., Compton, J.S., 2007. Oligocene to Holocene glauconite-phosphorite grains from the Head of the Cape Canyon on the western margin of South Africa. *Deep. Res. II* 54, 1375–1395. <https://doi.org/10.1016/j.dsr2.2007.04.004>
- Wilke, M., Farges, F., Petit, P.E., Brown, G.E., Martin, F., 2001. Oxidation state and coordination of Fe in minerals: An Fe K-XANES spectroscopic study. *Am. Mineral.* 86, 714–730. <https://doi.org/10.2138/am-2001-5-612>
- Williams, G.D., 1963. The Mannville Group (Lower Cretaceous) of central Alberta. *Bull. Can. Pet. Geol.* 11, 350–368.
- Wintsch, R.P., Dunning, J., 1985. The effect of dislocation density on the aqueous solubility of quartz and some geologic implications: a theoretical approach 90, 3649–3657.
- Xu, T., Apps, J.A., Pruess, K., 2004. Numerical simulation of CO₂ disposal by mineral trapping in deep aquifers. *Appl. Geochemistry* 19, 917–936. <https://doi.org/10.1016/j.apgeochem.2003.11.003>
- Yadav, V.P., Sharma, T., Saxena, V.K., 2000. Dissolution kinetics of potassium from glauconitic sandstone in acid lixiviant. *Int. J. Miner. Process.* 60, 15–36. [https://doi.org/10.1016/S0301-7516\(99\)00083-6](https://doi.org/10.1016/S0301-7516(99)00083-6)
- Yoshikazu, N., Yoshiyuki, T., Masaki, I., Kazuitsu, I., Yuji, S., Hitoshi, K., 1993. Underground Storage of Carbon Dioxide in Unused Aquifers. *kagaku kogaku ronbunshu* 19, 705–713. <https://doi.org/10.1252/kakoronbunshu.19.705>
- Zhang, Q., Tutolo, B.M., 2022. Evaluation of the potential of glauconite in the Western Canadian Sedimentary Basin for large-scale carbon dioxide mineralization. *Int. J. Greenh. Gas Control* 117, 103663. <https://doi.org/10.1016/j.ijggc.2022.103663>

Zhang, Q., Tutolo, B.M., 2021. Geochemical evaluation of glauconite carbonation during sedimentary diagenesis. *Geochim. Cosmochim. Acta* 306, 226–244. <https://doi.org/10.1016/j.gca.2021.05.036>

Zhang, S., DePaolo, D.J., 2017. Rates of CO₂ Mineralization in Geological Carbon Storage. *Acc. Chem. Res.* 50, 2075–2084. <https://doi.org/10.1021/acs.accounts.7b00334>

Zhu, C., 2009. Geochemical Modeling of Reaction Paths and Geochemical Reaction Networks. *Rev. Mineral. Geochemistry* 70, 533–569. <https://doi.org/10.2138/RMG.2009.70.12>

Appendices

Appendix A Supplementary Material for Chapter 2

XANES data can be accessed at: <https://doi.org/10.17605/OSF.IO/5AX8Z>.

Appendix B Supplementary Material for Chapter 3

Table AB-1 Measured mean pH and dissolution rate with the estimated standard deviations utilized in fitting the Arrhenius equation to derive the kinetic parameters in Table 3-7

pH	sigma_pH	Rate	sigma_rate	Temp
1.81	0.0559	-12.3601	0.0126	24
2.26		-12.5617	0.1052	24
2.65	0.0100	-12.7733	0.0778	24
4.11	0.0250	-13.2059	0.0409	24
6.95		-13.1977	0.1052	24
7.44		-14.5721	0.1052	24
8.69		-13.3654	0.1052	24
9.60	0.0000	-13.5547	0.0099	24
1.73		-12.1154	0.1052	40
2.30	0.0000	-12.3952	0.0369	40
2.69		-12.0507	0.1052	40
3.30	0.0000	-12.3536	0.0506	40
4.00	0.0043	-12.4717	0.2165	40
6.43	0.0000	-13.4297	0.3618	40
7.08		-13.2808	0.1052	40
8.14		-13.0006	0.1052	40
8.82	0.0000	-13.2895	0.1130	40
11.13		-13.0997	0.1052	40
2.70	0.0000	-11.7356	0.0823	80
3.30	0.0000	-12.0437	0.0265	80
4.00	0.0000	-12.2523	0.0211	80
6.08	0.0300	-12.4821	0.1455	80
6.62		-13.4759	0.1052	80
7.17	0.0000	-12.3836	0.0370	80

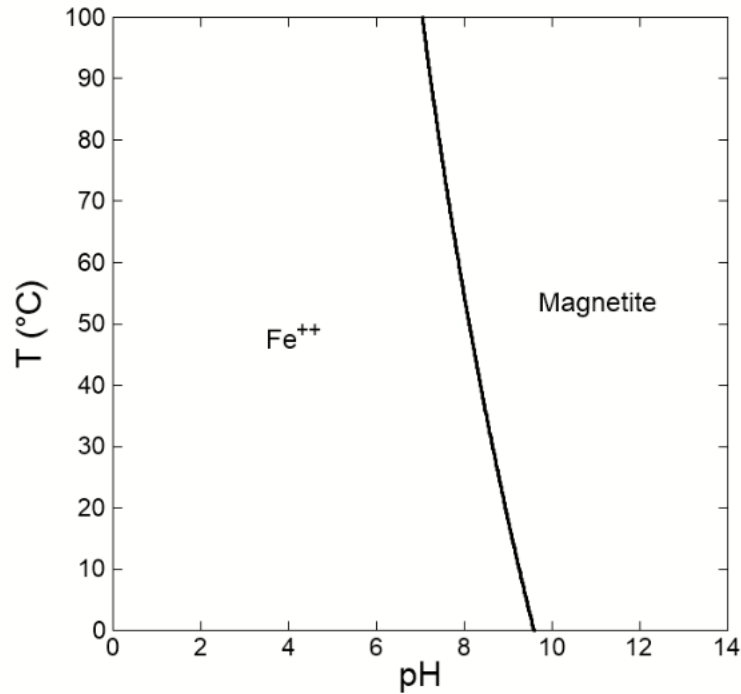


Figure AB-1 Fe solubility as a function of pH and temperature at activity of $\text{Fe}^{2+} = 10^{-6}$, which is consistent with experimental effluent concentrations and the approximate detection limits of our analytical techniques and fugacity of $\text{H}_2(\text{g}) = 0.025$, which is consistent with the atmosphere of the Coy anaerobic chamber. The diagram illustrates the limited solubility of Fe in high-pH solutions at the conditions of our experiments, and suggests the reason for a lack of Fe in effluent solutions from elevated-pH experiments can be attributed to its re-precipitation as magnetite or an Fe_3O_4 component in neoformed glauconite.

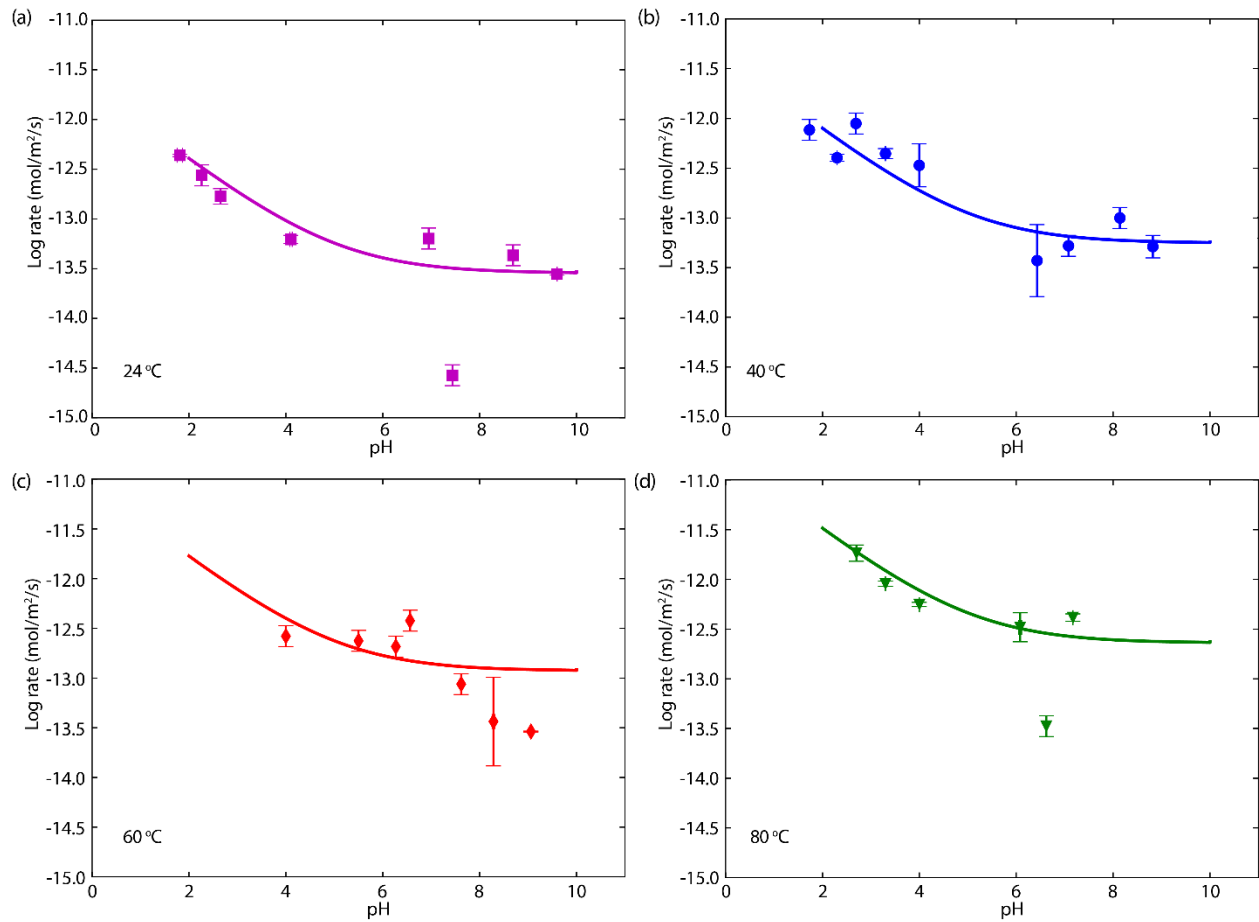


Figure AB-2 Glauconite dissolution rates calculated by implementing Eq. 7 into the Geochemist's Workbench (solid lines) plotted against experimentally measured dissolution rates (data points). The figures illustrate the correct implementation of the derived rate law and the utility of the Geochemist's Workbench in calculating pH- and temperature-dependent glauconite dissolution rates.

Appendix C Supplementary Material for Chapter 4

Table AC-1 Mean porosities calculated from 30 randomly selected core logs.

UWI	TVD (m)	Mean Porosity	Rolling Mean
100/11-21-030-22W4/00	1409-1435	0.1	
100/05-18-030-11W4/00	1060 -1083	0.22	
102/06-06-042-05W5/00	2258 -2277	0.094	
102/06-31-041-05W5/00	2311-2337	0.083	
100/13-21-045-01W5/00	1719-1744	0.13	0.13
100/08-24-033-23W4/00	1452-1549	0.12	0.13
100/02-13-023-14W4/00	985-1004	0.14	0.11
100/14-33-041-05W5/00	2207-2232	0.062	0.11
102/06-07-021-17W4/00	1130-1155	0.15	0.12
100/08-16-030-11W4/00	1040-1049	0.25	0.14
102/10-19-025-19W4/00	1348-1397	0.11	0.14
100/11-21-044-01W5/00	1718-1739	0.12	0.14
100/07-13-044-03W5/00	1863-1891	0.12	0.15
100/04-11-039-10W4/00	961-980	0.22	0.16
100/06-28-044-01W5/00	1727-1749	0.22	0.16
100/13-01-045-02W5/00	1796-1816	0.13	0.16
100/14-19-042-04W5/00	2084-2108	0.07	0.15
100/13-10-039-10W4/00	961-979	0.23	0.17
100/06-32-025-19W4/00	1357-1403	0.16	0.16
100/11-09-042-04W5/00	2083-2114	0.09	0.14
102/06-11-020-09W4/00	962-986	0.25	0.16
100/13-13-053-18W4/00	844-865	0.24	0.19
100/06-08-041-25W4/00	1613-1627	0.12	0.17
100/06-09-012-18W4/00	1062-1079	0.18	0.18
102/09-16-033-25W4/00	1680.06	0.03	0.16
100/06-07-051-07W5/00	1885-1896	0.13	0.14
100/12-13-049-01W5/00	1417-1469	0.13	0.12
100/02-08-039-04W5/00	2244-2254	0.12	0.12
100/11-23-031-23W4/00	1526-1548	0.11	0.10
100/04-05-039-04W5/00	2255-2265	0.11	0.12
		Mean:	0.14

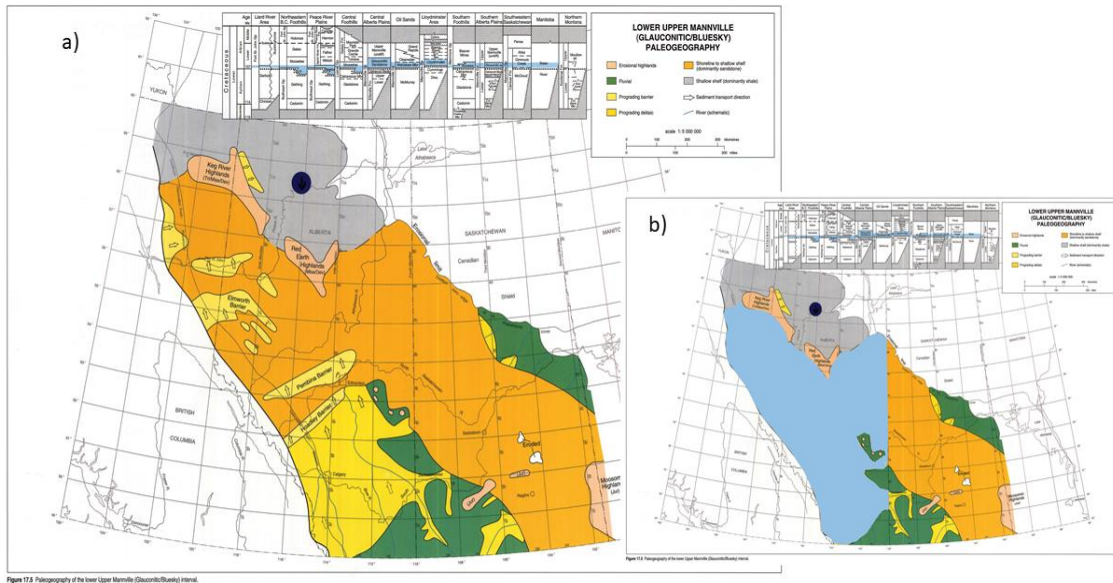


Figure AC-1 a) Map of the Lower Upper Mannville (Glaucconitic/Bluesky) Paleogeography (Hayes et al., 1994a) retrieved from https://static.ags.aer.ca/files/image-content/fg17_05.jpg. b) The area in blue represents the area of glauconitic sandstones calculated using ImageJ (Rasband, 2018) in this study. Although records of glauconite are present in the shale (light grey) and the fluvial sediments (green), these areas are not accounted towards the total area of glauconite, because these sediments tend to be less ideal CO₂ injection material.

Using ImageJ analysis (Rasband, 2018), the scale of the map is 2.36 pixel/km. By applying scaled measurements on thresholded images, the area of glauconitic sandstones is ~492,527 km². Due to the low resolution of the original map, the borders on geological units are unclear in thresholded images, which caused roughness along the edges. By manually tracing the map and removing 1-2 km² roughness around the borders, we estimated 426,332 - 403,443 km² of glauconitic sandstones. The smallest measurement was applied to our calculations for the most conservative estimate.

Appendix D Copyright Letter of Permission

Letter of Permission

Benjamin Tutolo
To: Qin Zhang



Mon 5/9/2022 4:58 PM

Permission granted.

From: Qin Zhang
Sent: May 9, 2022 4:58 PM
To: Benjamin Tutolo
Subject: Letter of Permission

Hi Ben,

I am writing to request your permission as a coauthor, in order to use the following publication as part of my PhD thesis titled "From Greensands to Green Technology: Examination of Carbon Dioxide Storage Potential in Glauconitic Sandstones":

Zhang, Qin, and Benjamin M. Tutolo. "Evaluation of the potential of glauconite in the Western Canadian Sedimentary Basin for large-scale carbon dioxide mineralization." *International Journal of Greenhouse Gas Control* 117 (2022): 103663.

Zhang, Qin, and Benjamin M. Tutolo. "Geochemical evaluation of glauconite carbonation during sedimentary diagenesis." *Geochimica et Cosmochimica Acta* 306 (2021): 226-244.